AD_____

Award Number: **W81XWH-08-1-0705**


TITLE:     Redox Abnormalities as a Vulnerability Phenotype for Autism and Related Alterations in CNS
            Development


PRINCIPAL INVESTIGATOR:     **Maria Hepel**


CONTRACTING ORGANIZATION: **Research Foundation of SUNY**
                            Potsdam, NY  13676


REPORT DATE: **October 2010**


TYPE OF REPORT:     **Annual**


PREPARED FOR:  U.S. Army Medical Research and Materiel Command
                Fort Detrick, Maryland  21702-5012


DISTRIBUTION STATEMENT: (Check one)

     X     Approved for public release; distribution unlimited

# REPORT DOCUMENTATION PAGE

*Form Approved*
*OMB No. 0704-0188*

Public reporting burden for this collection of information is estimated to average 1 hour per response, including the time for reviewing instructions, searching existing data sources, gathering and maintaining the data needed, and completing and reviewing this collection of information. Send comments regarding this burden estimate or any other aspect of this collection of information, including suggestions for reducing this burden to Department of Defense, Washington Headquarters Services, Directorate for Information Operations and Reports (0704-0188), 1215 Jefferson Davis Highway, Suite 1204, Arlington, VA 22202-4302. Respondents should be aware that notwithstanding any other provision of law, no person shall be subject to any penalty for failing to comply with a collection of information if it does not display a currently valid OMB control number. **PLEASE DO NOT RETURN YOUR FORM TO THE ABOVE ADDRESS.**

| 1. REPORT DATE *(DD-MM-YYYY)* <br> 1/10/2010 | 2. REPORT TYPE <br> Annual | 3. DATES COVERED *(From - To)* <br> 15 SEP 2009 - 14 SEP 2010 |
|---|---|---|
| **4. TITLE AND SUBTITLE** <br> Redox Abnormalities as a Vulnerability Phenotype for Autism and Related Alterations in CNS Development | | **5a. CONTRACT NUMBER** |
| | | **5b. GRANT NUMBER** <br> W81XWH-08-1-0705 |
| | | **5c. PROGRAM ELEMENT NUMBER** |
| **6. AUTHOR(S)** <br> Maria Hepel, PhD <br><br> Email: hepelmr@potsdam.edu | | **5d. PROJECT NUMBER** |
| | | **5e. TASK NUMBER** |
| | | **5f. WORK UNIT NUMBER** |
| **7. PERFORMING ORGANIZATION NAME(S) AND ADDRESS(ES)** <br><br> Research Foundation of SUNY <br> Potsdam, NY 13676 | | **8. PERFORMING ORGANIZATION REPORT NUMBER** |
| **9. SPONSORING / MONITORING AGENCY NAME(S) AND ADDRESS(ES)** <br><br> US ARMY MEDICAL RESEARCH and Material Command <br> 820 Chandler St. <br> **FORT DETRICK MD 21702-5014** | | **10. SPONSOR/MONITOR'S ACRONYM(S)** |
| | | **11. SPONSOR/MONITOR'S REPORT NUMBER(S)** |

**12. DISTRIBUTION / AVAILABILITY STATEMENT**
Approved for public release; distribution unlimited

**13. SUPPLEMENTARY NOTES**

**14. ABSTRACT**

The interactions of biomarkers of oxidative stress with various dye molecules and antibodies have been investigated to explore possible venues for designing sensors for these biomarkers. This was followed by the development of several sensor types and testing their performance. Printed circuits were developed for single microsensors and for sensor arrays. The oxidative stress biomarkers, including glutathione (GSH), glutathione disulphide, cysteine, and homocysteine, were also studied in processes of ligand exchange in core-shell gold nanoparticles for application in novel assays for GSH, cysteine and homocysteine, as well as for the enhancement of sensor sensitivity. The monoclonal anti-GSH antibody piezoimmunosensors and molecular beacons for the detection of GSH have been designed and tested. The neural network analysis of sensor signals from the same type of sensors has been developed and will be applied to the analysis sensor arrays during the third year of the Project.

**15. SUBJECT TERMS**
Sensors for oxidative stress biomarkers, glutathione, cysteine, homocysteine, autism

| 16. SECURITY CLASSIFICATION OF: | | | 17. LIMITATION OF ABSTRACT | 18. NUMBER OF PAGES | 19a. NAME OF RESPONSIBLE PERSON <br> USAMRMC |
|---|---|---|---|---|---|
| **a. REPORT** <br> U | **b. ABSTRACT** <br> U | **c. THIS PAGE** <br> U | UU | 76 | **19b. TELEPHONE NUMBER** *(include area code)* |

**Standard Form 298 (Rev. 8-98)**
**Prescribed by ANSI Std. Z39.18**

**Table of Contents**

## Introduction

During the second year of this Project, we have investigated interactions of biomarkers of oxidative stress to be utilized in sensors for testing autism biomarkers and diagnose environmental conditions requiring preventive or medical intervention to control the development of the disease. The interactions of oxidative stress biomarkers with various dye molecules, including fluorone black and coumarin derivatives, monochlorobimane, molecular beacons, and antibodies were investigated in order to explore possible venues for designing enhanced sensors for these biomarkers. This was followed by the development of several sensor types and testing their performance. Printed circuits were developed for single microsensor chips and for sensor arrays. The oxidative stress biomarkers, including glutathione (GSH), cysteine (Cys), and homocysteine (Hcys), were also studied in processes of ligand exchange in core-shell gold nanoparticles [1-3] for application in novel assays for GSH, cysteine and homocysteine, as well as for the enhancement of sensor sensitivity due to the improved electrocatalytic activity and increased real surface area. Studies of the ligand exchanges in GSH-Hcys-capped gold nanoparticles [3] have shown interesting kinetic effects and pH dependence enabling for their analytical determinations [2]. On the other hand, by adsorbing fluorosurfactant on a gold surface, homocysteine and cysteine could be analyzed [1]. By considering detailed potential distribution in sensory films, we have made an attempt to design a novel anti-GSH monoclonal antibody based sensor with positive potential barrier. This type of sensor can be tested in piezoimmunosensing, as well as the redox-probe voltammetric framework. The sensor development studies were paralleled with efforts to miniaturize sensor chips and gaining experience with operation of sensor arrays.

## Body

The investigations carried out during the second year of the Project involved continuation of studies on several sensing platforms commenced during the first year, as well as new studies on electrocatalytic materials for application in sensors for oxidative stress biomarkers. These investigations were followed by developmental work on designing microsensor chips, testing the microsensors, and miniaturization studies using microsensor arrays.

Since the interactions of oxidative stress biomarkers with other molecules, electrocatalysts surfaces and nanoparticles are the key factor in analytical platform development and signal transduction, our studies involved the investigation of interactions of glutathione, cysteine and homocysteine with dye molecules, conductive polymers, different electrode surfaces including various forms of carbon, gold, and metal alloys, as well as with ligands in core-shell nanoparticle microenvironment framework. Among the dyes that interact with GSH, we have studied: (i) derivatives of fluorone black (FB) due to the electrochemical activity of FB and possible electron mediation of the GSH oxidation process, (ii) coumarin (CM) derivatives due to the possible effect of GSH and GSSG on the reduction waves of various coumarins, and (iii) monochlorobimane (MCB) due to the kinetic effects associated with slow binding of GSH to MCB and high specificity of this reaction. While the interactions of GSH, Cys, and Hcys with these dyes may be best studied using optical techniques such as the absorbance, fluorescence, and resonance elastic light scattering spectroscopies, the sensor designs may involve electrochemical, impedance, piezometric, or optical techniques. Hence, comprehensive studies are necessary to evaluate the optimum approach. The interaction of oxidative stress biomarkers with dyes are generally characterized with relatively low binding constant. A dramatical increase of the binding characteristics comes with the application of antibodies and other biorecognition systems. We have investigated biosensors based on anti-GSH monoclonal antibody and on molecular beacons. Both these platforms show high sensitivity that comes in cost of reduced durability and expensive reagents. The molecular beacon that we have developed responds to GSH and Cys down to $10^{-8}$ M concentration and could be utilized for the analysis of plasma samples to diagnose GSH deficiency.

In the report, we show also the microsensor chip circuit and sensor array circuit that will be used for further analysis. Initial experimental work with these new sensors has been described and it will be expended during the third year of the Project.

3

*Aim 1*: *Design EQCN sensors responsive to GSH, GSH+GSSG, and thioaminoacids to determine and monitor the redox potential in biological samples as a potential biomarker for autism.*

a) design and testing of polyclonal antibody sensors responsive to GSH + GSSG using electrochemical Quartz crystal nanobalance (EQCN) and quartz crystal immittance (QCI) techniques (Months 1-12); N/A

b) design and testing of monoclonal anti-GSH antibody sensors using QCI and AFM techniques (Months 13-24);

**The GSH immunosensors based on a rabbit monoclonal anti-GSH antibody were designed utilizing experiences gained in year 1 of the Project while constructing mouse polyclonal anti-GSH antibody. Two types of immunosensors were prepared: (i) sensors with positively charge basal SAM film with aminohexane thiol (AHT) and (ii) sensors with negatively charged basal film in the form of deprotonated GSH-SAM. The sensor surface was imaged using the atomic force microscopy (AFM) to evaluate uniformity of surface coating. The sensors were examined by quartz crystal immittance (QCI) spectroscopy and the resonance frequency changes were related to the apparent mass changes that were measured using the electrochemical quartz crystal nanobalance (EQCN) which is an integral part of the QCI instrumentation (EQCN-930). The details of the sensor design and the applied procedures are described below.**
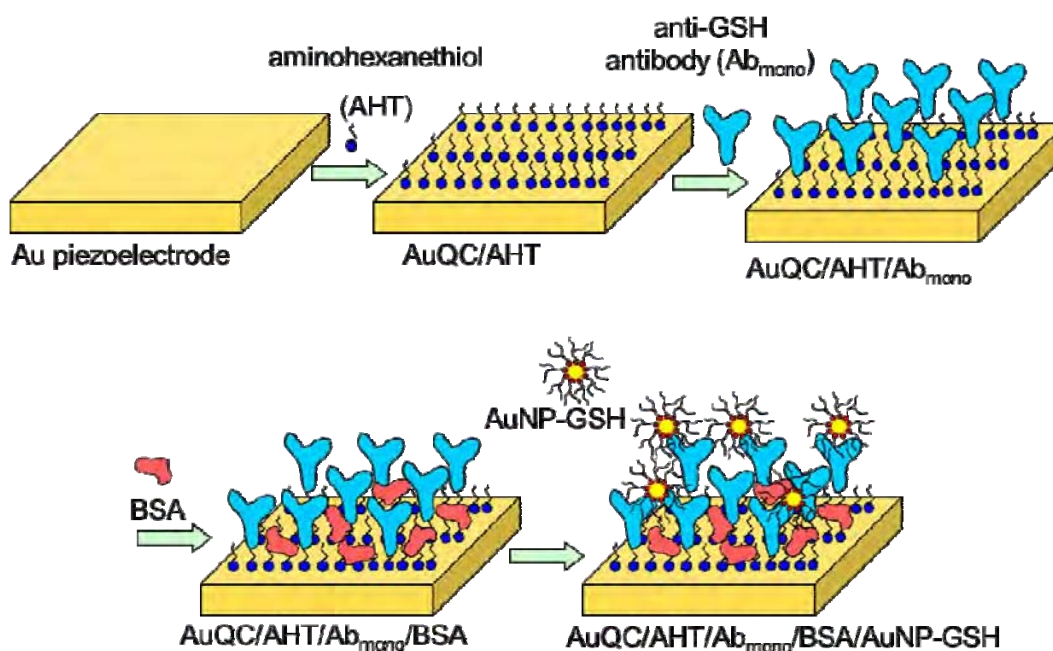
**Preparation of immunosensors:**

*Type I sensor: QC/Au/AHT/Ab$_{mono}$/BSA.* **The aminohexanethiol (AHT) was immobilized on a fresh quartz crystal Au-electrode by immersing the electrode in 3.2 mM AHT ethanolic solution for 75 min. After washing with PBS buffer, the antibody molecules were attached via amide bonds to a self-assembled monolayer of AHT by incubating the electrode in 6.7 μM anti-GSH monoclonal antibody for 75 min. The carboxylic groups of anti-GSH antibody were activated by 0.033 M EDC. A BSA solution (0.001%) was then applied for 60 min to adsorb BSA and block nonspecific binding sites. The biosensor was rinsed with 50 mM PBS buffer and used for testing the antibody-antigen interactions using free GSH or GSH-capped AuNP as the analyte. For the control experiments, the electrodes were prepared without antibody. Voltammetric measurements were performed in 1 mM $K_3Fe(CN)_6$ and 1 mM $Ru[(NH)_3]_6$ in phosphate buffer saline solution (PBS) consisting of 0.15 M NaCl, 2 mM KCl, and 50 mM phosphate buffer pH = 7.4.**

*Type II sensor: QC/Au/GSH/Ab$_{poli}$/GSH-AuNP.* **A quartz crystal piezoelectrode was immersed in a 5 mM glutathione (GSH) solution for 20 min. Then, a solution of 58 μM anti-GSH antibody (1:2000 dilution of original solution) with carboxylic groups activated by 0.033 M EDC was added to bind covalently the IgG to AHT-SAM and form the recognition layer. The biosensor was tested for the detection of GSH-capped AuNP. For the control experiments, electrodes without antibody layer were used. Voltammetric measurements were performed in 4 mM $Fe(CN)_6^{-3}$ in 1M $KNO_3$, pH = 6.74. This sensor, designed and tested for the sake of comparison with the positive barrier sensor, responds also to GSH-capped AuNP but shows lower sensitivity than the type I sensor. Therefore, we do not include any further details on the negative barrier sensor in this report. They will be included in the paper which is under preparation for publication.**

## Results and Discussion
### *Design of positive potential-barrier immunosensor for GSH*

The immunosensor designed in this investigation is depicted in Scheme 1. The anti-GSH antibody molecules were immobilized on positive potential-barrier SAM of aminohexanethiol (AHT). For the attachment of proteins, the SAMs with functional groups such as $NH_2$, COOH, OH are suitable [4-6]. The accessibility of binding sites for the analyte epitope at the top branches of the Y shaped antibody molecules is the key element in the sensor response. In this work, the anti-GSH antibody molecules were immobilized on an AHT SAM adsorbed on gold piezoelectrode via amide bonds between carboxylic groups of the Fc stem of an Ab and amine groups of the thiol. The carboxylic groups of Ab were activated with EDC reagent. In this work, the IgG molecules were covalently attached through the amide bond formation to –$NH_2$ groups of the basal SAM. Because of the absence of carboxyl groups in the Fab recognition arms of IgG, the amide bond formation leads to the favorite orientational bonding of IgG molecules in the sensory film. To control nonspecific binding, the electrodes were incubated with 0.001% BSA solution in 0.1M PBS pH 7.4. The main goal of this work was to evaluate electrostatic interactions in the sensory film based on the AHT basal SAM. The analyte solutions in the form of a free GSH or GSH-capped gold nanoparticle (AuNP@GSH) solution were added to investigate the antigen-antibody interactions.



Scheme 1. The design of an electrochemical and nanogravimetric immunosensor with positive potential barrier for the detection of glutathione-capped AuNP.

### *Nanogravimetric monitoring of immunosensor construction*
Each step of the modification of a gold piezoelectrode was monitored by the electrochemical quartz crystal nanogravimetry to confirm binding of molecules and the structure build up on a gold electrode.
The adsorption of AHT from ethanolic solution results in a multilayer film formed on a gold surface. After washing the excess of AHT in ethanol and water, the amount of adsorbed AHT was estimated from the net mass change: $\Delta m$ = 32.9 (25.4)

ng/QC corresponding to mass density $m_{AHT}$ = 128.9 (99.7) ng/cm$^2$ and surface coverage: $\gamma_{AHT}$ = 0.75 nmol/cm$^2$ ($\Gamma_{AHT}$ = 4.52x10$^{14}$ molec/cm$^2$; adsorption of AHT.HCl is assumed, as necessary for the charge balance) and independently, from the charge $Q_{des}$ required for the reductive desorption of AHT taking place during the potential scan from -0.4 V to -1.2 V in alkaline solution: $q_{des}$ = 18.0 μC/QC ($Q_{des}$ = 70.4 μC/cm$^2$) corresponding to surface excess: $\gamma_{AHT}$ = 0.73 nmol/cm$^2$ ($\Gamma_{AHT}$ = 4.40x10$^{14}$ molec/cm$^2$), assuming one-electron transfer cathodic process: Au-S(CH$_2$)$_6$NH$_3^+$ + H$^+$ + e$^-$ = Au + HS(CH$_2$)$_6$NH$_3^+$. These values compare favorably with theoretical charge and coverage for linear alkane thiols: $Q_{des}$ = 74.1 μC/cm$^2$, $\gamma_{AHT}$ = 0.768 nmol/cm$^2$, $\Gamma_{AHT}$ = 4.62x10$^{14}$ molec/cm$^2$ [7, 8].

In a typical nanogravimetric mass transient, recorded after the injection of monoclonal anti-GSH antibody solution (10 μL of 1 mg/mL IgG solution to 1 mL of PBS + 0.5 mL of 0.1 M EDC; final concentration of IgG: 6.67 μg/mL), the total resonant frequency shift Δf = 370 Hz (corresponding to apparent mass increase Δ$m$ = 321 ng/QC) is observed. To evaluate the maximum surface coverage by IgG molecules, the following X-ray derived dimensions of the four-peptide chain Y-shaped IgG molecule have been taken into account: the two identical antigen binding Fab arms with dimensions 6.5 nm by 3.5 nm and the inactive Fc shrank with dimensions 5 nm by 3.5 nm [9]. Hence, the theoretical surface coverage by IgG is obtained: $\gamma_{IgG,theo}$ = 4.31 pmol/cm$^2$ ($\Gamma_{IgG,theor}$ = 2.60x10$^{12}$ molec/cm$^2$) and the mass of a monolayer of IgG is $m_{IgG,theor}$ = 629.7 ng/cm$^2$, corresponding to the amount od IgG adsorbed on a QC/Au surface: Δ$m$ = 160.6 ng/QC, based on the molecular mass $M_{Ab}$ = 146 kDa (subgroup IgG2). Taking into account the apparent mass amplification known for other antibody films which is due to the incorporation of solvent in IgG films, this result likely indicates on a full coverage of the electrode surface by IgG molecules, $\theta \approx 1$. This is supported by control experiments with higher concentration of IgG in which no further mass increases were observed. From our experiments, it follows that the mass-percent of water in IgG film is 49.9% (i.e. 160.4 ng of water and 160.6 ng of IgG) and the volume-percent of water is even higher, as it approaches 71% (based on the mass of pure water film, 11.5 nm thick, equal 225.4 ng/QC).

To control nonspecific binding, the electrodes were incubated in a BSA solution. The experimental apparent mass change observed during incubation was Δ$m$ = 52.9 ng, which corresponds to a mass density $m_{BSA}$ = 207.4 ng/cm$^2$ and surface coverage: $\gamma_{BSA}$ = 3.01 pmol/cm$^2$ ($\Gamma_{BSA}$ = 1.81x10$^{12}$ molec/cm$^2$). This surface coverage is lower than that calculated for theoretical dense packing coverage for vertical orientation of BSA [10]: $\gamma_{BSA,theo}$ = 5.49 pmol/cm$^2$ ($\Gamma_{BSA,theor}$ = 3.31x10$^{12}$ molec/cm$^2$, $m_{BSA,theor}$ = 378.8 ng/cm$^2$) and that for horizontal orientation: $\gamma_{BSA,theo}$ = 3.35 pmol/cm$^2$ ($\Gamma_{BSA,theor}$ = 2.02x10$^{12}$ molec/cm$^2$, $m_{BSA,theor}$ = 231.5 ng/cm$^2$), based on molecular dimensions: 5.5 x 5.5 x 9 nm$^3$ [11]). It is also lower than experimentally measured saturation coverage of BSA on citrate-coated Au surface: $\gamma_{BSA,theo}$ = 6.14 pmol/cm$^2$ ($\Gamma_{BSA,theor}$ = 3.31x10$^{12}$ molec/cm$^2$, $m_{BSA,theor}$ = 378.8 ng/cm$^2$) and a bare Au electrode: $\gamma_{BSA,theo}$ = 15.3 pmol/cm$^2$ ($\Gamma_{BSA,theor}$ = 9.20x10$^{12}$ molec/cm$^2$, $m_{BSA,theor}$ = 1054 ng/cm$^2$), measured recently by Brewer et al. [12]. The latter value was likely due to the multilayer film formation and change in viscoelastic properties which becomes non-negligible for multilayer protein films. In contrast, in our experiments, the BSA coverage is only: $\theta$ = 0.55 (in equivalent BSA monolayers with vertical orientation). The coverage lower than the equivalent monolayer is expected since BSA only fills the gaps between IgG molecules. The BSA molecules cannot replace IgG molecules since they

are covalently bound to the anchored AHT SAM. The coverages cited above are considered for the sake of comparison only since the exact evaluation would require additional information concerning conformation changes of IgG resulting in film thickness increase, changes in water content in the film, as well as changes in the film viscoelastic properties, if any. However, it is clear that the measurement sensitivity is sufficient for monitoring the amount of components immobilized on the sensor surface and establishing a protocol for rejecting sensors that fall outside of the preset apparent mass ranges. For the purpose of this work, the apparent mass variation within ±10% were assumed and found not to influence considerably the general characteristics of films and their behavior.
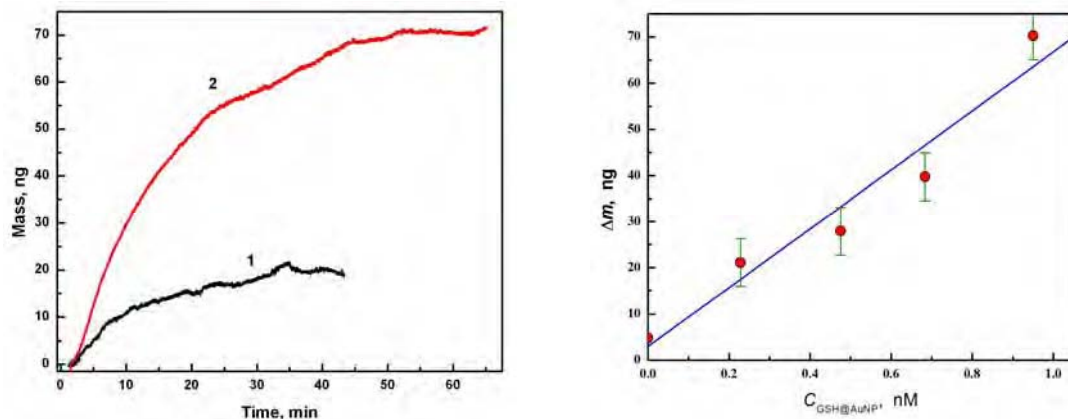


**Figure 1.** *Left panel*: **Changes of apparent mass vs. time during binding of: (1) glutathione and (2) glutathione-capped AuNP, on a AuQC/AHT/Ab$_{mono}$/BSA modified gold piezoelectrode.** *Right panel*: **Dependence of apparent mass change vs. AuNP@GSH concentration for a QC/Au/AET/BSA,Ab$_{mono}$ sensor in 50 mM PBS, with surface regeneration in 0.2 M glycine solution, pH = 3, after each test.**

The IgG used in this study was a monoclonal mouse antibody (Ab$_{mono}$) that is specific to glutathione. Figure 3 presents the apparent mass response of the AuQC/AHT/Ab$_{mono}$/BSA modified piezosensor immersed in: (1) GSH solution and (2) AuNP@GSH solution. As illustrated in Figure 1 (left panel), the Ab$_{mono}$ shows higher affinity towards glutathione-capped gold nanoparticles than glutathione alone. The lower immunoreactivity in the latter case clearly indicates that GSH itself does not have the sufficient size and structural complexity to induce the formation of Ab$_{mono}$ with very high affinity toward small GSH antigen (Amara et al. [13]).

For the immunosensor regeneration, we have found that washing the sensors with an aqueous 0.2 M solution of glycine, pH 3.04, and rinsing with PBS buffer provides satisfactory results. Similar procedure was recently adopted by Wasowicz et al. [14]. The apparent mass change vs. AuNP@GSH concentration plot for a QC/Au/AHT/Ab$_{mono}$ piezoimmunosensor, with surface regenerated with glycine solution after each test, is presented in Figure 3 (right panel). The calibration plot is fitted by the least-square fitting routine to give a straight line:

$$\Delta m = a + b \, C_{AuNP@GSH},$$

with intercept $a = 2.97$ ng and slope $b = 63.8$ ng/nM (the nanoparticle concentration is given in nM).

*A "molecular beacon" based fluorescent assay for selective detection of glutathione and cysteine*

Molecular beacons are composed of a single-stranded oligonucleotide with self-complementary 5' and 3' ends that can self-hybridize (Scheme 2). In the absence of a target, it forms a stem-loop structure that brings a fluorophore/quencher pair, attached to the ends of the DNA strand, into close proximity, reducing fluorescence emission. Once the single stranded loop portion of the molecular beacon hybridizes to the target, the stem melts and the resulting spatial separation of the fluorophore from the quencher leads to an enhancement in fluorescence. We have investigated a fluorescence turn-on "molecular beacon" probe for the detection of glutathione (GSH) and cysteine (Cys). The method was based on a competitive ligation of $Hg^{2+}$ ions by GSH/Cys and thymine-thymine (T-T) mismatches in a DNA strand of the self-hybridizing. (Scheme 2).
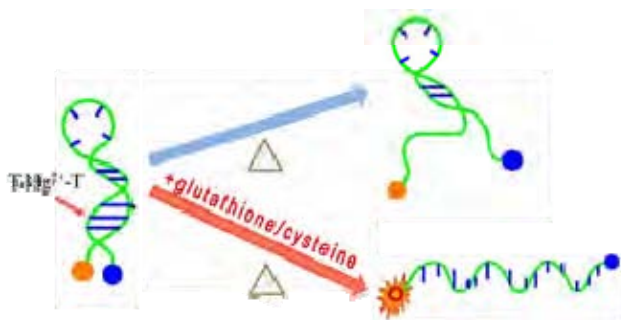


Scheme 2. The mechanism of turning "on" the molecular beacon by addition of GSH/Cys caused by extraction of $Hg^{2+}$ ions from the MB stem and separation of the fluorophore 6-FAM (orange) from the quencher DABCYL (blue).

The molecular beacon that we have developed responds to GSH and Cys with nanomolar sensitivity (Figure 2). $5 \times 10^{-9}$ M GSH/Cys can induce measurable fluorescence signal, indicating that the present method can successfully detect the GSH/Cys with high sensitivity. At the same condtions, very little change of the fluorescence intensity was observed upon addition of other amino acids (Figure 602d).
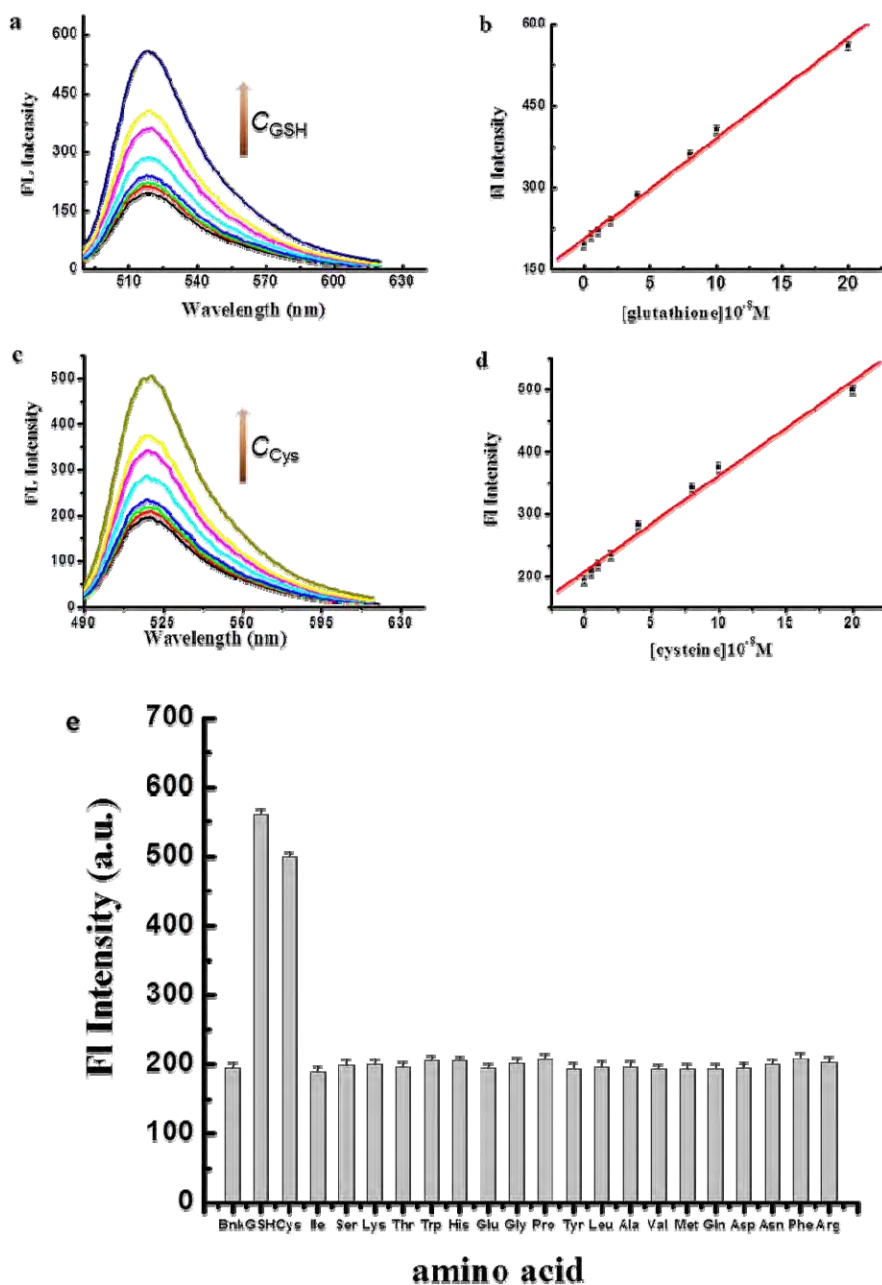
**Figure 2.** Fluorescence emission spectra for different concentrations of GSH (a) and Cys (c); (b,c) dependence of $I_{FL}$ vs (b) $C_{GSH}$ or (c) $C_{Cys}$ , (e) influence of different amino acids and GSH on fluorescence emission spectrum of MB/Hg$^{2+}$, [DNA] = [Hg$^{2+}$] = $1\times10^{-7}$ M, measurements after 15 min at 52°C; [MB] = [Hg$^{2+}$] = $1\times10^{-7}$ M; [amino acid] = $2\times10^{-7}$ M.

c) study of high density immobilized fluorone analogue GSH EQCN sensors (Months 1-6); N/A

d) investigations of electrochemical reactivity of coumarins and design of coumarin analogue EQCN sensors responding to GSH and thioaminoacids (Months 7-18);

**We have continued the investigations of fluorescence emission and electrochemical reactivity of coumarin dyes. The focus of this study was on the interactions of coumarins with gold nanoparticles (AuNP) and in particular, on the energy transfer between coumarin dye molecules acting as the donor and AuNP acting as the acceptor. We have considered several derivatives of the main coumarine dye (Scheme 3). The behavior of coumarin dyes and their interactions with biomarkers of oxidative stress and gold nanoparticle carriers have been studied (Figures 3-5). The characteristics obtained are utilized in the development of sensor arrays for biomarkers of oxidative stress in year 3 of the Project. The interactions of AuNP with coumarins are important for the development of assays for GSH and homocysteine based on the accumulation of these biomolecules on the nanoparticle surface which we have studied extensively during the first two years of the Project.**
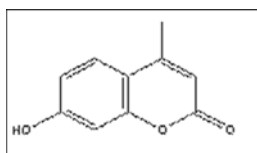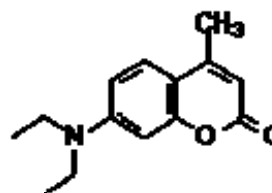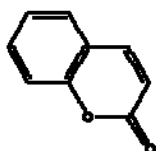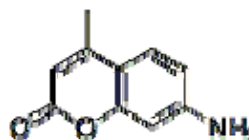
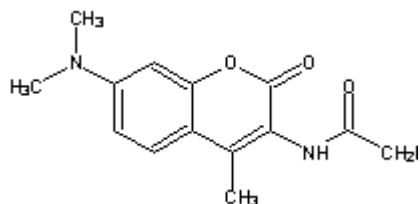Basic coumarin dye
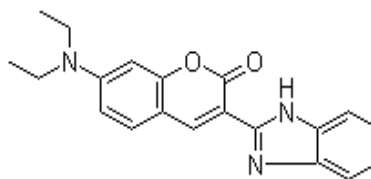
Coumarin 7
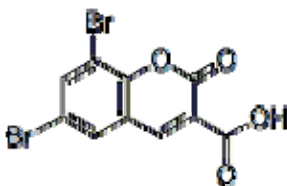
6,8-Dibromocoumarin-3-arboxylic

Coumarin 1

Coumarin 4

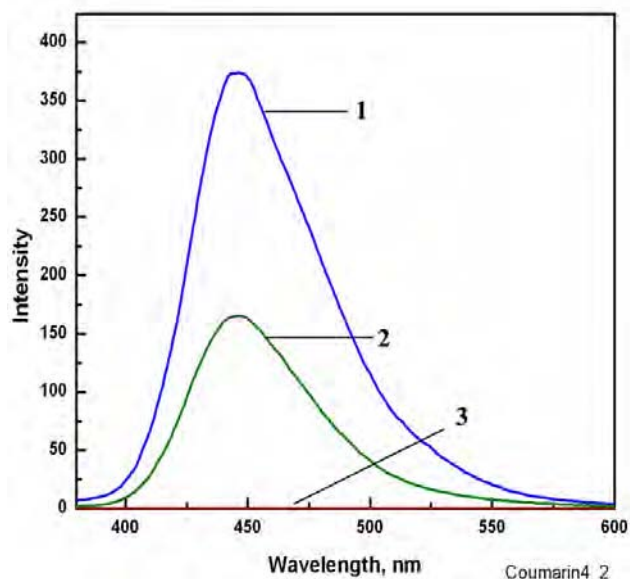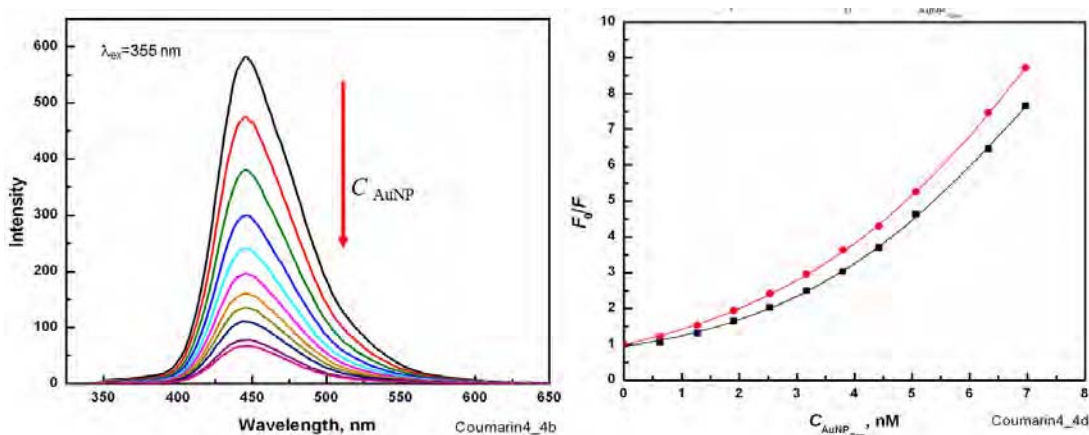Coumarin 120

N-(7-Dimethylamino-4-methylcoumarin
-3-yl) iodoacetamide

**Scheme 3. Coumarin dyes.**

**Figure 3. Effect of AuNP$_{5nm}$ on fluorescence spectrum of coumarin 4: (1) 166.7 μM coumarin 4, (2) 166.7 μM coumarin 4 + 3.8 nM AuNP$_{5nm}$. and (3) emission spectrum of 3.8 nM AuNP$_{5nm}$ . Excitation wavelength: λ$_{ex}$ = 363 nm.**



**Figure 4. Fluorescence spectra for AuNP$_{5nm}$ in the presence of 50 μM coumarin 4; AuNP concentration [nM]: (1) 0, (2) 0.63, (3) 1.27, (4) 1.9, (5) 2.53, (6) 3.17, (7) 3.8, (8) 4.43, (9) 5.07, (10) 6.33, (11) 6.97. Excitation wavelength: (left panel) λ$_{ex}$ = 363 nm; (right panel) dependence of $F_0$/F vs. $C_{AuNP,5nm}$ for: (1) excitation wavelength λ$_{ex}$ = 363 nm and (2) λ$_{ex}$ = 355 nm.**

11
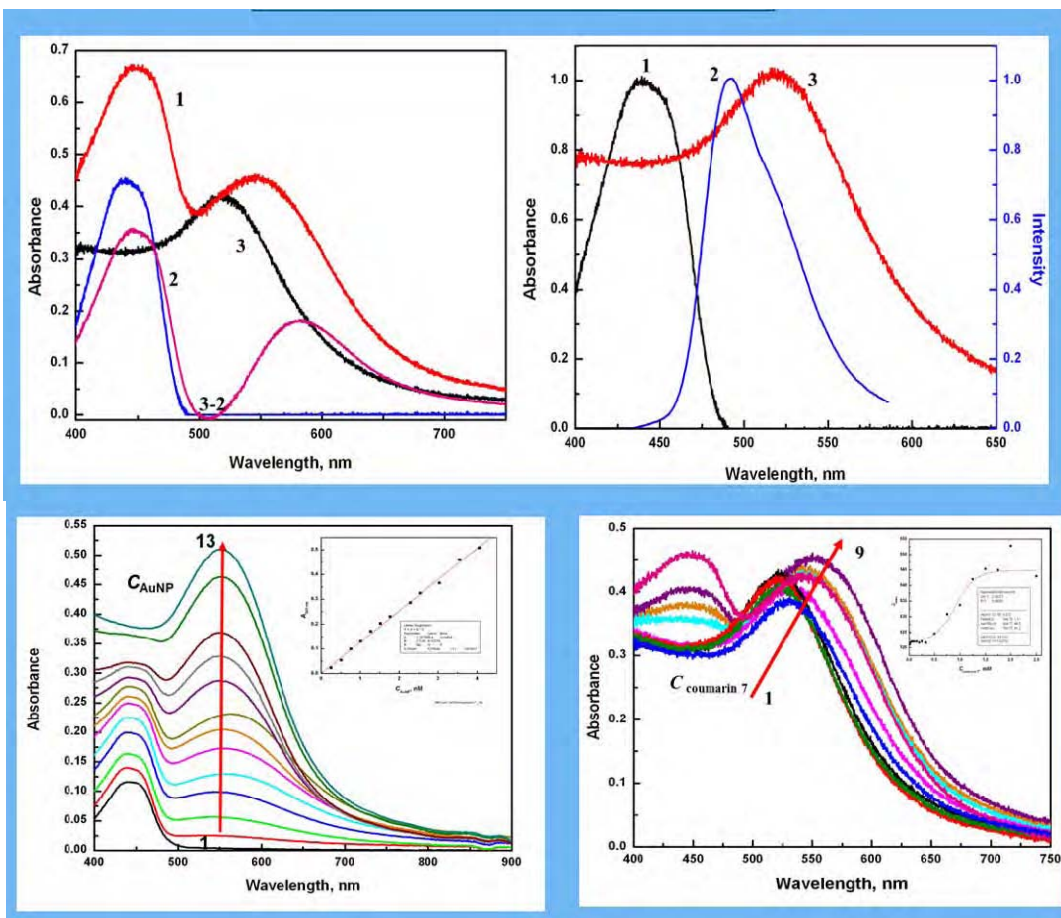
**Figure 5. Fluorescence emission behavior of Coumarine 7 in the presence of AuNP.**

*Upper-left panel*: **Effect of AuNP$_{5nm}$ on absorbance spectrum of coumarin 7: (1) 5 μM coumarin 7, (2) 9 nM AuNP$_{5nm}$, (3) 9 nM AuNP$_{5nm}$+ 5 μM coumarin 7, (3-2) difference spectrum of (3) minus (2).**

*Upper-right panel:* **Normalized absorbance (1) and fluorescence (2) spectra of coumarin 7, $C_{coumarin7}$ = 5 μM and 500 nM respectively for absorbance and fluorescence measurements. (3) Absorbance spectrum of 9 nM AuNP$_{5nm}$**

*Lower-left panel*: **(a) Absorbance spectra for different concentrations of AuNP$_{5nm}$ in the presence of 2.5 μM coumarin 7; AuNP$_{5nm}$ concentration, $C_{AuNP}$ [nM]: (1) 0, (2) 0.253, (3) 0.507, (4) 0.76, (5) 1.013, (6) 1.27, (7) 1.52, (8) 1.77, (9) 2.28, (10) 2.53, (11) 3.04, (12) 3.55, (13) 4.05, Inset: Dependence of $A_{535\,nm}$ vs. $C_{AuNP}$.**

*Lower-right panel*: **(a) Absorbance spectra of Coumarin 7 in the presence of 3.8 nM spherical gold nanoparticles AuNP$_{5nm}$, $C_{coumarin\,7}$ [μM]: (1) 0, (2) 0.1, (3) 0.5, (4) 0.75, (5) 1.0, (6) 1.5, (7) 1.75, (8) 2, (9) 2.5, Inset: dependence of $\lambda_{max}$ vs. $C_{coumarin\,7}$.**

The results are in preparation for publication. The investigations of coumarin reactivity and energy transfer will continue during the year 3 of the Project in the development of sensor arrays for biomarkers of oxidative stress.

e) testing of 20 samples, 1 mL extracts, from Projects 1 and 2 using the above sensors to check for matrix effects (Months 18-24);

**The plasma samples were obtained from the University of Arkansas and Arkansas Children Hospital research group of Professor J. James. The samples were tested for the matrix effects in analytical determination of GSH levels. The tests were performed in two groups; (i) in the first group, proteins from plasma samples were removed by precipitation with 5-sulfosalicylic acid (SSA), which is recommended for the removal of proteins from sample solutions and for the prevention of GSH oxidation, followed by centrifugation at 8,000 rpm (10 min), and collecting supernatant for further analyses; (ii) in the second group, plasma samples were used as received to obtain information on the influence of proteins, mostly human serum albumin (HSA), on the GSH analyses. The analyses were performed using fluorescence spectroscopy, immunosensors and dye-modified glassy carbon electrodes. The matrix effects have been evaluated using standard addition method and calibration curves in pure buffer solutions. In Figures 6 and 7, examples of the standard addition method applied to a plasma sample and comparison of calibrations with pure buffer and plasma are presented.**
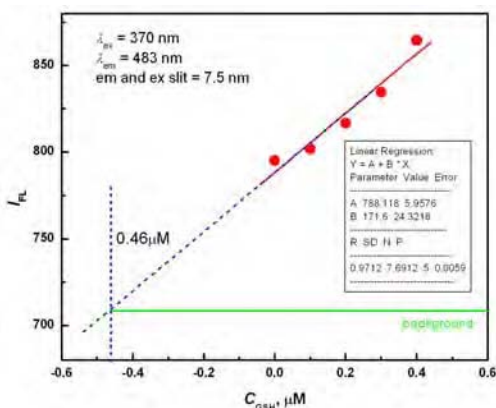


**Figure 6. Determination of GSH in a plasma sample by standard addition method; MCB concentration: 33 µM, glutathione S-transferase (GST) concentration: 10 µg/mL, $\lambda_{ex}$ = 370 nm, $\lambda_{em}$ = 483 nm, plasma dilution: 10x, 20 mM PBS buffer, pH = 7.4.**
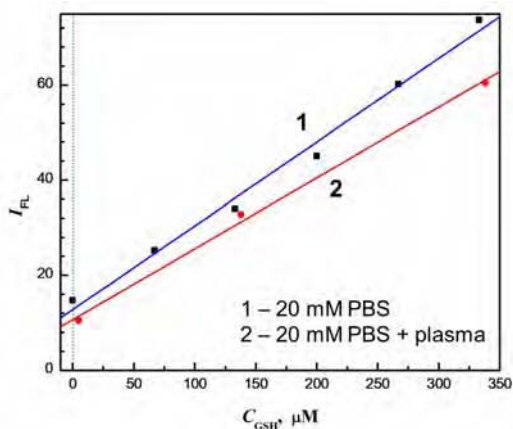


**Figure 7. Effect of plasma matrix on calibration curve for GSH: (1) calibration in 20 mM PBS buffer, (2) calibration curve in 20 mM PBS in the presence of plasma, obtained from a standard addition experiment after shifting the concentration scale to account for the GSH concentration in plasma sample; $C_{MCB}$ = 330 µM, GSH S-transferase concentration: 1 mg/mL, $\lambda_{ex}$ = 370 nm, $\lambda_{em}$ = 483 nm.**

13

The evaluation of matrix effects introduced by the presence of blood plasma components was performed by utilizing the data from standard-addition experiments. An example of the comparison with the calibration curve obtained in 20 mM PBS buffer was made by shifting the concentration scale in the standard addition experiment graph to account for the GSH concentration in plasma sample. This comparison, presented in Figure 7, indicates that in this example, the ordinate intercept is lowered by the plasma from 12.7 to 10.6 a.u., or 15.5%. The slope of the calibration curve is decreased from 0.1762 to 0.1492, or 15.3%, in the presence of plasma.

Due to specificity of each analytical determination methods, the matrix effects have to be evaluated separately for each sensor type included in the integrated array analysis system. This work is routinely done while developing each new sensor and the applied determination technique.

*Aim 2*: *Design a biosensor chip composed of an artificial neural network of nanosensors with immobilized different host molecules providing redox potential information that can be utilized in determining potential vulnerability to autism.*

a) construction of fluorone derivative microsensors and testing their performance (Months 12-18);

**Several sensors incorporating xanthene fused triple-ring moiety have constructed and tested. The rigid xanthene group is responsible for fluorescent properties of many dyes, including fluorone, fluorescein, pyronine, rhodamine B [15], and their derivatives. The monochlorobimane (MCB) dye is also included here because of the specificity of the interaction of MCB with GSH.**

*Experimental*

**Apparatus. The fluorescence spectra were recorded using LS55 Spectrometer (Perkin Elmer, Waltham, MA, U.S.A.) equipped with 20 kW Xenon light source operating in 8 $\mu$s pulsing mode. Separate monochromators for the incident beam and the detector beam enabled to use monochromatic radiation with wavelengths from 350 nm to 700 nm. The dual detector system consisted of a photomultiplier tube (PMT) and an avalanche photodiode. The UV-Vis spectra were recorded using Varian Cary 50 Bio, UV-Visible Spectrophotometer (Varian Inc.) in the range from 200 nm to 800 nm at room temperature. Isothermal calorimetry titrations were performed using The ITC Nano manufactured by TA Instruments, (Lindon, UT, U.S.A.). The reference cell was filled with water. The MCB in phosphate buffer was loaded into a 360 $\mu$L volume of sample cell of the calorimeter and GSH in the same buffer was placed in a 50 $\mu$L syringe. The system was allowed to equilibrate and a stable base line was recorded before initiating and finishing an automated titration through 300 s. The titration experiment consisted of 16 injections of 3 $\mu$L each into the sample cell with 3600 s intervals between injections. The sample cell was stirred at 300 rpm and the temperature of the system was maintained at 25 $^O$C. The voltammetric measurements were recorded using Model PS-205B Potentiostat/Galvanostat and Electrochemical Quartz Crystal Nanobalance, Model EQCN-700 (Elchema, U.S.A.) with a Data Logger and Control System, Model DAQ-716v, operating under Voltscan 5.0 data acquisition and processing software. A double-junction saturated (KCl) Ag/AgCl electrode (Elchema) was used as the reference electrode, Pt wire (Elchema) as the counter electrode and glassy carbon electrode (GCE, Elchema) was used as working electrodes.**

**Quantum mechanical calculations of electronic structures for fluorone black were performed using modified Hartree-Fock methods with 6-31G\* basis set and pseudopotentials, semi-empirical PM3 method, and density functional theory (DFT) with B3LYP functional. The molecular dynamics simulations and quantum mechanical calculations were carried out using procedures embedded in Wavefunction (Irvine, CA, U.S.A.) Spartan 6. The electron density and local density of states (LDOS) are expressed in atomic units, au$^{-3}$, where 1 au = 0.529157 Å and 1 au$^{-3}$ = 6.749108 Å$^{-3}$.**

A glassy carbon substrate immersed in a solution containing 100 μM fluorone in phosphate buffer solution (PBS), pH = 7.4, in 30:70 water:methanol solvent exhibits a well-defined electrooxidation wave beginning at $E$ = 100 mV and with a peak potential at $E_{pa}$ = 201 mV. This wave is irreversible and there is virtually no back reduction observed. However, during the subsequent cycles, the oxidation wave of fluorone increases indicating that fluorone undergoes a slow adsorption on the glassy carbon surface. This is illustrated in Figure 8.
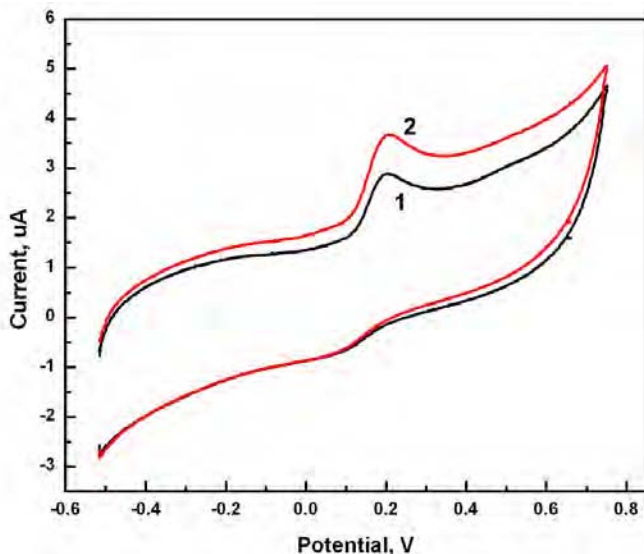


**Figure 8. Cyclic voltammograms for a glassy carbon electrode in 100 μM FB solution: (1) immediately after immersion of a freshly polished electrode and (2) after 3 min of GC exposure to FB solution; 20 mM phosphate buffer (water:methanol = 30:70), pH = 7.4.**

The integration of the amount of charge consumed during the initial voltammogram and that after fluorone adsorption leads to the value $\Delta Q_{an}$ = 132.5 μC/cm$^2$. Assuming that no adsorption has taken place immediately after immersing the electrode in solution, we can ascribe the value of $\Delta Q_{an}$ to the oxidation of adsorbed fluorone black. This value can be compared with the theoretical monolayer charge for densely packed fluorone black film with 3e exchanged in oxidation of 3 OH groups of fluorone black to quinone groups. The theoretical values for different orientations of FB are presented in Table I. They were calculated based on the dimensions of FB molecule obtained from a molecular dynamics (MD) and quantum mechanical (QM) calculations of FB structure and electron density distribution. These dimensions are: *length* = 1.285 nm, *height* = 1.209 nm, and *width* = 0.300 nm.

**Table I. Surface coverage by fluorone black***

| Variable | Units | Orientation | | |
|---|---|---|---|---|
| | | Horizontal | Side-on | Vertical |
| $A$ | nm$^2$ | 1.554185 | 0.38559 | 0.36276 |
| $\Gamma_{mono}$ | molec/cm$^2$ | 6.43E+13 | 2.59E+14 | 2.76E+14 |
| $\gamma_{mono}$ | nmol/cm$^2$ | 0.1069 | 0.4308 | 0.4579 |
| $m_{mono}$ | ng/cm$^2$ | 34.23 | 137.99 | 146.67 |
| $Q_{mono}$** | μC/cm$^2$ | 30.9 | 124.7 | 132.5 |

Symbols: $A$ - area per molecule, $\Gamma_{mono}$ - molecular surface coverage, $\gamma_{mono}$ - molar surface coverage, $m_{mono}$ - monolayer mass, $Q_{mono}$ – monolayer charge.
* Based on MD and QM calculations using Wavefunction Spartan 6 and molecular dimensions: *length* = 1.285 nm, *height* = 1.209 nm, and *width* = 0.300 nm;
** $Q_{mono} = nF\gamma$, where $n = 3$, $F = 96485$ C/equiv.

After preadsorbing FB on the electrode surface, the injection of GSH to the solution results in the increase of the oxidation current in the region of FB wave, as illustrated in Figure 202 b). The shape of the wave remains unchanged which indicates that most likely GSH undergoes an FB-mediated oxidation before it can form adducts with FB by $S_N2$ substitution in one of the positions 1, 4, 8, 5 in the adsorbed FB. The GSH oxidation is irreversible similar to the oxidation of FB. Subtraction of the waves 2 and 1 in Figure 202 a), leads to the difference voltammogram presented in Figure 202 b) which corresponds to the oxidation of GSH. The peak potential $E_{pa}$ = 210 mV. Hence, there is a small difference $\Delta E_{pa}$ = 9 mV between the $E_{pa}$ values for FB and GSH. This is much less than that observed for high concentrations of GSH and when nucleophilic substitution $S_N2$ is completed to form FB-GSH and FB-(GSH)$_2$ adducts.



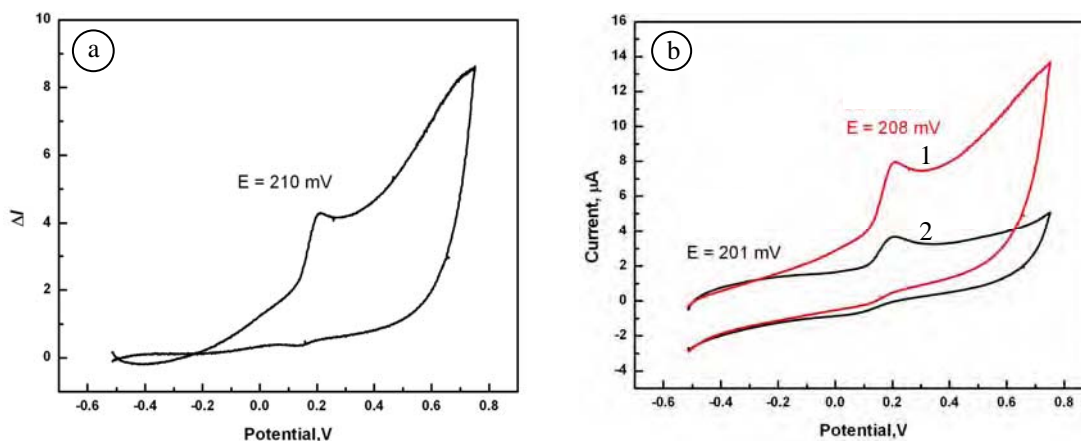Figure 9. (a) CV difference curve for CV of (1) GSH + FB and (2) FB alone, obtained for GC electrode with preadsorbed FB (3 min. in 100 μM FB solution); 0.91 mM GSH, 20 mM PBS (water:methanol = 30:70), pH = 7.4. (b) original CV for (1) and (2).

As seen in Figure 9a, significant electrooxidation of GSH begins from $E$ = 110 mV, but onset of the process is clearly visible already at $E$ = -150 mV.

On the other hand, the FB-mediated electrooxidation of GSH is similar to that we observed for catechol-GSH mixtures, presented in Figure 10. Here, the addition of GSH also results in the increase of the oxidation peak with minimal anodic shift of the peak potential ($\Delta E_{pa} \approx 10$ mV). The reduction peak the ortho-quinone is strongly suppressed by addition of GSH which indicates that it reacts very efficiently with GSH in a redox process in which the quinone moiety is reduced and GSH undergoes a nucleophilic $S_N2$ substitution.
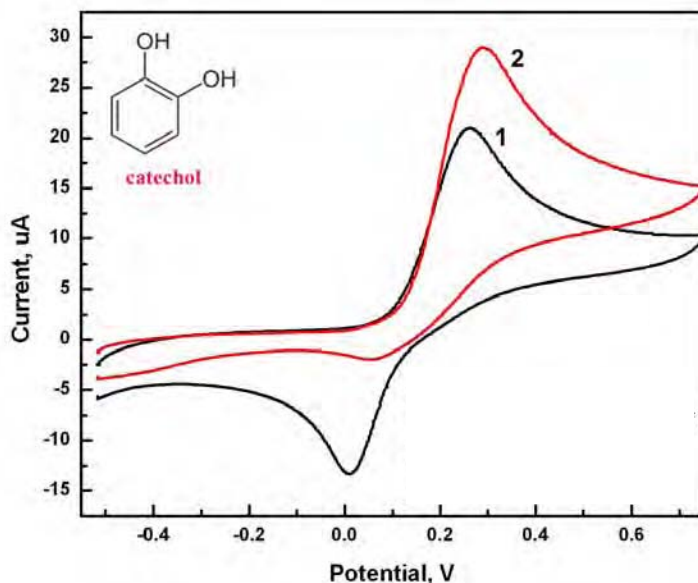


**Figure 10. Cyclic voltammograms for a GC electrode in: (1) 100 µM catechol and (2) 100 µM catechol + 750 µM GSH, in 20 mM phosphate buffer, pH = 7.4.**

In Figure 11, the voltammetric and nanogravimetric characteristics of a bare gold and GSH-capped (AuQC/GSH) piezoelectrodes in 100 µM solution of fluorone black are presented. The cyclic voltammogram for an adsorbed fluorone black on a bare electrode shows three oxidation waves with peak potentials: $E_{an,1} = 0.174$, $E_{an,2} = 0.419$, and $E_{an,3} = 0.654$ V and a reduction peak at $E_{cat} = 0.110$ V. These waves are associated with consecutive oxidation of the three functional -OH groups of the fluorone black. The increase of mass about 35 ng is due to the adsorption of phosphate ions and fluorone black molecules on the surface of the gold electrode (Figure 204a). In Figure 204b, the oxidation wave appears in the potential range from 245 to 478 mV. The changes of mass and current are smaller in comparison with those observed on a bare gold electrode. It indicates: (1) on the immobilization of glutathione on the electrode surface via strong Au-GSH bond formation and also (2) on the formation of FB-GSH adducts in solution.

18
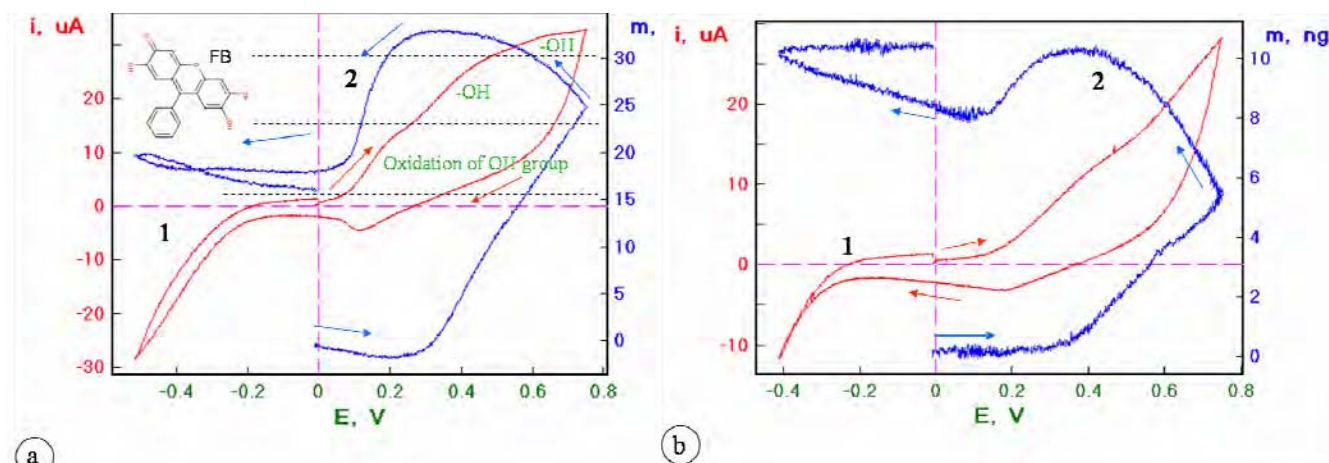
**Figure 11. Current-potential (1) and mass-potential (2) characteristic for AuQC electrode in 100 μM FB solution (70% methanol + 30% phosphate buffer) in the absence (a) and presence (b) 0.4 mM GSH, recorded at scan rate 100 mV/s.**


In Figure 12, typical apparent-mass change transient for the film formation on a QC/Au piezoelectrode is presented. For 33.3 μM FB solution, the adsorption was completed in 35 min and the final mass change of 71.3 ng was observed.
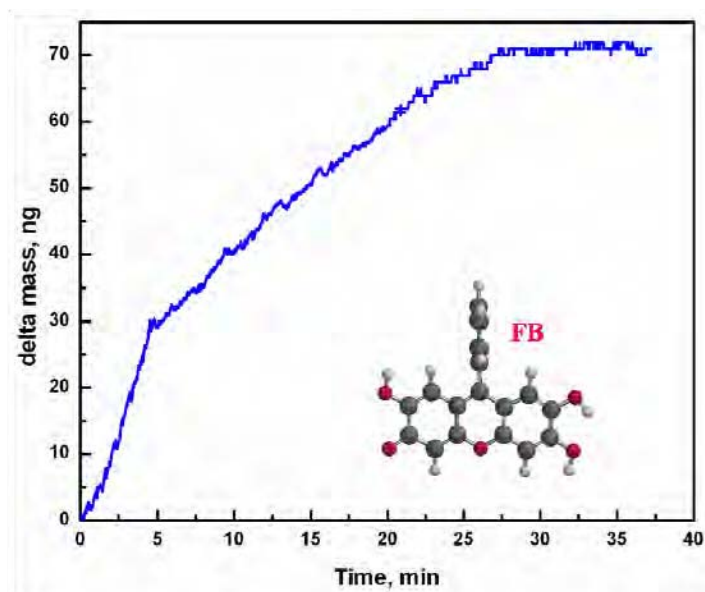


**Figure 12. Nanogravimetric transient for fluorone black adsorption on Au piezoelectrode from 33.3 μM FB solution (70% methanol+30% phosphate buffer); 50 mM phosphate buffer, pH 7.4**

The Resonance Elastic Light Scattering (RELS) and fluorescence measurements have been carried out for possible utilization of these techniques in GSH quantitation using multi-cell arrays. Since the sensor array is composed of a number of cells with printed sensor electrodes, some cells may be used to measure light scattering or fluorescence either from the sample solution or from sensory material. We have detected changes in light reflected from molecularly-template GSH sensors designed during year 1 of the Project. Here, we report on RELS and fluorescence measurements of fluorone black (FB) dye interacting with GSH, as well as the monochlorobimane (MCB) dye which binds specifically GSH.

<u>Fluorone Black.</u>  The absorbance spectrum of FB solutions show small changes in the absorbance maximum structure in the wavelength range 350-500 nm, as illustrated in Figure 13. In the lower wavelength range 200-350 nm, there is clear additivity of absorbances of FB and GSH. The broad absorbance peak observed at ca. 450 nm for FB in aqueous solutions corresponds to two separate electron excitation processes which are well-separated when measurements are performed in pure methanol.
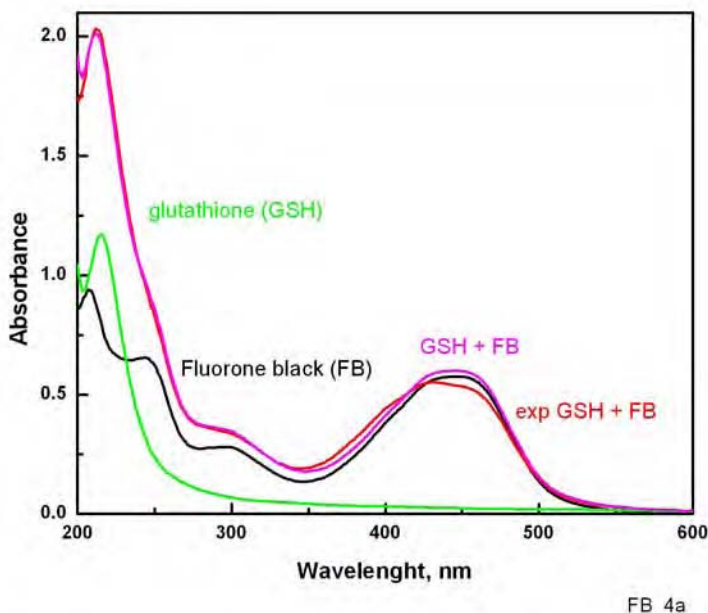


Figure 13.  Absorbance spectra for: (1) FB, (2) GSH, (3) FB + GSH, (4) sum of spectra (1) and (2); $C_{FB}$ = 33.3 µM, $C_{GSH}$ = 0.67 mM, 20 mM PBS buffer pH = 7.4 (water:methanol = 70:30).

In order to evaluate the effect of GSH of this peak structure, we have calculated the difference spectrum between the sum of FB and GSH spectra and the experimental spectrum for a solution of FB + GSH. The difference spectra obtained for several concentrations of GSH and constant concentration of FB are presented in Figure 14. They show positive peak with $\lambda_{max}$ = 383 nm and a negative peak with $\lambda_{max}$ = 458 nm.  This means that the addition of GSH causes a change in the electron excitation energy from 3.23 eV to 2.7 eV. The excitation energy change is then quite large and equals $\Delta E_{ex}$ = 0.53 eV.  The higher excitation energy is concomitant with lowering of the ground state energy, otherwise the adduct formation would not take place. To

estimate how much the ground state is downshifted, we invoke the electrochemical experiments recently published. The shift in the voltammetric peak current of FB upon addition of high concentration of GSH observed by Strongin et al. is on the order of 0.3 V. If one assumes that the ground state is shifted by ca. 0.3 eV then the adduct FB-GSH may not be stable in the excited state since the energy level of the excited FB alone would be lower than that of the adduct by 0.2 eV.
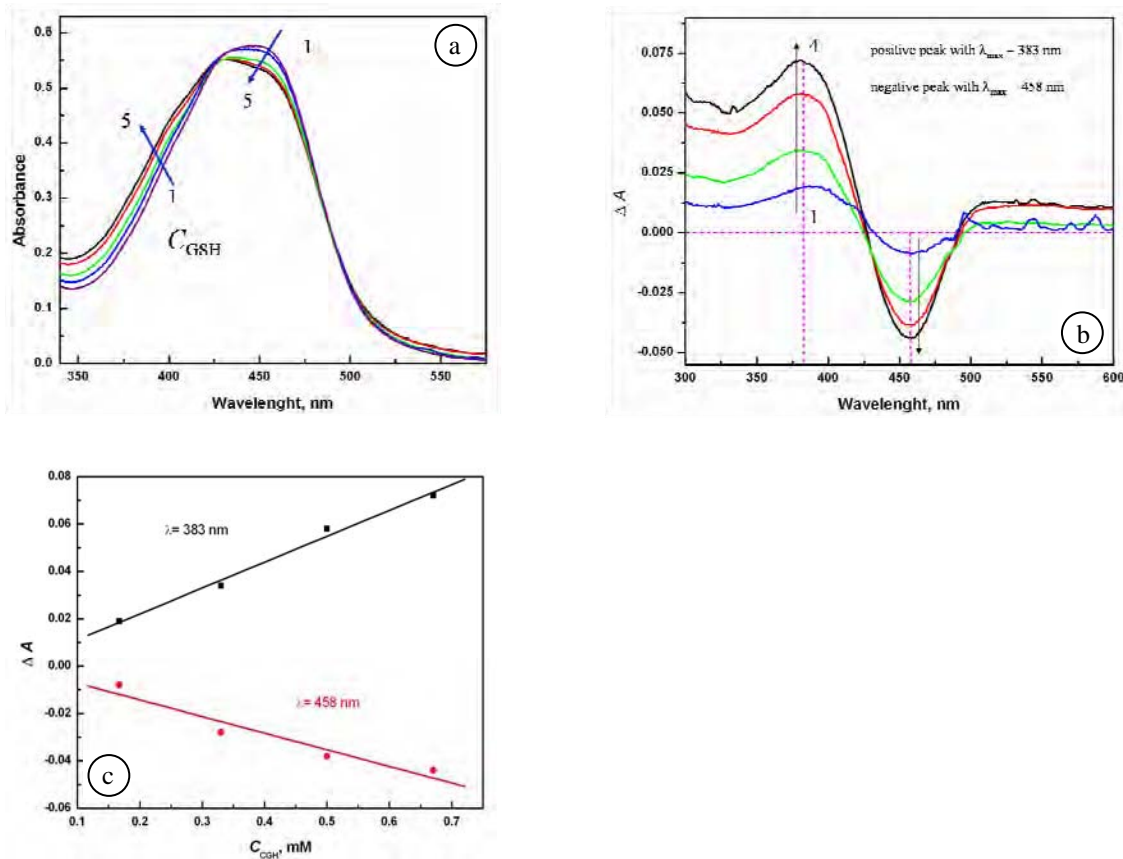


**Figure 14.** (a) Absorbance spectra for 33.3 µM FB in the presence of GSH, $C_{\text{GSH}}$, mM: (1) 0, (2) 0.17. (3) 0.33, (4) 0.5, (5) 0.67; (b) Absorbance difference spectra for 33 µM FB + $x$ GSH solutions minus sum of the spectra for individual components, $x$ [mM]: (1) 0.17, (2) 0.33, (3) 0.5, (4) 0.67; 20 mM PBS buffer pH = 7.4 (water : methanol = 70:30); (c) dependence of $\Delta A$ vs. $C_{\text{GSH}}$.

The RELS and fluorescence spectroscopy of FB solution upon addition of GSH reveals large changes in light scattering and very small changes in FB fluorescence. This is presented in Figure 15 for constant $C_{\text{FB}} = 3.33$ µM and $C_{\text{GSH}}$ changing from 0 to 833 µM. The RELS intensity $I_{\text{sc}}$ changes linearly with increasing concentration of GSH indicating on an increase of size and concentration of scattering particles. At the same time, the fluorescence of FB remains unchanged in a wide concentration range of FB, as illustrated in Figures 16a,b.

21
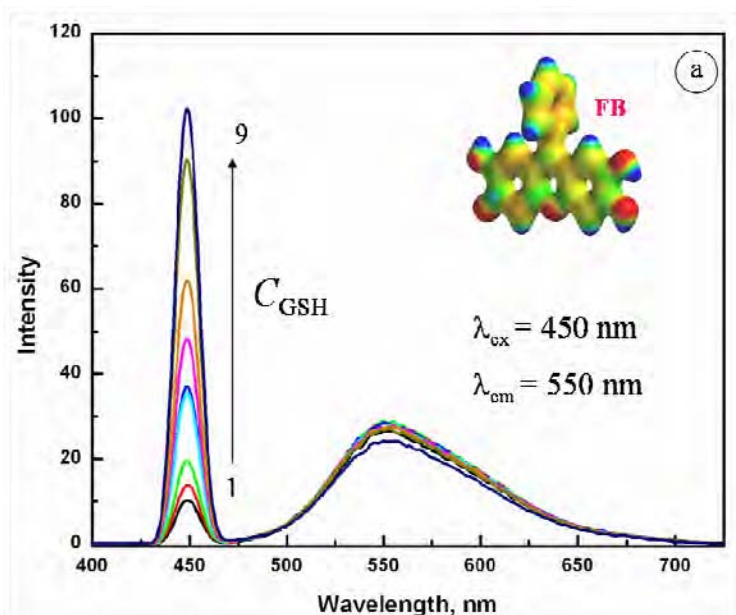
**Figure 15. RELS and fluorescence spectra of 3.33 μM FB + x GSH obtained for the excitation at $\lambda_{ex}$ = 450 nm, $x$ [μM] from 0 to 833.**
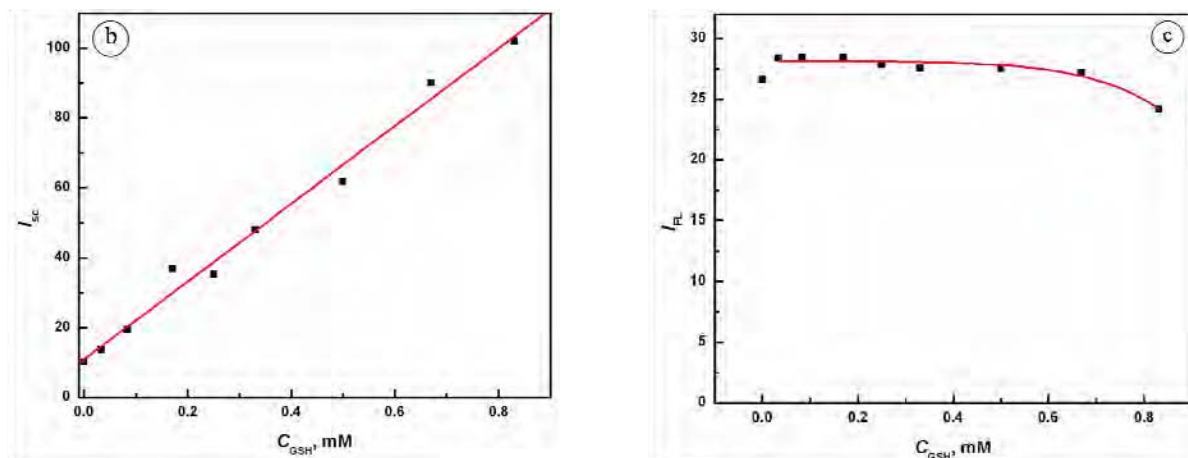


**Figure 16. Dependence of RELS (a) and fluorescence (b) intensity on $C_{GSH}$ obtained for FB + GSH solutions; $\lambda_{ex}$ = 450 nm, $C_{FB}$ = 3.33 μM, PBS, pH = 7.4**

**Monochlorobimane.** The substitution of Cl atom in monochlorobimane (MCB) is very specific to GSH and thus it was studied for possible inclusion in oxidative stress biomarker sensor arrays. The absorbance and fluorescence measurements have been performed. The binding constant of GSH to MCB was determined by means of fluorescence and isothermal calorimetry titration (ITC) techniques.

The UV-Vis spectra were recorded for increasing concentration of monochlorobimane (MCB) from 0 to 20 μM as illustrated in Figure 17a. The stock solutions of 1 mM monochlorobimane in 20 mM phosphate buffer pH 7 was used in these experiments. There is a major absorbance band observed with $\lambda_{max}$ = 395 nm. The absorbance maximum increases linearly with $C_{MCB}$. The linear regression equation is: $A$ = 0.00617 $C_{MCB}$ - 0.00107, with a correlation coefficient of $R$ = 0.9989, where $A$ is the absorbance, and $C_{MCB}$ is the MCB concentration in [μM] (Figure 17b).

22
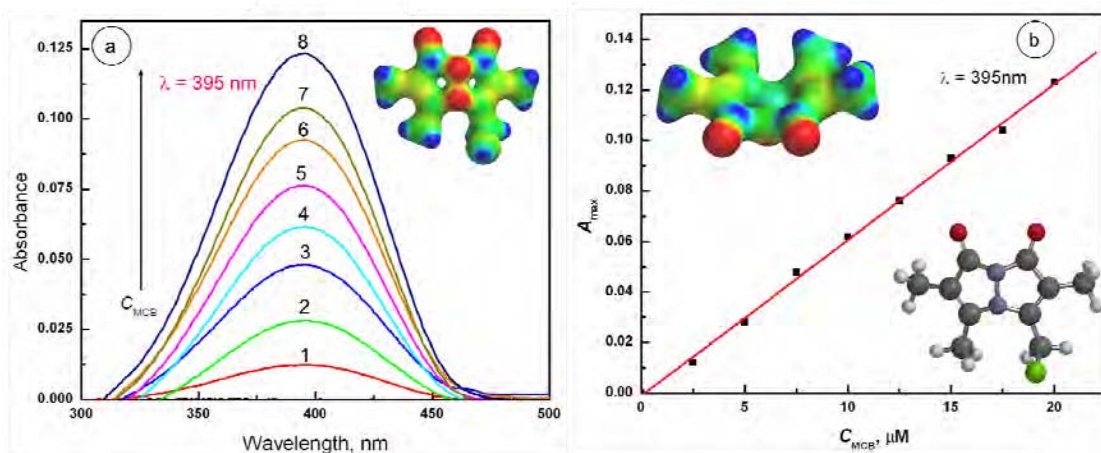
**Figure 17. (a) Absorbance spectra of monochlorobimane, recorded in 20 mM phosphate buffer pH 7.43, for $C_{MCB}$ [μM]: (1) 0, (2) 2.5, (3) 5, (4) 7.5, (5) 10, (6) 12.5, (7) 15, (8) 17.5, (9) 20; (b) dependence of $A_{max}$ vs. $C_{MCB}$.**

It is well known that the essentially nonfluorescent halogenated bimane molecules form fluorescent GSH-bimane adducts with glutathione (1). Figure 18 shows the temporal evolution of fluorescence emission spectra for 0.33 mM MCB and 0.33 mM GSH in 20 mM phosphate buffer, pH 7.4 with excitation wavelength $\lambda_{ex}$ = 395 nm and emission wavelength $\lambda_{em}$ = 485 nm. Fluorescence maximum increases without reaching the saturation value during two hour experiments. Therefore, we can assume that process of conjugation of GSH with MCB has not completed. The major reactive species of GSH with MCB at pH = 7.4 is the anion. The GSH is negatively charged due to dissociated carboxylic groups (COO⁻) of glutamate and glycine residue aminoacids and protonated  -amino group (-NH₃⁺) (pK₁ = 2.04 (glutamate–COOH), pK₂ = 3.4 (glycine–COOH), pK₃ = 8.72 (–SH group), pK₄ = 9.49 (– NH₂ group)).
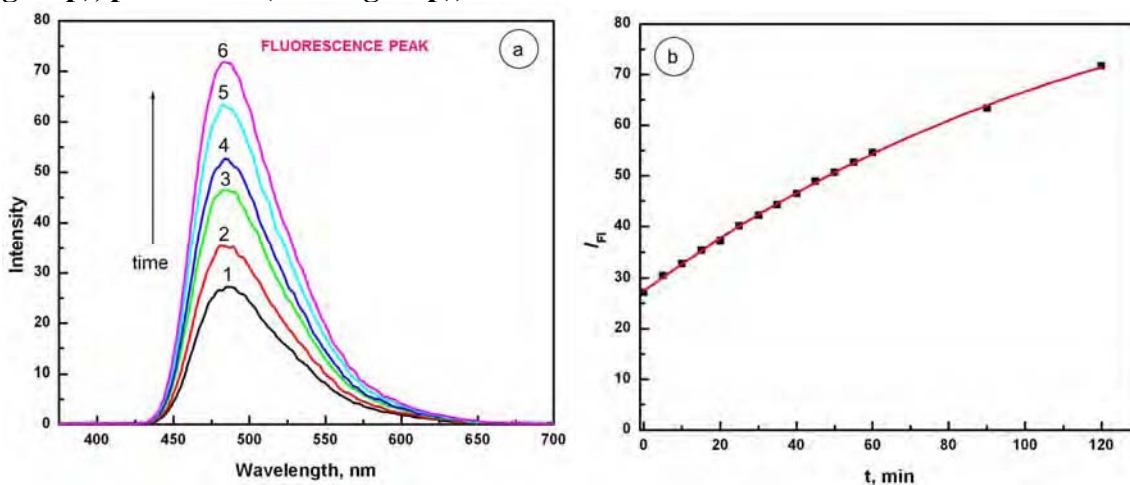


**Figure 18. (a) Temporal evolution of fluorescence emission intensity recorded after mixing monochlorobimane solution with GSH, in 20 mM phosphate buffer pH 7.43 in time; time, [min]: (1) 0, (2) 15, (3) 40, (4) 55, (5) 90, (6) 120; $\lambda_{ex}$ = 395 nm, $\lambda_{em}$ = 485 nm; $C_{MCB}$ = 330 μM, $C_{GSH}$ = 330 μM, final concentrations.**
**(b) Dependence of $I_{FL}$ vs. time.**
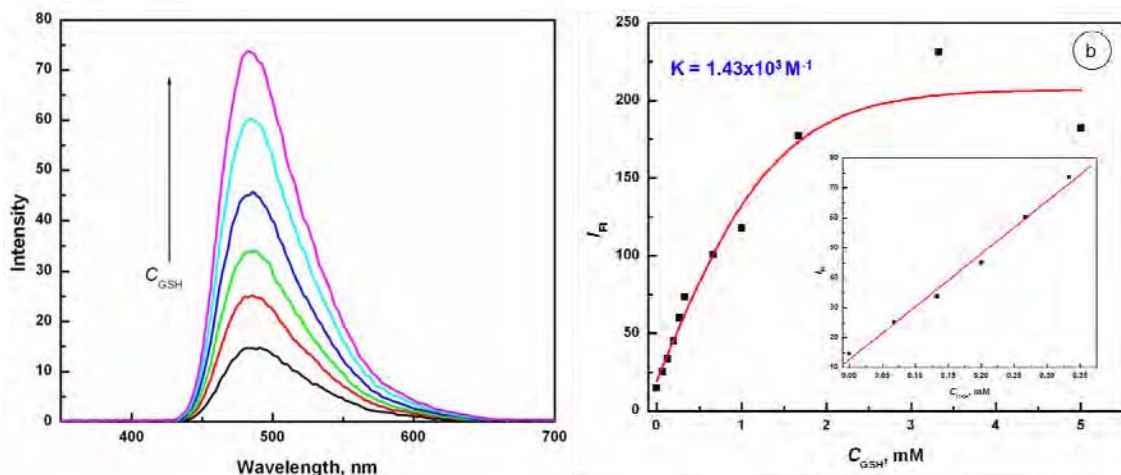
**Figure 19.** (a) Fluorescence spectra for 330 μM monochlorobimane solution after adding different concentrations of glutathione, measured after 50 min of the interaction time, $C_{GSH}$ [μM]: (1) 0, (2) 67, (3) 133, (4) 200, (5) 270 (6) 333; (b) dependence of $I_{FL}$ vs. $C_{GSH}$; inset: linear dependence for lower concentration range (0 - 333 μM of GSH).

Figure 19 presents typical fluorescence spectra for MCB-GSH adducts at constant excitation wavelength $\lambda_{ex}$ = 395 nm. The increase of concentration of GSH solutions results in the enhancement of emission spectrum of MCB. The fluorescence intensity $I_{FL}$ increases from $I_{FL,\,min}$ = 14.72 to the final value $I_{FL,final}$ = 181.95 at the saturation established for $C_{GSH}$ > 1.67 mM. The linear response was observed in the range from 0 to 0.33 mM concentration of GSH, with a correlation coefficient R = 0.995. In the full range of concentrations of GSH, the dependence of $I_{FL}$ vs. $C_{GSH}$ is sigmoidal with a Boltzmann function fitted to the experimental data:

$$I_{FL} = A_2 + (A_1 - A_2) / (1 + \exp\{(C - C_{1/2}) / s\})$$

where $A_1$, $A_2$ - are the lower and higher $I_{FL}$, C is concentration, $s$ is the slope parameter.

Mono(haloalkyl)bimanes react with glutathione to form a substitution product, monoalkylated glutathione (RSG) (2). Binding constant of GSH to MCB from fluorimetric measurements was determined as $1.43 \times 10^3\,M^{-1}$.

$$K = \frac{[C_{GSH-MCB}]}{[C_{free,GSH}][C_{free,MCB}]}$$

where:

$$C_{free,GSH} = C_{GSH} {}^- C_{GSH-MCB}$$

$$C_{free,MCB} = 0.33\ {}^- C_{GSH-MCB}$$

To confirm the obtained value of the binding constant, microcalorimetric measurements were performed using and Isothermal Titration Calorimetry (ITC). A typical ITC profile for the binding of GSH to MCB using a Nano ITC is shown in Figure 20. It corresponds to the signal (heat) produced following each addition of GSH (stock solution 30 mM) to 4 mM MCB in 20 mM phosphate buffer at pH 7.43

with 16 aliquots (3 µL each). The bottom panel in this figure shows the integration of the heats over the time course of the experiment. The heats (in µJ) integrated over each peak are plotted against the mole ratio of reduced GSH to MCB. From fitting of experimental data to a model of independent sites, the stoichiometry of the reaction was obtained as 1:1, the binging constant K = 1.31 x $10^3$, and the standard enthalpy changes ΔH = -106.4 kJ/mol. Thus, the reaction of GSH with MCB is exothermic.
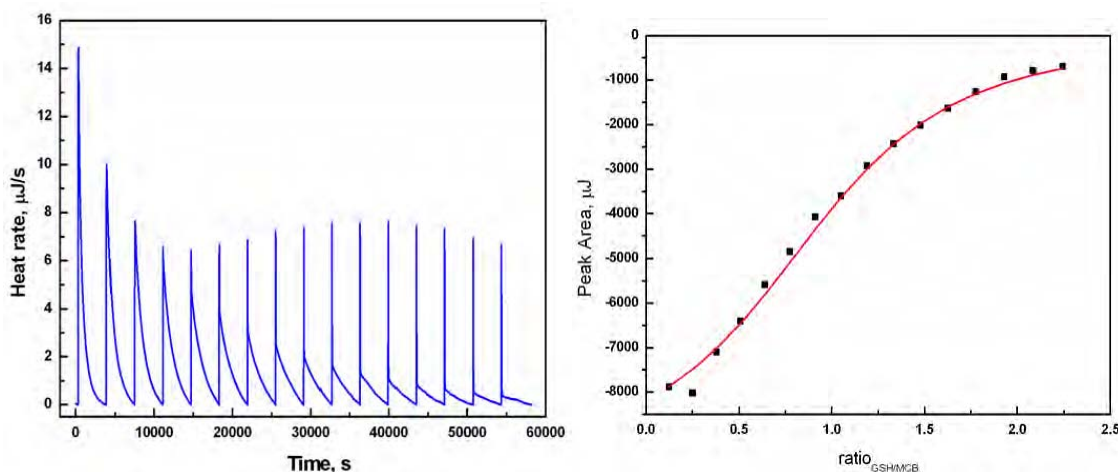


**Figure 20. Isothermal titration characteristic for binding of glutathione to monochlorobimane, in 20 mM phosphate buffer pH 7.43. The experiment consisted of 16 injections of 3 µL each of a 30 mM GSH. GSH was injected into a sample cell (volume 185 µL) containing 4 mM of MCB. Injections were at 1 h intervals.**

Further efforts will be directed toward finding new catalysts and modifying surface morphology to form nanstructures that would be able to enhance the surface electrocatalytic properties toward GSH oxidation. These results will be incorporated in designing and testing sensor arrays in year 3 of the Project.

The results described above will be presented at the Electrochemical Society Meeting in Montrel, Canada, 2011 and are in preparation for publication in a peer-reviewed journal.

b) construction of coumarin derivative microsensors and testing their performance (Months 12-18);

**The microsensors based on coumarin derivatives were constructed using different substrates to test their electrocatalytic properties. We have found that many coumarins can be reduced on glassy carbon electrodes (GC) and on lead-tin alloy ($Sn_{63}Pb_{37}$) electrode while graphite and $Sn_{96.5}Ag_3Cu_{0.5}$ show no electrocatalytic properties. In Figures 21a,b presented are cyclic voltammograms (CV) for a $Sn_{63}Pb_{37}$ alloy electrode in 50 mM phosphate buffer solution (PBS), showing the background at negative potentials and the oxide formation/reduction region, respectively.**
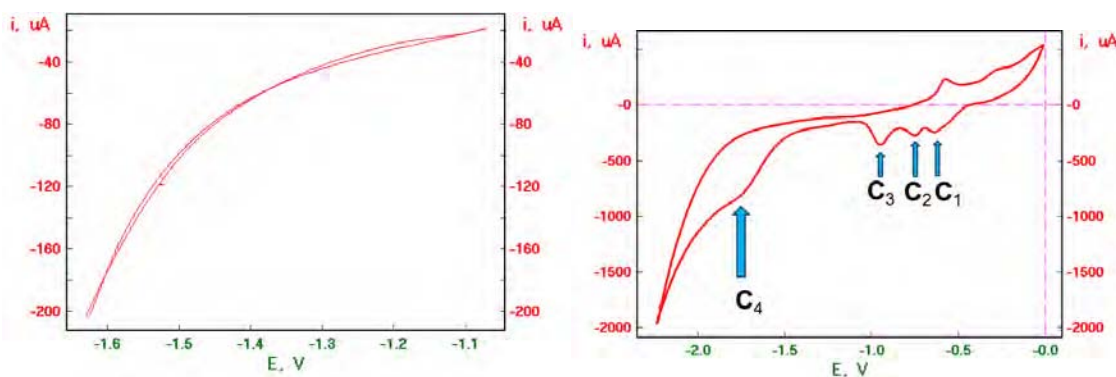


**Figure 21. Cyclic voltammograms for a $Sn_{63}Pb_{37}$ alloy electrode in 50 mM PBS: (a) background at negative potentials and (b) oxide formation/reduction region (cathodic peaks $C_1$, $C_2$, $C_3$) with a coumarin 4 (CM4) reduction wave $C_4$ at $E$ = -1.7 V vs. Ag/AgCl, $C_{CM4}$ = 100 μM; v = 100 mV/s.**

**As shown in Figure 21 (right panel), coumarin 4 (CM4) added to a solution is reduced in an irreversible process in the negative potential range showing a reduction wave $C_4$ with $E_{pc}$ = -1.7 V vs. Ag/AgCl. By limiting the potential scan to the range $E$ < -0.84 V, the formation of oxides on the electrode surface can be avoided and voltammograms for a clean alloy surface can be obtained.**
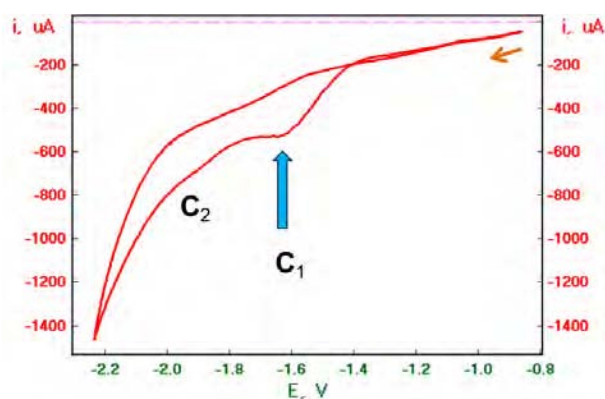


**Figure 22. Cyclic voltammogram for a $Sn_{63}Pb_{37}$ alloy electrode in 200 μM CM4 + 50 mM PBS, recorded on a surface undistorted by oxide formation/reduction; v = 100 mV/s.**

**This is illustrated in Figure 22 for a $Sn_{63}Pb_{37}$ alloy electrode in 200 μM CM4 + 50 mM PBS solution. It is seen that coumarin 4 reduction $C_1$ on the surface that is**

undistorted by oxide formation/reduction takes place at a slightly lower overpotential ($E_{pc}$ = -1.65 V) with a tale extending to more negative potentials, $C_2$.

The reduction of coumarins on a glassy carbon electrode and $Sn_{96.5}Ag_3Cu_{0.5}$ alloy electrode is not catalyzed as well as on a $Sn_{63}Pb_{37}$ alloy electrode. This is illustrated in Figures 504 and 505 for coumarin 120 and coumarin 1.
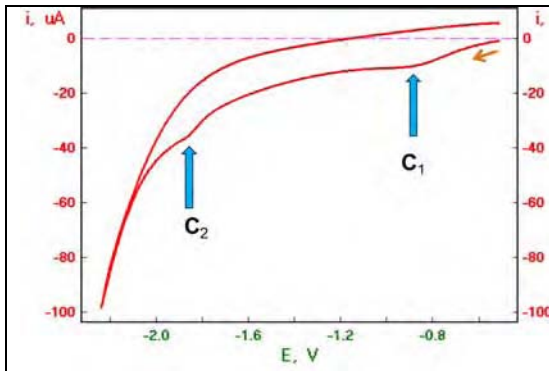
|  |  |
|---|---|
| **Figure 23. Cyclic voltammogram for a GC electrode in 100 μM CM120 + 50 mM PBS; $v$ = 100 mV/s.** | **Figure 24. Cyclic voltammogram for a GC electrode in 100 μM CM1 + 100 μM CM120 + 50 mM PBS; $v$ = 100 mV/s.** |
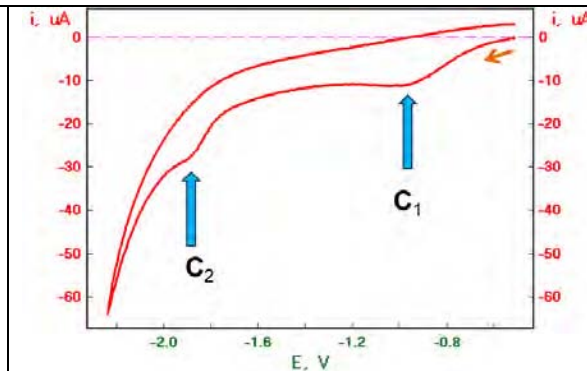
In these Figures the process $C_1$ is associated with reduction of adsorbed oxygen species and peak $C_1$ be removed by cathodization and solution deoxygenation. The cathodic peak $C_2$ is due to the reduction of coumarins 120 and 1. The peak potential is shifted toward a potential $E_{pc}$ = -1.85 V, which is about 200 mV more negative than that observed for a $Sn_{63}Pb_{37}$ alloy electrode. The electrocatalytic properties of a $Sn_{63}Pb_{37}$ alloy electrode toward reduction of coumarins is convenient for sensor designs since this alloy can be readily applied on copper traces in printed circuits.

Further efforts will be directed toward modifying the electrode morphology and applying nanomaterials to improve electrocatalytic properties of the sensors. The small peaks shown in cyclic voltammograms can be expanded into large peaks by applying square wave voltammetry or differential pulse voltammetry. We will apply these techniques in the final stage of sensor testing in year 3 of the Project after selection of the sensory films to be used in sensor arrays.

c) study of downscaling fluorone and coumarin based probes for sensor arrays (Months 18-30);

In the first stage of these investigations, we have designed printed circuits for a single sensor with dual interdigitated electrodes. The electrode width of 200 μm with interelectrode spacing of 200 μm was used. The sensor design is presented in Figure 25. The sensors were electroplated with a thin Au layer and different sensory films were deposited to test the sensor performance. These microsensors were applied in direct measurements of electrocatalytic activity of $Sn_{63}Pb_{37}$ and $Sn_{96.5}Ag_3Cu_{0.5}$ alloy electrodes described in section 1(b).
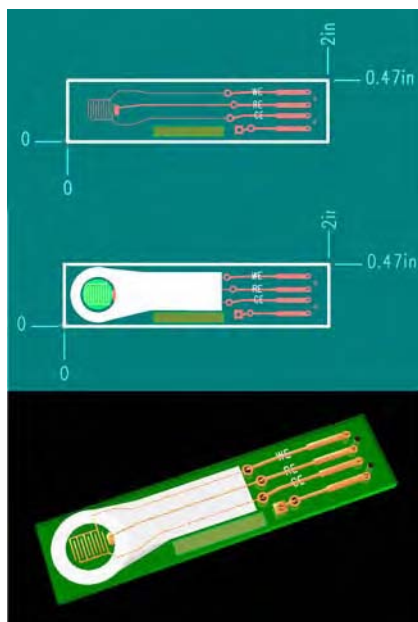
**Figure 25. Design of a microsensor with interdigitated electrodes.**

**Further investigations are underway and will be finished during the third year of the project.**

d) software development for artificial neural networks utilizing experimental concentration dependences of sensor signals (neuron firing functions) (Months 18-24);
**The software for artificial neural networks has been designed and tested on artificial data sets.**

e) construction of multisensor arrays based on sensors with different responses to GSH, GSSG, thiols and testing using multi-channel potentiostat with multi-sensor data acquisition system (Months 18-24);
**The multisensory arrays have been designed based on the concepts similar to those used in constructing microsensors. A multisensor array with six pairs of interdigitated electrodes has been constructed, as illustrated in Figure 26. One of the electrodes of each interdigitated pair was connected to the common and the other had an independent connection. This arrangement enabled measurements of lateral conductance independently in each sensory film with reduced interconnections. The experience to operate on small sensor areas and to avoid inter-sensor contamination has been gained. In particular, the problem of hydrophobizing the insulating silk-screened surfaces has been addressed. The durability tests have also been carried out to determine viability of reusing the sensors after sensory film removal or analyte-antibody adduct dis-association with 0.2 M glycine solution at pH = 3.**

28
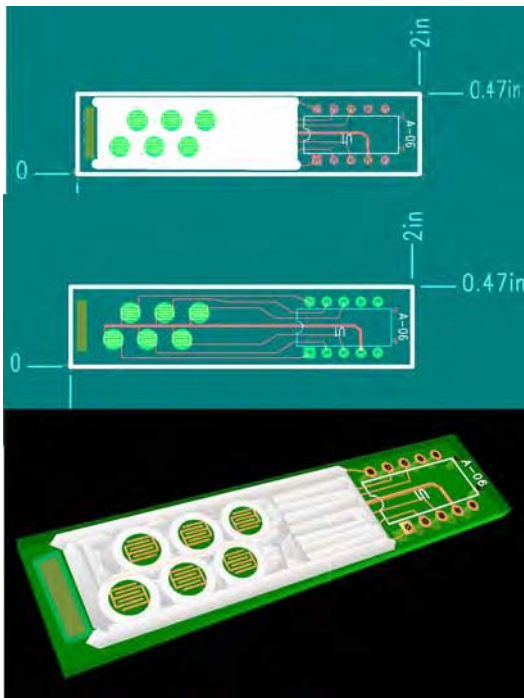
**Figure 26. Design of a microsensor array with pairs of interdigitated electrodes.**

The experimental setup with a six-channel potentiostat/galvanostat was prepared for simultaneous voltammetric analysis utilizing all six sensors of the sensor array. The potentiostat system allows for the use of a single counter electrode and a single reference electrode which reduces the number of electrodes for a six-cell array chip from 18 to 8. Due to the specificity of different experiment control for different sensors and separate data processing, the system control software will have to be modified, which we hope to achieve during year 3 of the Project. Therefore, in the investigations, we analyzed all sensors in the array separately, one at a time, except for a series of arrays with sensors of the same type, differing only in sensory film composition. Typical sensor arrangement examined in this work involved: (1) molecularly templated conductive polymer sensor synthesized by in-situ electropolymerization of ortho-phenylenediamine (oPD) in the presence of glutathione (GSH); (2) GSH-templated conductive polymer sensor synthesized by in-situ electropolymerization of polypyrrole (PPy) in the presence of GSH; (3,4) monoclonal anti-GSH antibody sensors; (5) $Sn_{63}Pb_{37}$ alloy based sensor or carbon with transition metal oxide catalyst-based sensor; (6) glassy carbon powder or unmodified PPy sensor. The procedure of preparing these sensors is rather laborious due to small size of sensors and manual operation. Hence, only a limited number of arrays has been prepared and tested. To gain more experience in handling sensor arrays, we have also constructed arrays consisting of sensors of the same kind, either identical or differing slightly in composition, for instance a sensor array was obtained by modifying the surface of sensors with AET SAM followed by immobilization of anti-GSH monoclonal antibody with slow withdrawal of the array chip from solution producing a concentration gradient of an antibody. This type of an approach is simpler than that of individual sensor preparation using different reagents and procedures which may result in cross-contamination.

The microsensor arrays described above, as well as others built on the same principle that will be subsequently constructed, will be employed in the analysis of

**array responses using algebraic equations and artificial neural networks while testing real-world samples (extracts from Projects 1-2) during the third year of the Project.**

f)  testing of 20 samples, 1 mL extracts, from Projects 1 and 2 using sensor arrays (Months 24-36); **N/A**
g)  analysis of array responses using algebraic equations and artificial neural networks (Months 24-36); **N/A**

**Key Research Accomplishments**

- Glutathione- and homocysteine-sensitive ligand exchange processes at core-shell gold nanoparticles have been utilized for rapid nanoparticle functionalization for applications in designing nanostructure-enhanced sensors.

- Highly selective assays for glutathione and homocysteine based on specific plasmonic microenvironment have been proposed.

- A novel biosensor based on an anti-GSH monoclonal antibody immobilized on a gold substrate with a positive potential barrier film has been designed and operated as a piezoimmunosensor or a voltammetric sensor with free redox ion probe.

- A fluorone black sensor for GSH has been developed and the GSH oxidation enhancement via fluorone-mediated electron transfer has been demonstrated.

- Highly sensitive platform for GSH and cysteine in the form of a molecular beacon has been proposed.

## Reportable Outcomes

(1) Paper published: "Rapid functionalization of metal nanoparticles by moderator-tunable ligand-exchange process for biosensor designs", M. Stobiecka, M. Hepel, *Sensors Actuators B*, 149 (2010) 373-380.

(2) Paper published: "Ligand exchange effects in gold nanoparticle assembly induced by oxidative stress biomarkers: Homocysteine and cysteine", M. Stobiecka, J. Deeb, M. Hepel, *Biophys. Chem.*, 146 (2010) 98-107.

(3) Paper published: "Resonance Elastic Light Scattering (RELS) Spectroscopy of Fast Non-Langmuirian Ligand-Exchange in Glutathione-Induced Gold Nanoparticle Assembly", M. Stobiecka, K. Coopersmith, M. Hepel, *J. Colloid Interface Sci*, 350 (2010) *168-177.*

(4) Paper in press: "Multimodal coupling of optical transitions and plasmonic oscillations in rhodamine B modified gold nanoparticles", M. Stobiecka, M. Hepel, Phys. Chem. Chem. Phys., (2010) (*in press*).

(5) Presentations:

1. Resonance Elastic Light Scattering Assays for Oxidative Stress Based on Selectively-Crosslinked Gold Nanoparticle Network Assembly, Maria Hepel and Magdalena Stobiecka, 4th International Conference on Oxidative/Nitrosative Stress and Disease, October 28-30, 2009, New York

2. Study of Resonance Elastic Light Scattering and Fluorescence Energy Transfer in Rhodamine B Modified Spherical Au Nanoparticles and Nanorods, Magdalena Stobiecka, Kaitlin Coopersmith, and <u>Maria Hepel</u>. Materials Research Society Meeting, Boston, November 30-December 4, 2009

3. Resonance Energy Transfer in a Multicomponent Fluorescent Dye System Influenced by Gold Nanorod Quadrupole Surface Plasmon Coupling, <u>Kaitlin Coopersmith</u>, Magdalena Stobiecka, and Maria Hepel, Pittsburgh Conference on Analytical Chemistry, Orlando, FL, February 28-March 5, 2010

4. Flow-cell nanogravimetric immunosensing for the detection of glutathione, Magdalena Stobiecka, <u>Zachary Reed</u>, Justine Barcomb, and Maria Hepel, the North-East Regional Meeting of American Chemical Society NERM-2010, 2-5 June, 2010, Potsdam

5. Nanomaterial Surface Energy Transfer (NSET) between Multiple Fluorescent Dyes and Gold Nanoparticles. Kaitlin Coopersmith, Magdalena Stobiecka and Maria Hepel, State University of New York at Potsdam, the North-East Regional Meeting of American Chemical Society NERM-2010, 2-5 June, 2010, Potsdam

6. Resonance Elastic Light Scattering (RELS) Spectroscopy for Monitoring Biomolecule-Induced Gold Nanoparticle Assembly. Maria Hepel and Magdalena Stobiecka, the North-East Regional Meeting of American Chemical Society NERM-2010, 2-5 June, 2010, Potsdam

7. Novel antibody-based nanostructured biosensors for glutathione oxidative-stress biomarker, Zachary Reed, Nicholas Trombley, Robert Wallace, Magdalena Stobiecka, and Maria Hepel, National Meeting of the American Chemical Society, Boston, MA, August 22-26, 2010

8. Fluorescence resonance energy transfer between functionalized Coumarin dyes and gold nanoparticles, Kaitlin Coopersmith, Magdalena Stobiecka, and Maria Hepel, National Meeting of the American Chemical Society, Boston, MA, August 22-26, 2010

9. Detection of homocysteine based on gold nanoparticle plasmonic coupling monitored by elastic light scattering, Magdalena Stobiecka, Jeffrey Deeb, and Maria Hepel, National Meeting of the American Chemical Society, Boston, MA, August 22-26, 2010

10. Novel ligand-exchange technique for rapid functionalization of monolayer-protected gold nanoparticles, Zachary Reed, Robert Wallace, Sara Cutler, Magdalena Stobiecka, and Maria Hepel, National Meeting of the American Chemical Society, Boston, MA, August 22-26, 2010.

11. "Resonance Elastic Light Scattering and Plasmonic Phenomena in Glutathione-Mediated Gold Nanoparticle Assembly", Amanda Prance[a], Zachary Reed[a], Magdalena Stobiecka[a], and Maria Hepel, *The Electrochemical Society Meeting,* Vancouver, Canada, April 25-30, 2010.

## Conclusions

The investigations of interactions between biomarkers of oxidative stress and dye molecules from the group of xanthene, coumarin and monochlorobimane have enabled designing new sensor types for these biomarkers. A novel monoclonal anti-GSH antibody-based piezosensors with positive potential barrier have been developed and shown to have higher mass response to GSH-capped gold nanoparticles than to GSH alone. The functionalized gold nanoparticle carriers may be considered in future for extraction and accumulation of analytes from samples. The immunosensors with positive potential barrier can also operate as voltammetric sensors with ferricyanide ion as the redox probe. Another biorecognition based sensing platform has been developed based on molecular beacon which shows high sensitivity and selectivity toward GSH and cysteine in a matrix of amino acids. For further development of microsensors, we have designed printed circuits for microsensor chips and performed initial testing of the design. Printed circuits for sensor arrays have also been designed and fabricated. The arrays with interdigitated electrodes will enable different kinds of sensors to be embedded within the array in further studies during the third year of the Project.

## References

[1] M. Stobiecka, J. Deeb, M. Hepel, Ligand exchange effects in gold nanoparticle assembly induced by oxidative stress biomarkers: Homocysteine and cysteine, *Biophys. Chem.*, 146 (2010) 98-107.
[2] M. Stobiecka, M. Hepel, Rapid functionalization of metal nanoparticles by moderator-tunable ligand-exchange process for biosensor designs, *Sensors Actuators B*, 149 (2010) 373-380.
[3] M. Stobiecka, K. Coopersmith, M. Hepel, Resonance Elastic Light Scattering (RELS) Spectroscopy of Fast Non-Langmuirian Ligand-Exchange in Glutathione-Induced Gold Nanoparticle Assembly, *J. Colloid Interface Sci*, 350 (2010) *168-177*.
[4] J. Ryu, H.A. Joung, M.G. Kim, C.B. Park, Surface plasmon Resonance Analysis of Alzheimer's $\beta$-Amyloid Aggregation on a Solid Surface: From Monomers to Fully-Grown Fibrils, *Anal.Chem.*, 80 (2008) 2400-2407.
[5] X. Sun, P. He, S. Liu, J. Ye, Y.F. Y., Immobilization of single-stranded deoxyribonucleic acid on gold electrode with self-assembled aminoethanethiol monolayer for DNA electrochemical sensor application, *Talanta*, 47 (1998) 487-495.
[6] S.G. Wang, R. Wang, P.J. Sellin, Q.Z. Q., DNA biosensors based on self-assembled carbon nanotubes, *Biochem. Biophys. Res. Comm.*, 325 (2004) 1433-1437.
[7] S.I. Imabayashi, M. Iida, D. Hobara, Z.Q. Feng, K. Niki, T. Kakiuchi, Reductive desorption of carboxylic-acid-terminated alkanethiol monolayers from Au(111) surfaces, *Journal of Electroanal. Chem.*, 428 (1997) 33-38.
[8] H. Radecka, I. Szymańska, M. Pietraszkiewicz, O. Pietraszkiewicz, H. Aoki, Y. Umezawa, Intermolecular ion-channel sensors using gold electrodes immobilized with macrocyclic polyamines for voltammetric detection of adenine nucleotides, . *Chem.Anal.(Warsaw)*, 50 (2005) 85-102.
[9] E. Brynda, Methods for attachment of antibodies onto optical biosensors, in: F. Baldini (Ed.) *Optical Chemical Sensors*, pp. 387–401.
[10] M. Stobiecka, M. Hepel, J. Radecki, Transient conformation changes of albumin adsorbed on gold piezoelectrodes, *Electrochim. Acta*, 50 (2005) 4873-4887.

[11] K. Rezwan, L.P. Meier, M. Rezwan, J. Voros, M. Textor, L.J. Gauckler, Bovine serum albumin adsorption onto colloidal $Al_2O_3$ particles: A new Model based on zeta-potential and UV-Vis measurements, *Langmuir*, 20 (2004) 10055-10061.

[12] S.H. Brewer, W.R. Glomm, M.C. Johnson, M.K. Knag, S. Franzen, Probing BSA binding to citrate-coated gold nanoparticles and surfaces, *Langmuir*, 21 (2005) 9303-9307.

[13] A. Amara, M. Coussemacq, M.Geffard, Antibodies to reduced glutathione, *Brain Res.*, 659 (1994) 237-242.

[14] M. Wąsowicz, S. Viswanathan, A. Dvornyk, K. Grzelak, B. Kłudkiewicz, H.R. H., Comparison of electrochemical immunosensors based on gold nano materials and immunoblot techniques for detection of histidine-tagged proteins in culture medium, *Biosensors and Bioelectronics*, 24 (2008) 284-289.

[15] M. Stobiecka, M. Hepel, Multimodal coupling of optical transitions and plasmonic oscillations in rhodamine B modified gold nanoparticles, *Phys. Chem. Chem. Phys.*, (2010) (*in press*).

## Appendix

A. Paper published: "Rapid functionalization of metal nanoparticles by moderator-tunable ligand-exchange process for biosensor designs", M. Stobiecka, M. Hepel, *Sensors Actuators B*, 149 (2010) 373-380.

B. Paper published: "Ligand exchange effects in gold nanoparticle assembly induced by oxidative stress biomarkers: Homocysteine and cysteine", M. Stobiecka, J. Deeb, M. Hepel, *Biophys. Chem.*, 146 (2010) 98-107.

C. Paper published: "Resonance Elastic Light Scattering (RELS) Spectroscopy of Fast Non-Langmuirian Ligand-Exchange in Glutathione-Induced Gold Nanoparticle Assembly", M. Stobiecka, K. Coopersmith, M. Hepel, *J. Colloid Interface Sci*, 350 (2010) *168-177*.

D. Paper in press: "Multimodal coupling of optical transitions and plasmonic oscillations in rhodamine B modified gold nanoparticles", M. Stobiecka, M. Hepel, Phys. Chem. Chem. Phys., (2010) (*in press*).

# Rapid functionalization of metal nanoparticles by moderator-tunable ligand-exchange process for biosensor designs

Magdalena Stobiecka, Maria Hepel*

*Department of Chemistry, State University of New York at Potsdam, Potsdam, NY 13676, USA*

### ABSTRACT

A new method for rapid functionalization of metal nanoparticles based on a moderator-tunable 2D nucleation and growth of ligand-exchange domains has been developed for the design of biosensors with nanoparticle-enhanced sensory films and other applications. The proposed functionalization of gold nanoparticles proceeds through the nucleation and avalanche growth of ligand-exchange domains in the self-assembled monolayer film on a gold nanoparticle surface. The nucleation and growth is controllable by a moderator molecule. The experimental system described presents a ligand-exchange process at citrate-capped gold nanoparticles, with homocysteine acting as the incoming ligand and glutathione as the moderator. The kinetics of the nucleation and growth driven ligand-exchange is characterized by a sigmoidal switching function and differs from that of the usually observed Langmuirian pseudo-first-order process corresponding to the random place-exchange. The ultra-fast functionalization process was monitored using resonance elastic light scattering (RELS) spectroscopy and confirmed by UV–vis plasmonic band absorbance measurements.

© 2010 Elsevier B.V. All rights reserved.

## 1. Introduction

Growing interests in bioassays providing transduction of bioinformation to optical and electronic signals have recently been observed in conjunction with stimulating developments in synthesis of highly efficient quantum-dots and functionalized gold nanoparticles (AuNP) [1–3]. The vast potential of AuNP in nanomedicine and bioassays stems from the immense possibilities of designing complex nanoarchitectures with precision recognition of DNA fragments [4–8]. In biosensors and sensor arrays which have been modified by immobilizing multifunctional AuNP in sensory films, an enhanced response has been observed in a variety of sensors [8–11]. The enhancement is likely to be associated with surface plasmon coupling, increased surface area, improved flexibility of embedded biorecognition elements, and other effects. Various functionalization methods for AuNP based on self-assembly of protective monolayers, such as the multi-functional thiols [1,2,12–16], DNA [3,17], and other biorecognition layers [15,18,19], have been utilized. Kinetic studies show that the ligand-exchange process in a self-assembled monolayer (SAM) film is basically a Langmuirian pseudo-first-order process [2,20–22] and as such, is based on the random place-exchange proceeding evenly on the entire surface of AuNP. Additionally, this process may be influenced by such slow steps as surface diffusion [19], hydrogen bond breaking [22], or

slow desorption [23]. Generally, low concentrations of the incoming ligands have been used in AuNP functionalization processes, on a presumption of better film ordering. However, film ordering itself is an inherently slow process due to the very slow surface diffusion which is then the slowest step in the film preparation, taking in some cases up to 100 h [22,24]. The improvement of the rate of metal nanoparticle functionalization is then highly desired.

In our previous studies, we have focused on designing and testing piezosensors based on glutathione (GSH) films (QC/Au/GSH and derivatives) for the detection of heavy metals (Hg(II), Pb(II), Cd(II)) and other metal ions (Ni(II), Cu(II), lanthanides) [25–29]. The fundamental problems of the fabrication of GSH films, as well as other thiol-based films, and their functionalization have been the subject of extensive studies by other groups as well and still the mechanism and kinetics of the sensory film formation are not well understood [30,31]. Such issues as to whether the mixed thiol films are homogeneous [32] or segregated multi-phase systems [33,34] are being actively investigated in view of the importance the form and composition of sensory films have for the functionality and performance of the sensors. In this work, we have described phenomena which are the key factors in sensory film fabrication. These phenomena relate to the speed of the film formation and modification of the film composition. Since the utilization of gold nanoparticles for the enhancement of sensor performance has recently been demonstrated [8–11], the assembly of gold nanoparticles to form organomolecule-linked networks is also of interest for the sensor developers, not only as a means of monitoring the ligand-exchange processes in nanoparticle shells, but also for the

---

* Corresponding author. Tel.: +1 315 267 2267; fax: +1 315 267 3170.
*E-mail address:* hepelmr@potsdam.edu (M. Hepel).
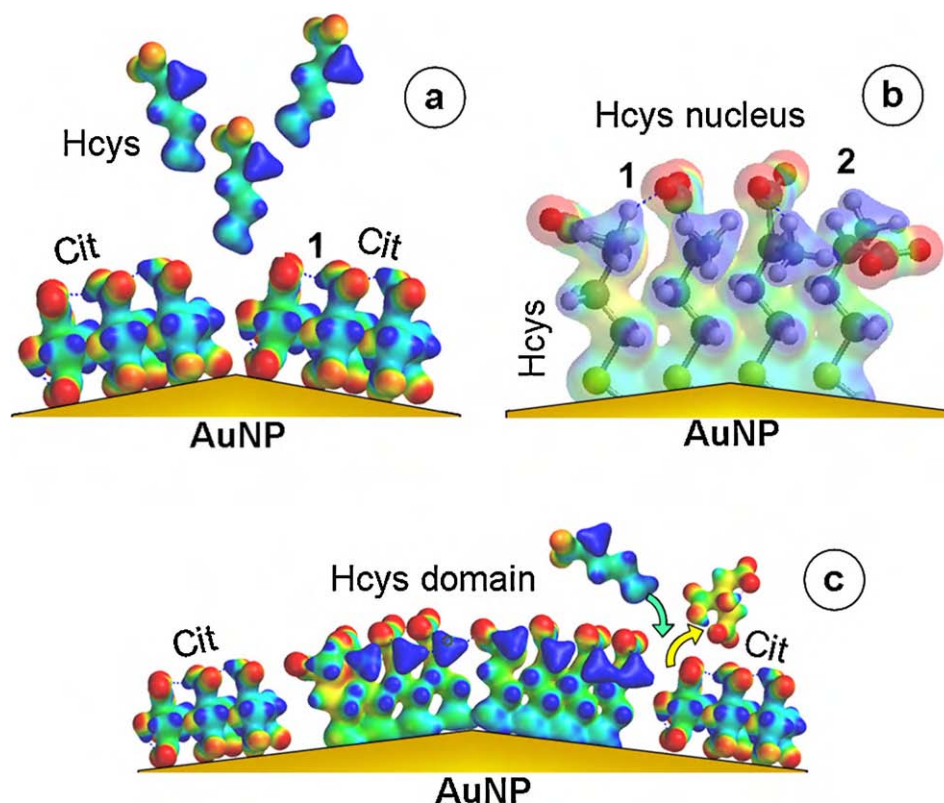
**Fig. 1.** Schematic view of the hydrogen bonded citrate SAM basal film (a) and the nucleation and growth of a hydrogen bonded Hcys-ligand domain (c) on an edge of a citrate-capped AuNP (b).

preparation of AuNP networked films. Thus, the practical aspects of the phenomena described in this paper are associated with the sensor development and film fabrication.

Herein, we describe a new nanoparticle functionalization methodology based on employing high-concentration moderator ligands controlling a fast one-step ligand-exchange operation. In the experiments reported below, a short time frame, $\tau = 60$ s, was arbitrarily selected. The fine-tuning of the film composition was achieved by utilizing moderator molecules able to control the interfacial ligand-exchange process. Since the ligand-exchange process on Au terraces is very slow then to attain high exchange rates, we have based our approach on the sequential process commencing from nanocrystal edges [35]. The nucleation of ligand-exchange domains at the core edges and their 2D growth, corresponding to this approach, are illustrated in Fig. 1.

A clear break in the film-protecting hydrogen-bonds in a citrate SAM at the nanocrystal edge is seen in drawing (b). In the experimental example of the proposed methodology presented in this paper, we have employed a biomolecule, homocysteine (Hcys), as the ligand replacing citrate capping of AuNP$_{5\,nm}$ (see Fig. 1) and glutathione (GSH) which can act as the moderator for ligand-exchange processes. For the fast detection of ligand-exchange processes, we have employed the resonance elastic light scattering (RELS) spectroscopy [36–39]. The RELS spectroscopy has been proposed for analytical determination of complexes and biocompounds [36–39] and offers also an exceptional sensitivity to the degree of AuNP assembly [14].

## 2. Materials and methods

### 2.1. Chemicals

All chemicals used for investigations were of analytical grade purity. L-Glutathione reduced, minimum 99% (GSH),

DL-Homocysteine (HS(CH$_2$)$_3$NH$_2$COOH), tetrachloroauric(III) acid trihydrate (HAuCl$_4$·3H$_2$O), 99.9 + % metals basis, were purchased from Sigma–Aldrich Chemical Company (Atlanta, GA, USA) and used as received. Sodium citrate, dihydrate (HOC(COONa)(CH$_2$COONa)$_2$·2H$_2$O) was obtained from J.T. Baker Chemical Co. (Phillipsburg, NJ, USA). Sodium borohydride (NaBH$_4$) and other reagents were obtained from Fisher Scientific Company (Pittsburgh, PA, USA). Solutions were prepared using Millipore (Billerica, MA, USA) Milli-Q deionized water (conductivity $\sigma = 55$ nS/cm). They were deoxygenated by bubbling with purified argon.

### 2.2. Apparatus

The imaging analyses of Au nanoparticles were performed using high-resolution transmission electron microscopy (HR-TEM) with Model JEM-2010 (Jeol, West Chester, PA, USA) instrument with accelerating voltage of 200 kV. The resonance elastic light scattering (RELS) spectra were recorded using LS55 Spectrometer (Perkin Elmer, Waltham, MA, USA) equipped with 20 kW xenon light source operating in 8 µs pulsing mode allowing for the use of monochromatic radiation with wavelength from 200 to 800 nm with 1 nm resolution and sharp cut-off filters: 290, 350, 390, 430, 515 nm. The dual detector system consisted of a photomultiplier tube (PMT) and an avalanche photodiode. Pulse width at half height was less than 10 µs. For the instrument to record scattering spectra for the resonance elastic light scattering (RELS) spectroscopy, the sample was illuminated with a monochromatic beam of light and the scattered light was detected at 90° angle. The wavelength scanning was set to $\Delta\lambda = 0$ (i.e. simultaneous scan of the excitation and detection monochromators). The constant-excitation spectra were recorded by setting $\lambda_{ex} = $ const and scanning $\lambda_{em}$ (emission wavelength) around $\lambda_{ex}$. Other details of RELS technique can be found
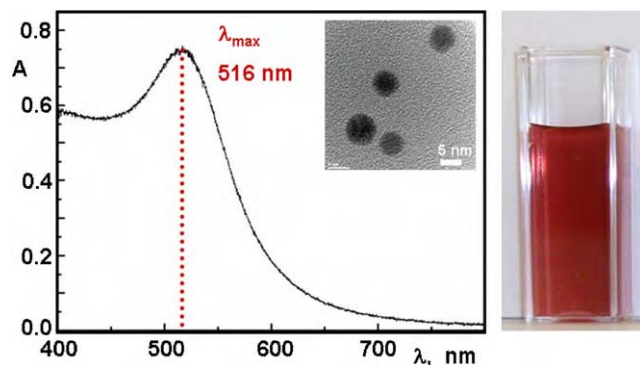
**Fig. 2.** Characterization of citrate-capped AuNP: the SP absorbance spectrum with $\lambda_{max} = 516$ nm and photo of the cuvette showing ruby-red color of AuNP solution; inset: high-resolution TEM image of nanoparticles (bar length: 5 nm). (For interpretation of the references to color in this figure legend, the reader is referred to the web version of the article.)

in our recent publication [14]. The RELS technique is suitable for studying ligand-exchange processes followed by AuNP assembly which provide a high amplification of the RELS signal. The UV–vis spectra were recorded using Perkin Elmer Lambda 50 Spectrophotometer in the range of 220–1100 nm or Ocean Optics (Dunedin, FL, USA) Model R4000 Precision Spectrometer in the range from 340 to 900 nm.

### 2.3. Procedures

The Au nanoparticles were synthesized according to the published procedure [14,40,41]. Briefly, to obtain 5 nm AuNP, a solution of $HAuCl_4$ (10 mM, 2.56 mL) was mixed with a trisodium citrate solution (10 mM, 9.6 mL), ratio 1: 3.75, and poured to distilled water (88 mL). The obtained solution was vigorously stirred and fresh cold $NaBH_4$ solution (5 mM, 8.9 mL) was added dropwise. The solution slowly turned light grey and then ruby red. Stirring was maintained for 30 min. The obtained citrate-capped core-shell Au nanoparticles (AuNP) were stored at 4 °C. Their size, determined by HR-TEM imaging and UV–vis surface plasmon absorption was $5.0 \pm 0.9$ nm ($n = 85$); no larger particle population was present. The concentrations of AuNPs are given in moles of particles per 1 L of solution (usually, in the nM range). The size and distribution of AuNP were also tested using plasmonic absorbance spectra in UV–vis. A clear surface plasmon band with $\lambda_{max} = 516$ nm and a low background beyond that wavelength indicate that no larger particles were present. The UV–vis spectrum of the plasmonic band, TEM high-resolution image, and color photograph of the AuNP solution is presented in Fig. 2. The homocysteine and glutathione stock solutions in water (10 mM) were stored at 4 °C. The solutions were prepared fresh just before the experiments, with citrate buffer, pH = 5, $C_{Cit} = 0.46$ mM (final concentration). A separate solution was prepared for each measurement. The pH of AuNP solution and that of Hcys and GSH solutions was checked before mixing and also at the end of experiment. The interactions of Hcys and GSH with AuNP were monitored using RELS spectroscopy and UV–vis surface plasmon spectroscopy.

Molecular dynamics (MD) and quantum mechanical (QM) calculations of electronic structures of Hcys and GSH and their interactions were performed using modified Hartree–Fock methods [42,43] with 6-31 G* basis set and pseudopotentials, as well as the density functional theory (DFT) with B3LYP functional and strongly correlated advanced Moller–Plesset method, embedded in Wavefunction Spartan 6 [43]. The electron density and local density of states (LDOS) are expressed in atomic units, au$^{-3}$, where 1 au = 0.52916 Å and 1 au$^{-3}$ = 6.7491 Å$^{-3}$.
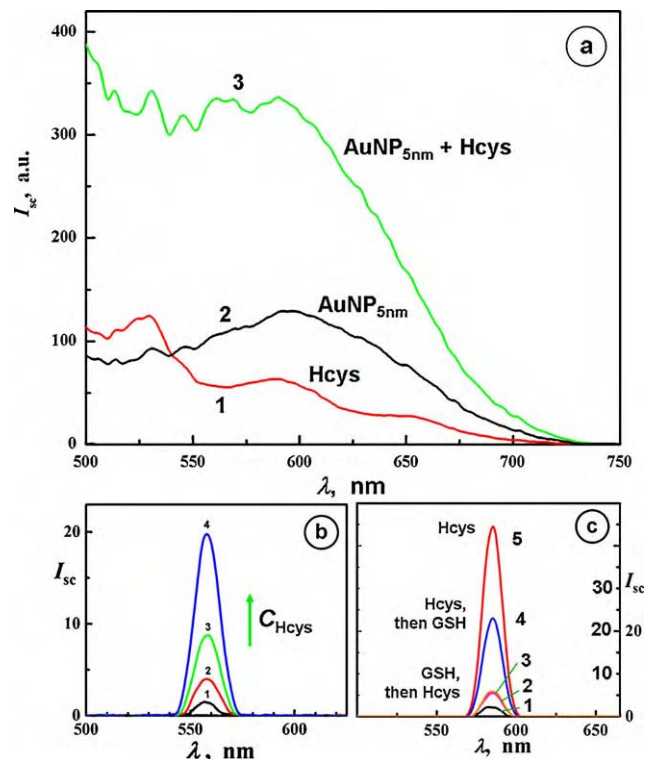


**Fig. 3.** (a) RELS spectra for: (1) 20 µM Hcys, (2) 3.8 nM AuNP$_{5\,nm}$ and (3) 3.8 nM AuNP$_{5\,nm}$ + 20 µM Hcys recorded after 60 s reaction time; (b) RELS spectra at constant $\lambda_{ex} = 560$ nm for 3.8 nM AuNP$_{5\,nm}$ + $x$ Hcys after 60 s reaction time, $x$ [µM]: (1) 0, (2) 5, (3) 5.5, (4) 5.75; (c) illustration of the inhibition of nucleation of Hcys-domains in a shell of citrate-capped AuNP$_{5\,nm}$ by the addition of GSH during 60 s AuNP functionalization: (1) GSH alone, (2) AuNP alone, (3) GSH mixed with AuNP and then added Hcys, (4) Hcys mixed with AuNP and then added GSH, (5) AuNP + Hcys (without GSH); citrate buffer, $C_{Cit} = 0.46$ mM, pH = 5; $\tau = 60$ s (all concentrations are final concentrations).

## 3. Results and discussion

### 3.1. RELS spectroscopic monitoring of ligand-exchange and AuNP assembly

The measurements were carried out at a predefined wavelength selected from the RELS spectra for AuNP@Hcys (Fig. 3a). Well resolved RELS spectra were obtained for excitation wavelengths in the range: $\lambda_{ex} = 560$–640 nm (Fig. 3b and c). The increase of scattering intensity is due to the dependence of scattering cross-section on particle diameter $a$ and the dielectric function (or refractive index) of the medium:

$$I_{sc} = I_0 N \frac{1 + \cos^2 \theta}{2R^2} \left(\frac{2\pi}{\lambda}\right)^4 \frac{(n_p - n_s)^2 - 1}{(n_p - n_s)^2 + 2} \left(\frac{a}{2}\right)^6 \quad (1)$$

where $n_p$ and $n_s$ are the refractive indices for the particles and the solution, respectively, $\lambda$ is the wavelength of incident light beam, $R$ is the distance from source, $\theta$ is the scattering angle, $N$ is the number of particles, and $I_0$ is the constant.

We note that the scattering maximum in Fig. 3a appears at longer wavelengths than the absorbance maximum. For perfectly monodisperse, non-interacting particles, the maximum of absorbance and scattering should be close if the efficiency of the secondary emission (or reflectivity) is not dependent on wavelength. Since the plasma frequency, determined by the frequency of the absorbance maximum, is the highest frequency with which free electrons can follow the electromagnetic field oscillations, the AuNP behave as a non-metal at frequencies higher than plasma frequency and as a perfect metal at frequencies lower than plasma
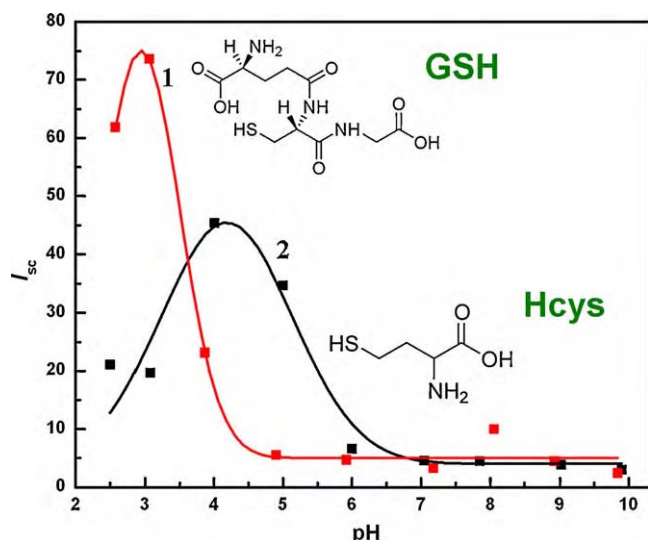
**Fig. 4.** Dependence of $I_{sc}$ on pH for: (1) 20 μM GSH solutions and (2) 20 μM Hcys solutions; $\tau$ = 60 s; $C_{AuNP}$ = 3.8 nM; AuNP diameter: 5 nm, $C_{Cit}$ = 0.46 mM.

frequency. The maximum of the light reflection will then be shifted toward wavelengths longer than the Frohlich wavelength $\lambda_F$ where free electrons reflect light with high efficiency (here, $\lambda_F$ approximately equals to $\lambda_{max}$ of plasmon absorbance). In other words, high scattering intensity is observed when both the absorbance and secondary emission are high. The RELS maximum can also be shifted to longer wavelengths if in equilibrium with majority of single gold nanoparticles there would be a small number of AuNP aggregates. However, this should not be of significance since the absorbance spectra recorded in the absence of thiols show a very narrow SP band with no long-wave tail present (*cf.* Fig. 2).

To distinguish between Hcys-dominated AuNP and GSH-dominated AuNP, the pH dependence of RELS was analyzed (Fig. 4). By carefully selecting pH, it is possible to keep Hcys in the form of zwitterions, which leads to the AuNP assembly [14,44]. In solution at pH = 5, we have predominantly zwitterionic Hcys and negatively charged GSH. The p$K_a$ values for Hcys are: p$K_1$ = 2.22 (–COOH), p$K_2$ = 8.87 (–NH$_2$) and p$K_3$ = 10.86 (–SH) making it a zwitterions at pH = 5. At the same pH, GSH is negatively charged (p$K_a$ values for GSH are: p$K_1$ = 2.04 (glutamate –COOH), p$K_2$ = 3.4 (glycine –COOH), p$K_3$ = 8.72 (–SH group), p$K_4$ = 9.49 (–NH$_2$ group)). (Note that the scattering decrease for Hcys at pH > 6.5 (Fig. 4) indicates on a shift of the p$K_a$ value for protonation of –NH$_2$ group in adsorbed Hcys. Similar shifts in surface p$K_a$ are not unusual and have been observed for other ligands as well [31,45–52]. Therefore, a high RELS intensity can be ascribed to the Hcys-dominated AuNP shells (due to Hcys-induced aggregation of AuNPs) and low RELS intensity to the GSH-dominated AuNP shells (due to repulsions between AuNPs).

The RELS signal is extremely sensitive to the aggregation. Recently, we have derived the size dependence of scattering intensity for the aggregation process [14] showing that $I_{sc}$ increases with third power of aggregate diameter:

$$\frac{I_{sc,2}}{I_{sc,1}} = a_{rel}^3 \qquad (2)$$

where $I_{sc,1}$ and $I_{sc,2}$ are the scattering intensities before aggregation (1) and after aggregation (2) leading to the formation of aggregates with relative particle-size increase $a_{rel} = a_2/a_1$ where $a_1$ and $a_2$ are the diameters of the particle before and after aggregation, respectively. While a rigorous physical treatment is not available, there are two indications that a red-shift should be observed in the case of AuNP assembly: (i) first of all, for larger solid particles, a red shift follows from theoretical calculations [53–55] and from experimen-
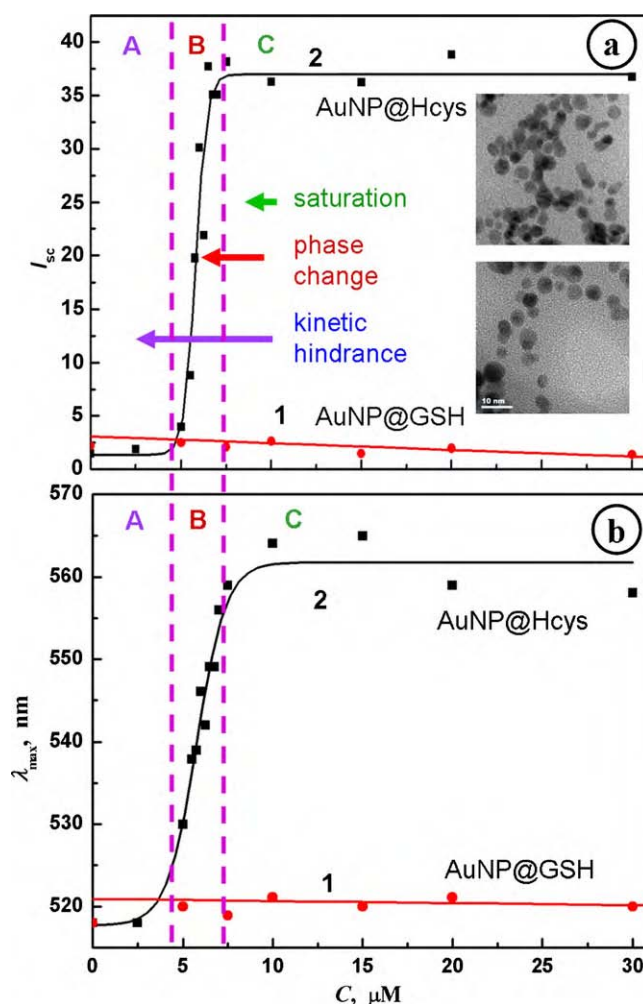


**Fig. 5.** (a) Dependence of RELS intensity $I_{sc}$ for citrate-capped AuNP$_{5\,nm}$ on incoming ligand concentration $C$ for: (1) GSH, (2) Hcys; (b) control experiment showing the dependence of $\lambda_{max}$ for plasmonic absorbance band shift on ligand concentration $C$; $C_{AuNP}$ = 3.8 nM, citrate buffer, $C_{Cit}$ = 0.46 mM, pH = 5, $\lambda_{ex}$ = 560 nm; $\tau$ = 60 s; inset: TEM images for (1) and (2), scale bar: 10 nm; all concentrations are final concentrations; curves (2) are fitted with sigmoidal Boltzmann function, $R$: (a) 0.98, (b) 0.97.

tal observations [56–60]; (ii) when two AuNP particles are at close distance (distance $d < 5r$, where $r$ is the nanoparticle radius), the surface plasmons of the two particles interact with each other and begin to oscillate in resonance and the frequency of these oscillations should be lower similar to frequency lowering effect with the resonator size (e.g for longitudinal SP resonators in nanorods with increasing length of the rod).

The dependence of RELS intensity on concentration of the incoming ligand, $C$, is presented in Fig. 5a. It becomes immediately apparent that the shape of the $I_{sc}$–$C_{Hcys}$ relationship (curve 2) is a threshold-type characteristics which is modeled using the Boltzmann function of the form:

$$I_{sc} = \frac{I_{max,1} - I_{max,2}}{1 + \exp\{(C - C_{1/2})/S\}} + I_{max,2} \qquad (3)$$

with the following parameters: the low-concentration scattering intensity $I_{max,1}$ = 1.35 ± 2.18, the high-concentration scattering intensity $I_{max,2}$ = 36.99 ± 1.42, the half-way threshold concentration of the ligand $C_{1/2}$ = 5.78 ± 0.09, and the slope parameter $S$ = 0.312 ± 0.082. The switching begins at $C_{Hcys}$ = 4 μM and ends at $C_{Hcys}$ = 6 μM with a sharp transition from the background scattering level of AuNP@Cit to that characteristic of the AuNP@Hcys. The observed characteristic indicates that none of the monophasic
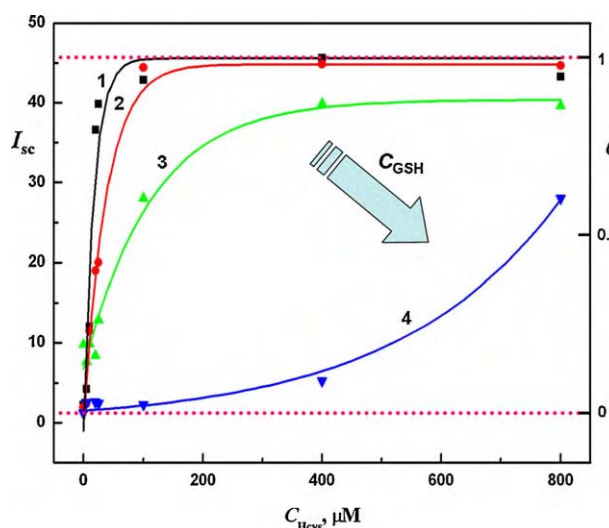
**Fig. 6.** Tuning the speed of ligand-exchange and SAM shell composition in fast AuNP functionalization; dependence of RELS intensity $I_{sc}$ on $C_{Hcys}$ for different $C_{GSH}$ [μM]: (1) 5, (2) 20, (3) 100, (4) 400; $C_{AuNP}$ = 3.8 nM, citrate buffer, $C_{Cit}$ = 0.46 mM, pH = 5, $\lambda_{ex}$ = 640 nm, $\tau$ = 60 s; all curves are fitted with sigmoidal Boltzmann function.

models of random ligand-exchange [61] can satisfactorily describe our system behavior since none of these models is compatible with the threshold-type of a transition. Moreover, it has recently been shown that the rate of aggregation induced by the random ligand-exchange is of a pseudo-first order w.r.t. the incoming ligand [21]. Since the sharpness of the transition is reminiscent of an avalanche process that is initiated by the nucleation and growth of a new phase, we attribute this transition to the ligand-exchange process proceeding via the nucleation and growth of 2D domains. The independent control experiments performed by monitoring plasmonic absorbance band shifts (Fig. 5b) confirm the fast switching behavior of the ligand-exchange and AuNP assembly. The experimental data were fitted with Boltzmann function:

$$\lambda_{max} = \frac{\lambda_{max,1} - \lambda_{max,2}}{1 + \exp\{(C - C_{1/2})/S\}} + \lambda_{max,2} \tag{4}$$

with the following parameters: the low-concentration $\lambda_{max}$ limit $\lambda_{max,1}$ = 517.7 ± 2.1, the high-concentration $\lambda_{max}$ limit $\lambda_{max,2}$ = 561.8 ± 1.4, the half-way threshold concentration of the ligand $C_{1/2}$ = 5.755 ± 0.138, and the slope parameter $S$ = 0.821 ± 0.133; the regression coefficient was $R$ = 0.974 and $x^2$ = 7.60.

The sigmoidal kinetic plots presented here are consistent with the model of 2D-nucleation and growth of incoming-ligand domains [35]. In this model, exchanges occur at the circumference of the growing domain and the rate of exchange first increases, as the domain grows, and after taking up a half-sphere, decreases with further domain growth. This results in the sigmoidal characteristics of $I_{sc}$ vs. $C$.

### 3.2. Composition control of SAM films

To control the SAM composition in the fast ligand-exchange process, GSH-moderator molecules able to influence the nucleation and growth processes in the short time-scale of the functionalization process have been used. A series of experiments has been performed in which the concentration ratios $C_{GSH}/C_{Hcys}$ were changed in a wide range from 0.002 to 160. In Fig. 6, the RELS intensity for 3.8 nM AuNP$_{5\,nm}$ solutions is plotted vs. $C_{Hcys}$ for different concentration levels of GSH. The average composition of the film is

approximately given by:

$$\theta = \frac{I - I_{min}}{I_{max} - I_{min}} \tag{5}$$

where $\theta$ is the content of the linker ligand (Hcys) in the SAM shell and $I_{min}$, $I_{max}$ are the minimum and maximum scattering intensities corresponding to AuNP@GSH and AuNP@Hcys, respectively. This dependence enables a quick estimate of the average film composition.

The ability to control the SAM composition in the fast ligand-exchange process is the key element to the nanoparticle functionalization. The mechanism of action of the moderator molecules is not well understood but it likely involves the competition for the nucleation sites and/or tuning the exchange processes at ligand-exchange wave-front, i.e. at the perimeter of the growing domains of the incoming ligand.

The changes in film composition, discussed above, are useful in several approaches in sensory film fabrication, such as in the process of: (i) embedding two, or more, different functionalities, (ii) introducing spacers for the attachment of large bioorganic molecules (e.g. streptavidin [17]), (iii) controlling the range of sensor response (e.g. in GSH-capped QC/Au-piezosensors for Hg(II), the film response can be tuned to higher or lower Hg(II) concentration range [25,27] by controlling the sensory film properties, such as the film density, leading to the changes in film permeability). On the other hand, no morphological changes in nanoparticle cores are encountered unless the system is heated to higher temperatures, which would result in AuNP core enlargement.

In general, the aggregation of AuNP may not necessarily be due to the ligand-exchange but may also be caused by other factors as well, such as the addition of higher salt concentrations (on account of considerable decrease of Debye layer thickness at the outer nanoparticle film interface [60] or simply by reducing AuNP solubility in the salting-out effect) or injection of small amounts of multivalent metal cations able to coordinate to the ligands of nanoparticle shells [62] in which case metal cations act as the linkers. However, neither the salt or metal cations have any chance to replace a SAM film that protects AuNP. In contrast to that, the high affinity of thiols to a Au surface [30] changes the situation dramatically and enables such thiols as GSH and homocysteine to readily replace citrates from the nanoparticle shell [14,58,60]. While GSH can form intermittently some weakly bound intermediate interparticle linking structures [35], these only help to isolate a citrate ion from its neighbors and remove that citrate from the film.

### 3.3. Molecular dynamics and quantum mechanical calculations

A comparison of the size and electronic structure of molecules taking part in ligand-exchange processes at AuNP are presented in Fig. 7. It is seen that Hcys and GSH molecules are taller than Cit. Hcys appears to be smoother than GSH and should show less steric hindrance than GSH while forming 2D domains. The experimental data confirm this conjecture. The MD simulation of intermolecular binding for a group of homocysteine (Hcys) molecules as a model of Hcys domain in SAM-shell on a gold nanoparticle (AuNP) were carried out to evaluate intermolecular hydrogen bonding in that group and to support the mechanism of predominant interactions of Hcys with other Hcys molecules rather than with existing citrate ligands in SAM on AuNP. The calculations were performed by collecting a group of four Hcys molecules in a zwitterionic form (protonated –NH$_3^+$ and dissociated –COO$^-$ groups). The molecules were moved close to each other and allowed to relax and form inter- and intra-molecular H-bonds. The zwitterionic structure of Hcys enabled the formation of H-bonds between each neighbor molecule thus strengthening the group. The results of QM calculations of electronic structure are presented in Fig. 8. The electron
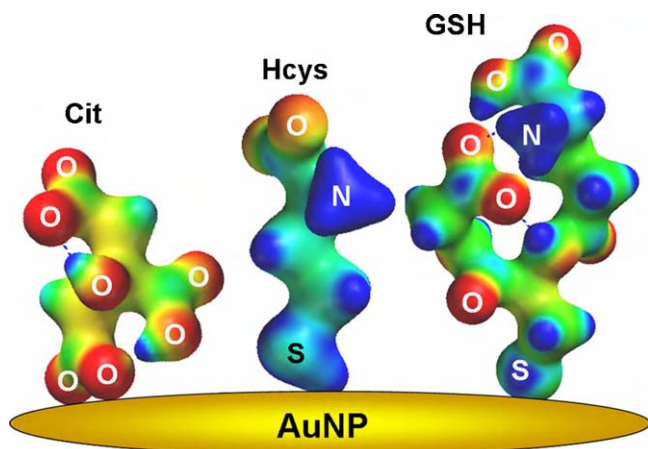
**Fig. 7.** Comparison of molecule size and electron density surfaces for citrate, homocysteine, and glutathione taking part in ligand-exchange processes at a AuNP; the electrostatic potential is mapped on the density surface (color code: from negative potential – red, to positive potential – blue). (For interpretation of the references to color in this figure legend, the reader is referred to the web version of the article.)
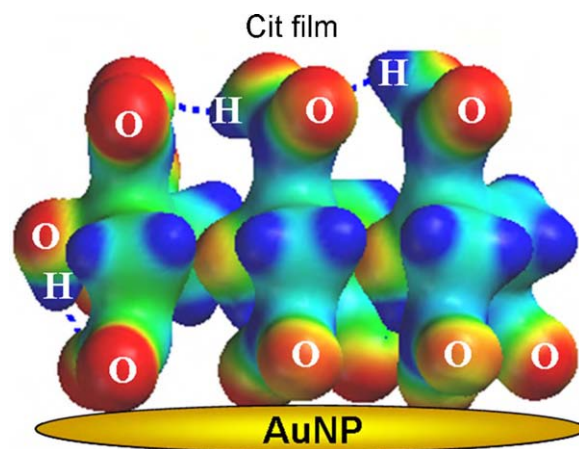
density surface is mapped with electrostatic potential (color coded: from negative potential (red) to positive (blue)).

It is seen that on the outer surface some disorder of functional groups ($-COO^-$ and $-NH_3^+$) is apparent. This is due to the conformational adjustments of Hcys molecules to adapt to the H-bonding geometry. The intermolecular forces make the group seen as a single cluster of molecules. Such groups of a few Hcys molecules can be treated as nuclei of the ligand-exchange domain. The nuclei grow on the outside borders where bonding between Hcys molecules and citrate ligands of the existing SAM on AuNP is weak. Eventually, the fast growing domains take over the entire surface of a nanoparticle. The surface diffusion of ligands does not play any role because of the time limitation of process, which was restricted to 60 s in this work.

Similar calculations have also been performed for a group of citrate molecules, as illustrated in Fig. 9. Again, intermolecular H-bonding strengthens the citrate SAM and makes it less penetrable to foreign species, e.g. Hcys ligands. This corroborates the assumption that most likely nucleation sites for the ligand-exchange domains are located where the film has discontinuities, i.e. at the edges and plane steps, in agreement with Murray's model [2].
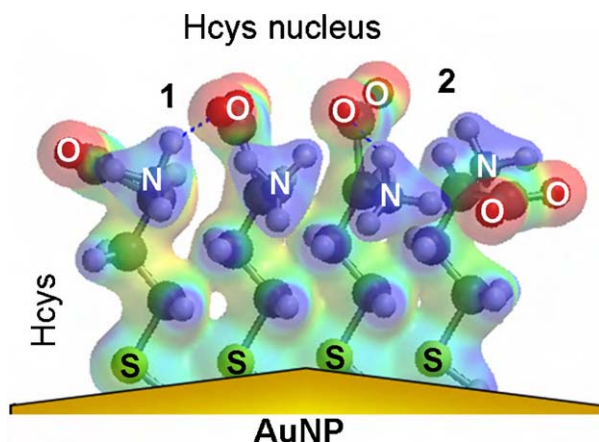


**Fig. 8.** Electron density surface for a group of homocysteine molecules forming a nucleus of the ligand-exchange domain at an edge of a AuNP; the electrostatic potential is mapped on the density surface (color code: from negative potential – red, to positive potential – blue); 1 – inter-molecular hydrogen bond, 2 – intra-molecular hydrogen bond.(For interpretation of the references to color in this figure legend, the reader is referred to the web version of the article.)



**Fig. 9.** Electron density surface for a group of citrate molecules of a SAM shell on a AuNP; the electrostatic potential is mapped on the density surface (color code: from negative potential – red, to positive potential – blue); the group is inter-molecularly hydrogen bonded; hydrogen bonds are marked with dashed lines. (For interpretation of the references to color in this figure legend, the reader is referred to the web version of the article.)

Since the forces and phenomena playing important roles in the behavior of SAM films on AuNP are complex, their comprehensive evaluation would require carrying out calculations taking into account highly populated adsorption films, together with the nanocrystalline-structured substrate (Au core), and the diffuse double-layer on the solution side. Such calculations have not been done so far for any system. Therefore, at this stage, our MD simulations and QM calculations have focused on smaller, more primitive models to evaluate some limited effects, rather than solve the entire SAM film problems. Since for the analysis of ligand-exchanges it is important to verify if the intermolecular H-bonding within the SAM film occurs or not, we have carried out calculations for small groups of citrate and homocysteine molecules emulating a portion of the SAM films. The results indicate clearly that H-bonding stabilizes both the citrate SAMs and the homocysteine SAMs. As concerns to the ligand $pK_a$ in solution and $pK_a$ shifts in a SAM film, the calculations were carried out for the predetermined ionic/neutral species and thus reflected a fixed solution pH for which these pre-set ligand forms predominate. In this way, the results obtained are invariant with the $pK_a$-modifying forces and correspond to the well-defined film composition and the charge state. (In other words, if these would not have been pre-set, then the $pK_a$-modifying forces, including the interactions of ligand molecules in the SAM with gold substrate and with the solution phase would have to be taken into account.)

The results of MD and QM calculations provide visualization of the strengthening of pure ligand 2D phases by hydrogen bonding and enable better understanding of the reduced steric hindrance at the nanocrystal edge which is essential in identifying the likely nucleation sites for the incoming ligand domain formation. The H-bonding and over-driven irreversible conditions are likely prerequisites of the nucleation and growth mechanism of the ligand-exchange observed in this work.

## 4. Conclusion

In summary, we have demonstrated the viability of a fast (on the order of 60 s) nanoparticle functionalization process with moderator-tunable composition of the monolayer-shell. This process is based on a new paradigm of the ligand-exchange proceeding through the nucleation and growth of 2D ligand domains and may be utilized as an efficient preparation step in nanoparticle-enhanced sensory film designs for biosensors and

other applications, such as the multifunctional nanoparticles for MRI image enhancement, photodynamic cancer therapy, colorimetric assays for heavy metals and others.

## Acknowledgements

## References

[1] C.D. Bain, J. Evall, G.M. Whitesides, Formation of monolayers by the coadsorption of thiols on gold: variation in the head group, tail group, and solvent, J. Am. Chem. Soc. 111 (1989) 7155–7164.
[2] M.J. Hostetler, A.C. Templeton, R.W. Murray, Dynamics of place-exchange reactions on monolayer-protected gold cluster molecules, Langmuir 15 (1999) 3782–3789.
[3] L.M. Demers, C.A. Mirkin, R.C. Mucic, R.A. Reynolds, R.L. Letsinger, R. Elghanian, G. Viswanadham, A fluorescence-based method for determining the surface coverage and hybridization efficiency of thiol-capped oligonucleotides bound to gold thin films and nanoparticles, Anal. Chem. 72 (2000) 5535–5541.
[4] L. Wang, X. Liu, X. Hu, S. Song, C. Fan, Unmodified gold nanoparticles as a colorimetric probe for potassium DNA aptamers, Chem. Commun. (2006) 3780–3782.
[5] H. Li, L. Rothberg, Colorimetric detection of DNA sequences based on electrostatic interactions with unmodified gold nanoparticles, Proc. Natl. Acad. Sci. 101 (39) (2004) 14036–14039.
[6] R. Elghanian, J.J. Storhoff, R.C. Mucic, R.L. Letsinger, C.A. Mirkin, Selective colorimetric detection of polynucleotides based on the distance-dependent optical properties of gold nanoparticles, Science 277 (1997) 1078–1081.
[7] A.P. Alivisatos, K.P. Johnsson, X. Peng, T.E. Wilson, C.J. Loweth, M.P. Bruchez, P.G. Schultz, Attachment of oligonucleotides to thiol-coated AuNP, Nature 382 (1996) 610.
[8] S.J. Park, T.A. Taton, C.A. Mirkin, Array-based electrical detection of DNA with nanoparticle probes, Science 295 (2002) 1503–1505.
[9] C.Y. Tsai, Y.H. Tsai, C.C. Pun, B. Chan, T.Y. Luh, C.C. Chen, F.H. Ko, P.J. Chen, P.H. Chen, Electrical detection of DNA hybridization with multilayer gold nanoparticles between nanogap electrodes, Microsyst. Technol. 11 (2005) 91–96.
[10] T.A. Taton, G. Lu, C.A. Mirkin, Two-color labeling of oligonucleotide arrays via size-selective scattering of nanoparticle probes, J. Am. Chem. Soc. 123 (2001) 5164–5165.
[11] M. Hepel, M. Stobiecka, Interactions of Herbicide Atrazine with DNA, Nova Science Publishers, New York, 2010.
[12] C.E.D. Chidsey, Electron transfer rate depends on thiol chain length, Science 25 (4996) (1991) 919–922.
[13] R.G. Nuzzo, D.L. Allara, Adsorption of bifunctional organic disulfides on gold surfaces, J. Am. Chem. Soc. 105 (1983) 4481.
[14] M. Stobiecka, J. Deeb, M. Hepel, Ligand-exchange effects in gold nanoparticle assembly induced by oxidative stress biomarkers: Homocysteine and cysteine, Biophys. Chem. 146 (2010) 98–107.
[15] M. Stobiecka, J. Deeb, M. Hepel, Molecularly-templated polymer matrix films for biorecognition processes: sensors for evaluating oxidative stress and redox buffering capacity, Electrochem. Soc. Trans. 19 (28) (2009) 15–32.
[16] R. Colorado, R.J. Villazana, T.R. Lee, Self-assembled monolayers on gold generated from aliphatic dithiocarboxylic acids, Langmuir 14 (1998) 6337–6340.
[17] A.M. Nowicka, A. Kowalczyk, Z. Stojek, M. Hepel, Nanogravimetric and voltammetric DNA-hybridization biosensors for studies of DNA damage by common toxicants and pollutants, Biophys. Chem. 146 (2010) 42–53.
[18] A.K. Boal, V.M. Rotello, Fabrication and self-optimization of multivalent receptors on nanoparticle scaffolds, J. Am. Chem. Soc. 122 (2000) 734–735.
[19] M.H.V. Werts, H. Zaim, M. Blanchard-Desce, Excimer probe of the binding of alkyl disulfides to gold nanoparticles and subsequent monolayer dynamics, Photochem. Photobiol. Sci. 3 (2004) 29–32.
[20] J.B. Schlenoff, M. Li, H. Ly, Stability and self-exchange in alkanethiol monolayers, J. Am. Chem. Soc. 117 (1995) 12528–12536.
[21] I.I.S. Lim, M.M. Maye, J. Luo, C.J. Zhong, Kinetic and thermodynamic assessments of the mediator-templateassemblyof nanoparticles, J. Phys. Chem. B 109 (2005) 2578–2583.
[22] J.C. Love, L.A. Estroff, J.K. Kriebel, R.G. Nuzzo, G.M. Whitesides, Self-assembled monolayers of thiolates on metals as a form of nanotechnology, Chem. Rev. 105 (2005) 1103–1169.
[23] M. Montalti, L. Prodi, N. Zaccheroni, R. Baxter, G. Teobaldi, F. Zerbetto, Kinetics of place-exchange reactions of thiols on gold nanoparticles, Langmuir 19 (2003) 5172–5174.
[24] M.J. Hostetler, A.C. Templeton, R.W. Murray, Dynamics of place-exchange reactions on monolayer-protected gold cluster molecules, Langmuir 15 (1999) 3782.
[25] M. Hepel, J. Dallas, Multifunctional polypeptide EQCN sensors: probing the cysteamine-glutathione film permeability with Hg(II) ions, Sensors 8 (2008) 7224–7240.
[26] M. Hepel, J. Dallas, M.D. Noble, Glutathione modified gold piezoelectric and voltammetric sensors for determination of mercury in a wide concentration range, Sensors Transducers 88 (2008) 47.
[27] M. Hepel, J. Dallas, M.D. Noble, Interactions and reactivity of Hg(II) on glutathione modified gold electrode studied by EQCN technique, J. Electroanal. Chem. 622 (2008) 173–183.
[28] M. Hepel, E. Tewksbury, Ion-gating phenomena of self-assembling glutathione films on gold piezoelectrodes, J. Electroanal. Chem. 552 (2003) 291.
[29] M. Hepel, E. Tewksbury, Nanogravimetric study of templated copper deposition in ion-channels of self-assembled glutathione films on gold piezoelectrodes, Electrochim. Acta 49 (2004) 3827–3840.
[30] G.M. Whitesides, J.K. Kriebel, J.C. Love, Molecular engineering of surfaces using self-assembled monolayers, Sci. Prog. 88 (2005) 17–48.
[31] A.C. Templeton, W.P. Wuelfing, R.W. Murray, Monolayer-protected cluster molecules, Acc. Chem. Res. 33 (2000) 27–36.
[32] A. Kassam, G. Bremner, B. Clark, G. Ulibarri, R.B. Lennox, Place exchange reactions of alkyl thiols on gold nanoparticles, J. Am. Chem. Soc. 128 (2006) 3476–3477.
[33] A.M. Jackson, Y. Hu, P. Silva, F. Stellacci, From homo-ligand to mixed-ligand monolayer protected metal nanoparticles, J. Am. Chem. Soc. 128 (2006) 11135–11149.
[34] A.M. Jackson, J.W. Myerson, F. Stellacci, Spontaneous assembly of sub-nanometre ordered domains in the ligand shell of monolayer protected nanoparticles, Nat. Mater. 3 (2004) 330–336.
[35] M. Stobiecka, K. Coopersmith, M. Hepel, Resonance elastic light scattering (RELS) spectroscopy of fast non-langmuirian ligand-exchange in glutathione-induced gold nanoparticle assembly. J. Colloid Interface Sci. doi:10.1016/j.jcis.2010.06.010.
[36] R.F. Pasternack, C. Bustamante, P.J. Collings, A. Giannetto, E.J. Gibbs, Porphyrin assemblies on DNA as studied by a resonance light-scattering technique, J. Am. Chem. Soc. 115 (1993) 5393–5399.
[37] R.F. Pasternack, Resonance light scattering: a new technique for studying chromophore aggregation, Science 269 (5226) (1995) 935.
[38] Y. Liu, C.Q. Ma, K.A. Li, F.C. Xie, S.Y. Tong, Rayleigh light scattering study on the reaction of nucleic acids and methyl violet, Anal. Biochem. 268 (1999) 187–192.
[39] Z. Jia, J. Yang, X. Wu, C. Sun, S. Liu, F. Wang, Z. Zhao, The sensitive determination of nucleic acids using resonance light scattering quenching method, Spectrochim. Acta A 64 (2006) 555–559.
[40] J. Turkevich, P.C. Stevenson, J. Hiller, synthesis of AuNP, Discuss. Faraday Soc. 11 (1951) 55–75.
[41] M.M. Maye, I.I.S. Lim, J. Luo, Z. Rab, D. Rabinovich, T. Liu, C.J. Zhong, Mediator-template assembly of nanoparticles, J. Am. Chem. Soc. 127 (2005) 1519–1529.
[42] P.W. Atkins, R.S. Friedman, Molecular Quantum Mechanics, Oxford University Press, Oxford, 2004.
[43] W.J. Hehre, L. Radon, P.R. Schleyer, J.A. Pople, Ab-initio Molecular Orbital Theory, Wiley, New York, 1985.
[44] S.I. Lim, C.J. Zhong, Molelucarly mediated processing and assembly of nanoparticles: exploring the interparticle interactions and structures, Acc. Chem. Res. 42 (2009) 798–808.
[45] C.D. Bain, G.M. Whitesides, Surface $pK_a$, Langmuir 5 (1989) 1370.
[46] M.A. Bryant, R.M. Crooks, Determination of surface $pK_a$ values of surface-confined molecules derivatized with pH-sensitive pendant groups, Langmuir 9 (2) (1993) 385–387.
[47] A.T. Masheter, P. Abiman, G.G. Wildgoose, E. Wong, L. Xiao, N.V. Rees, R. Taylor, G.A. Attard, R. Baron, A. Crossley, J.H. Jonesd, R.G. Compton, Investigating the reactive sites and the anomalously large changes in surface $pK_a$ values of chemically modified carbon nanotubes of different morphologies, J. Mater. Chem. 17 (2007) 2616–2626.
[48] M.A. Porter, J.R. Hall, J.C. Locke, J.H. Jensen, P.A. Molina, Hydrogen bonding is the prime determinant of carboxyl $pK_a$ values at the N-termini of -helices Proteins, Struct. Funct. Bioinform. 63 (3) (2006) 621–635.
[49] R.K. Shervedani, M. Bagherzadeh, Electrochemical characterization of in situ functionalized gold cysteamine self-assembled monolayer with 4-formylphenylboronic acid for detection of dopamine, Electroanalysis 20 (5) (2008) 550–557.
[50] J.F. Smalley, K. Chalfant, S.W. Feldberg, T.M. Nahir, E.F. Bowden, An indirect laser-induced temperature jump determination of the surface $pK_a$ of 11-mercaptoundecanoic acid monolayers self-assembled on gold, J. Phys. Chem. B 103 (10) (1999) 1676–1685.
[51] C.J. Zhong, M.D. Porter, J. Am. Chem. Soc. 116 (1994) 11616.
[52] J. Luo, N. Kariuki, L. Han, M.M. Maye, L.W. Moussa, S.R. Kowaleski, C.J. Zhong, Interfacial mass flux at 11-mercaptoundecanoic acid linked nanoparticle assembly on electrodes, J. Phys. Chem. B 106 (2002) 9313–9321.
[53] S. Link, M.A. El-Sayed, Spectral properties and relaxation dynamics of surface plasmon electronic oscillations in gold and silver nanodots and nanorods, J. Phys. Chem. B 103 (1999) 8410–8426.
[54] S. Link, M.B. Mohamed, M.A. El-Sayed, Simulation of the optical absorption spectra of gold nanorods as a function of their aspect ratio and the medium dielectric constant, J. Phys. Chem. B 103 (1999) 3073–3077.
[55] C. Ungureanu, R.G. Rayavarapu, S. Manohar, T.G.v. Leeuwen, Discrete dipole approximation simulations of gold nanorod optical properties: choice of input parameters and comparison with experiment, J. Appl. Phys. 105 (2009) 102032.
[56] I.I.S. Lim, U. Chandrachud, L. Wang, S. Gal, C.J. Zhong, Assembly-disassembly of DNAs and gold nanoparticles: a strategy of intervention based on oligonucleotides and restriction enzymes, Anal. Chem. 80 (2008) 6038–6044.

[57] I.I.S. Lim, F. Goroleski, D. Mott, N. Kariuki, W. Ip, J. Luo, C.J. Zhong, Adsorption of cyanine dyes on gold nanoparticles and formation of J-aggregates in the nanoparticle assembly, J. Phys. Chem. B 110 (2006) 6673–6682.
[58] I.I.S. Lim, W. Ip, E. Crew, P.N. Njoki, D. Mott, C.J. Zhong, Homocysteine-mediated reactivity and assembly of gold nanoparticles, Langmuir 23 (2007) 826–833.
[59] I.I.S. Lim, M.M. Maye, J. Luo, C.J. Zhong, Kinetic and thermodynamic assessments of the mediator-template assembly of nanoparticles, J. Phys. Chem. B 109 (2005) 2578–2583.
[60] I.M.S. Lim, D. Mott, W. Ip, P.N. Njoki, Y. Pan, S. Zhou, C.J. Zhong, Interparticle interactions of glutathione mediated assembly of gold nanoparticles, Langmuir 24 (2008) 8857–8863.
[61] R. Georgiadis, K.P. Peterlinz, A.W. Peterson, Quantitative measurements and modeling of kinetics in nucleic acid monolayer films using SPR spectroscopy, J. Am. Chem. Soc. 122 (2000) 3166–3173.
[62] S. Chen, R. Pei, T. Zhao, D.J. Dyer, Gold nanoparticle assemblies by metal ion-pyridine complexation and their rectified quantized charging in aqueous solutions, J. Phys. Chem. B 106 (2002) 1903–1908.

## Biographies

**Magdalena Stobiecka** received the M.S. degree in biology from the University of Warmia and Mazury in Olsztyn, Poland, in 2002. She received Ph.D. degree from the Polish Academy of Sciences (PAN) in Olsztyn in 2009 and worked in the Department of Biosensors, PAN, Olsztyn as the Assistant. She coorganized several International Research Symposia "Summer Schools" for graduate students from European countries under the EU grant. She published in the field of biosensors for genetically engineered food, molecularly-templated conductive polymer sensors, DNA, and oligonucleotides and presented papers at the national and international conferences. Since 2008, she has been a postdoctoral researcher at the State University of New York at Potsdam. Her current research interests include DNA-hybridization biosensors, aptamers, piezoimmunosensors, flow-cell analysis, microsensor arrays and lab-on-a-chip systems.

**Maria Hepel** received the M.S. and Ph.D. degrees in chemistry from Jagellonian University in Krakow, Poland. From 1985 she worked as the faculty at the State University of New York at Potsdam where she is now a professor and chair of the Department of Chemistry. She published over 120 papers, 25 chapters in books, and has made over 380 presentations at the national and international symposia. She organized and chaired many symposia at the American Chemical Society, Electrochemical Society and International Society of Electrochemistry Meetings and was the program chair of the 2010 North-East Regional Meeting of ACS. In 2007 she received SUNY Chancellor's Award for Excellence in Research and Creative Endeavor. Her current research interests include DNA intercalation sensors, piezoimmunosensors, sensors for biomarkers of oxidative stress, diabetes, and cancer, fluorescnce energy transfer (FRET and NSET), DNA-hybridization biosensors, aptamers, microsensor arrays and lab-on-a-chip systems, photovoltaics, dye pollutant degradation, and electrochromic devices.

# Ligand exchange effects in gold nanoparticle assembly induced by oxidative stress biomarkers: Homocysteine and cysteine

Magdalena Stobiecka [a], Jeffrey Deeb [a], Maria Hepel [a,b],*

[a] Department of Chemistry, State University of New York at Potsdam, Potsdam, NY 13676, USA
[b] Department of Chemistry, State University of New York at Buffalo, Buffalo, NY 14260, USA

## ARTICLE INFO

## ABSTRACT

The interactions of oxidative stress biomarkers: homocysteine (Hcys) and cysteine (Cys) with the multifunctional gold nanoparticles, important in view of novel biomedical applications in diagnostics and therapy, have been investigated using resonance elastic light scattering (RELS), UV–Vis plasmonic spectroscopy, and high-resolution TEM imaging. The Hcys-induced assembly of gold nanoparticles has been observed for non-ionic surfactant-capped gold nanoparticles as well as for negatively-charged citrate-capped gold nanoparticles. We have observed for the first time the de-aggregation of citrate-capped gold nanoparticle ensembles followed by their conversion to citrate-linked Hcys-capped nanoparticle assemblies. The Cys molecules, which are smaller than Hcys by only one $CH_2$ group, show much less activity. The mechanisms leading to this intriguing disparity in the abilities of these two thioaminoacids to ligand exchange with surfactant- or citrate-capping molecules of the gold nanoparticle shells are proposed on the basis of the experimental evidence, molecular dynamics simulations, and quantum mechanical calculations. For citrate-capped gold nanoparticles, we postulate the formation of surface complexes facilitated by electrostatic attractions and formation of double hydrogen bonds for both Hcys and Cys. The conformational differences between these two kinds of complexes result in marked differences in the distance between –SH groups of the biomarkers to the gold surface and different abilities to induce nanoparticle assembly. Analytical implications of these mechanistic differences are discussed.

© 2009 Elsevier B.V. All rights reserved.

## 1. Introduction

Biomarkers of oxidative and nitrosative stress have recently been the subject of extensive studies [1,2] as the new evidence demonstrates ever increasing number of related diseases. The oxidative stress has been suggested as the causative factor in aging [3] and many diseases such as cadiovascular, diabetes, cancer, autism spectrum disorders (ASD) [4], and others. Among the biomarkers of oxidative stress are small biomolecules such as: ubiquinol [5] which is very labile in the oxidation of low-density lipoprotein (LDL), glutathione (GSH) which is depleted in the presence of organic radicals and peroxides [6], homocysteine [7,8] which has been found at elevated levels in atherosclerosis [9–14], Alzheimer disease [15,16], dementia [15], and poses an increased risk of birth defects [17]. Some biomarkers of oxidative stress are necessary to maintain healthy homeostasis (e.g. glutathione), while others participate in the development of diseases (e.g. homocysteine). For instance, decreased levels of glutathione and increased levels of oxidized glutathione (GSSG) have been observed in plasma, serum and urine samples from individuals diagnosed with ASD [4,18–20]. Homocysteine (Hcys), which is a sulfur-containing amino acid, is formed during a metabolism of methionine to cysteine but the increased concentration of Hcys in plasma ($C_{Hcys} > 15\,\mu M$) is a risk factor for many disorders, including cardiovascular [9–12], renal [21], Alzheimer's [15,16], and other diseases [22]. Redox-related alterations, measured usually as the change in the concentration ratio of GSH/GSSG which is the main redox level maintaining couple in organisms, may also be heritable. Deviations from healthy biomarker concentration levels may result from deficiency of certain vitamins, e.g. B12 and folic acid (in hyperhomocysteinemia). The investigations of oxidative stress biomarkers are important to understand their behavior and role in organisms and to develop sensors and assays for their rapid detection and diagnosis of stress-related disorders.

The reactivities and interactions of the oxidative stress biomarkers have been investigated in conjunction with the development of molecularly-templated polymer films with biorecognition capabilities designed for biomarkers detection [23], fluorimetric assays based on specific reactions [24–26], electrochemical sensors [27,28], colorimetric assays based on nanoparticle assembly [29–32], and the design of immunosensors [33] and other sensors for the analysis of biomarkers or utilizing biomarkers in the sensory film design [34–36]. In particular, in studies of biomolecule-induced gold nanoparticle assembly, the kind of interparticle interactions is the key element of the functionalized nanoparticle self-affinity [37–39]. The interparticle forces include electrostatic [40], zwitterionic [29,40], van der Waals

* Corresponding author. Department of Chemistry, State University of New York at Potsdam, Potsdam, NY 13676, USA. Tel.: +1 315 267 2264; fax: +1 315 267 3170.
E-mail address: hepelmr@potsdam.edu (M. Hepel).

forces [41], as well as hydrogen bonding forces [41–43]. The investigations of functionalized spherical gold nanoparticles and gold nanorods for application in novel assays for GSH [43], cysteine [32,44–48] and homocysteine [29,30,45,49] have been reported. The gold nanoparticle cores with protective shells of self-assembled monolayers (SAM) of thiolates [50,51], surfactants [47,52,53], citrate ions [48], and others can be utilized in the analysis. A difference in the sensitivity of the gold nanoparticle assembly process to structurally similar cysteine and homocysteine molecules, which differ only by one $CH_2$ group, has been found [32,46,47]. Probing the interactions of biomolecules with gold nanoparticles and their influence on surface plasmon resonance and the elastic light scattering cross-section has potential applications in the development of novel assays for these molecules.

The gold nanoparticle assembly process observed upon the addition of biomolecules is believed to be due to the ligand exchange [54] followed by the attractive interparticle interactions [29,48]. According to the thermodynamic stability, the citrate shell is less strongly bound than cysteine shell and the latter is less strongly bound than homocysteine shell. In practice, the kinetic hindrance may slow down considerably the ligand exchange processes. Also, the interparticle molecular-linking may induce an assembly before the completion of a ligand exchange process, as we have recently observed in the case of GSH-induced assembly.

The biomolecule-induced gold nanoparticle assembly process can be monitored using surface plasmon absorbance band shifts. The oscillation frequency of the local surface plasmon (SP) is very sensitive to the changes in dielectric environment of nanoparticles and distance between nanoparticles within $5r$ range (where $r$ is the nanoparticle radius). Theoretical studies of plasmonic oscillations [55–65] and SP absorbance spectra [66–74] have enabled the understanding of mechanisms leading to the absorbance maximum shifts associated with the assembly processes. The hydrodynamic radius of nanoparticle aggregates can be measured using dynamic light scattering although the complex dielectric medium and formation of aggregates of small particles may complicate the analysis. The use of transmission electron microscopy (HR-TEM) has been so far the best in determining the nanoparticle diameters and presenting images of aggregated nanoparticles. In this work, we have applied UV–Vis plasmonic absorbance measurements, HR-TEM, and the resonance elastic light scattering (RELS) spectroscopy [75–87]. The latter provides very sensitive measure of the degree of gold nanoparticle assembly. The gold nanoparticles show enhanced scattering during the assembly process due to the collective oscillation of local surface plasmons in nanoparticles bound in an ensemble.

In this work, the assembly of gold nanoparticles induced by oxidative stress biomarkers, homocysteine and cysteine, has been investigated using non-ionic fluorosurfactant-capped gold nanoparticles and negatively-charged citrate-capped gold nanoparticles. The remarkable differences in ligand exchange abilities of the homocysteine and cysteine, have been observed for both the charged and uncharged nanoparticle shells. Different mechanisms leading to these effects for uncharged and charged nanoparticle shells are proposed. The elucidation of these mechanisms is crucial for analytical determination of structurally similar cysteine and homocysteine using rapid and inexpensive measurement techniques important for oxidative stress screening and prevention of environmental pollution effects on human health.

## 2. Experimental

### 2.1. Chemicals

All chemicals used for investigations were of analytical grade purity. DL-Homocysteine ($HS(CH_2)_3NH_2COOH$), L-Cysteine ($HS(CH_2)_2NH_2COOH$), tetrachloroauric(III) acid trihydrate ($HAuCl_4 \cdot 3H_2O$)

with 99.9+% metals basis, D-Methionine, and L-glutathione (GSH) reduced (minimum 99%), were purchased from Sigma Aldrich Chemical Company (Atlanta, GA, U.S.A.) and used as received. ZONYL FSN-100, a fluorocarbon-ether surfactant (FES), with nominal composition $CF_3(CF_2)_m(C_2H_4O)_nCH_2OH$ and average molecular mass $M = ~950$ g/mol was obtained from Sigma Aldrich. Sodium citrate dihydrate ($HOC(COONa)(CH_2COONa)_2 \cdot 2H_2O$) was received from J.T. Baker Chemical Co. (Phillipsburg, NJ, U.S.A.). Sodium borohydride ($NaBH_4$) was obtained from Fisher Scientific Company. L(+) Histidine was purchased from Eastman Organic Chemicals (Rochester, NY, U.S.A.). Solutions were prepared using Millipore (Billerica, MA, U.S.A.) Milli-Q deionized water (conductivity $\sigma = 55$ nS/cm). They were deoxygenated by bubbling with purified argon.

### 2.2. Apparatus

The imaging analyses of Au nanoparticles were performed using high-resolution transmission electron microscopy (HR-TEM) with Model JEM-2010 (Jeol, West Chester, PA, U.S.A.) HR-TEM instrument (200 kV) and imaging with a Jeol Model JSM-7400F field-emission scanning electron microscope (FE-SEM). The elastic light scattering spectra were recorded using LS55 Spectrometer (Perkin Elmer, Waltham, MA, U.S.A.) equipped with 20 kW Xenon light source operating in 8 μs pulsing mode. Pulse width at half height was less than 10 μs. Separate monochromators for the incident beam and the detector beam enabled to use monochromatic radiation with wavelengths from 200 nm to 800 nm with 1 nm resolution. Additionally, the system was equipped with sharp cut-off filters: 290, 350, 390, 430, 515 nm. The dual detector system consisted of a photo-multiplier tube (PMT) and an avalanche photodiode. The RELS spectra were obtained at 90° angle from the incident (excitation) light beam. The excitation beam monochromator was either scanned simultaneously with the detector beam monochromator ($\Delta\lambda = 0$) or set at a constant excitation wavelength. The UV–Vis spectra were recorded using Perkin Elmer Lambda 50 Spectrophotometer in the range 400 to 900 nm or Ocean Optics (Dunedin, FL, U.S.A.) Model R4000 Precision Spectrometer in the range from 340 nm to 900 nm.

### 2.3. Procedures

The Au nanoparticles were synthesized according to the published procedure [88]. Briefly, to obtain 5 nm AuNP, 10 mM $HAuCl_4$ was mixed with 10 mM trisodium citrate solution (ratio 1: 3.75) and poured to distilled water (109 mL). The obtained solution was vigorously stirred and fresh cold $NaBH_4$ solution (5 mM, 8.9 mL) was added dropwise. The solution slowly turned light grey and then ruby red. Stirring was maintained for 30 min. The obtained citrate-capped core-shell Au nanoparticles (AuNP) were stored at 4 °C. Their size, determined by HR-TEM imaging and UV–Vis surface plasmon absorption was 5.0 nm. The concentrations of AuNP's are given in moles of particles per 1 L of solution (usually, in the nM range). The RELS and UV–Vis spectra for samples were obtained with 1 min of mixing of AuNP with biomolecule solutions, unless otherwise stated.

Quantum mechanical calculations of electronic structures for a model fluorocarbon-ether surfactant, citric acid, cysteine and homocysteine were performed using modified Hartree–Fock methods [89,90] with 6–31G* basis set and pseudopotentials, semi-empirical PM3 method, and density functional theory (DFT) with B3LYP functional. The molecular dynamics simulations and quantum mechanical calculations were carried out using procedures embedded in Wavefunction (Irvine, CA, U.S.A.) Spartan 6. The electron density and local density of states (LDOS) are expressed in atomic units, $au^{-3}$, where 1 au = 0.529157 Å and 1 $au^{-3}$ = 6.749108 $Å^{-3}$.

## 3. Results and discussion

### 3.1. Plasmonic spectroscopy of thioaminoacid-induced assembly of gold nanoparticles protected by ZONYL

Fluorosurfactants provide similar advantages to other surfactants but, in addition, show high degree of chemical inertness. For these reasons they have recently been applied in chemical analysis [52]. The ZONYL fluorosurfactant is known to form self-assembled monolayers on gold surfaces rendering the surface more hydrophobic and significantly retarding the gold oxide formation processes [91]. In the case of AuNP, it stabilizes gold colloids by forming tight shells around nanoparticle cores with hydrophilic heads oriented toward Au surface and fluorocarbon tails forming hydrophobic non-interacting external surface. Although this surfactant forms water-tight shells, its bonding to a gold surface is not as strong as that of thiolates. Therefore, in their presence, ZONYL is replaced in a ligand exchange process by thiols, including thioaminoacids, homocysteine and cysteine, investigated in this work, provided that sufficiently high concentration of these agents is used and long enough time is allowed.

The HR-TEM images of fluorosurfactant-capped AuNP's are presented in Fig. 1 before (a) and after (b–d) homocysteine-induced nanoparticle framework assembly.

The ligand exchange process taking place upon addition of homocysteine to ZONYL-capped AuNP can be monitored using SP-band absorbance of AuNP, as illustrated in Fig. 2. The UV–Vis spectra 1–9 were recorded for increasing concentrations of Hcys, from 0 to 22.2 μM and constant concentration of $AuNP_{5\ nm}$ (6 nM). It is seen that the SP band shifts toward longer wavelengths and the maximum absorbance increases with increasing $C_{Hcys}$. These observations are consistent with ligand exchange process:

$$AuNP\,/\,FES_x + yHcys = AuNP\,/\,Hcys_y + xFES$$
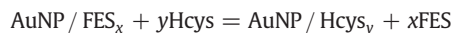
where $x \approx y$, followed by interparticle molecular linking of AuNP/Hcys through direct Hcys-Hcys interactions. At the pH of these experiments (pH = 6.0), homocysteine exists as a zwitterion with α-amino group protonated ($-NH_3^+$) and carboxylic group dissociated ($COO^-$). Therefore, the zwitterionic interparticle binding between Hcys-capped AuNP is playing a predominant role as recently discussed by Zhong et al. [29].
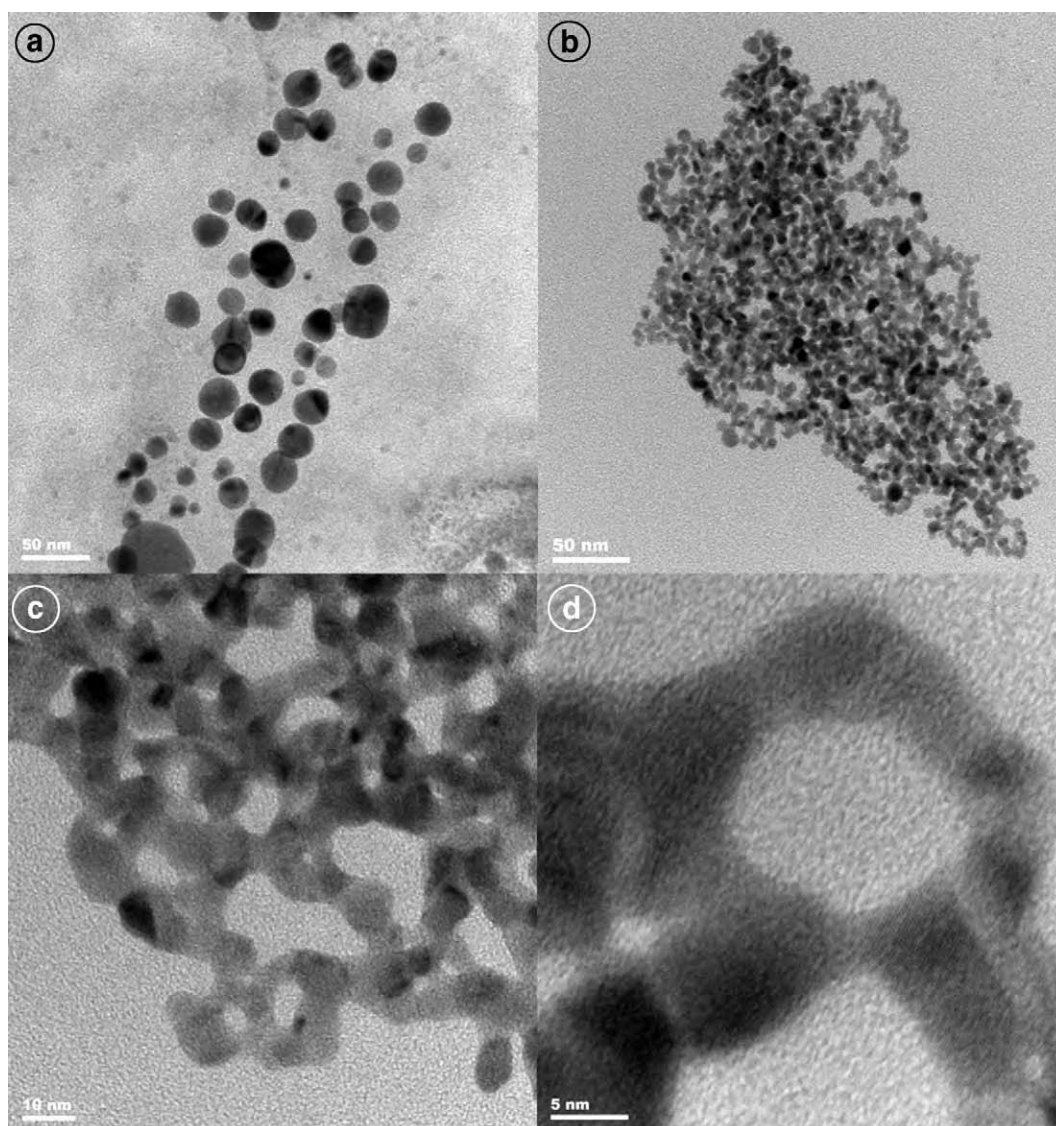


**Fig. 1.** HR-TEM images of ZONYL-capped gold nsanoparticles before (a) and after assembly with 15 μM homocysteine (b–d); $C_{AuNP}$ = 6 nM, $C_{ZONYL}$ = 0.22 %, pH = 6; bar size: (a) 50 nm, (b) 50 nm, (c) 10 nm, (d) 5 nm.
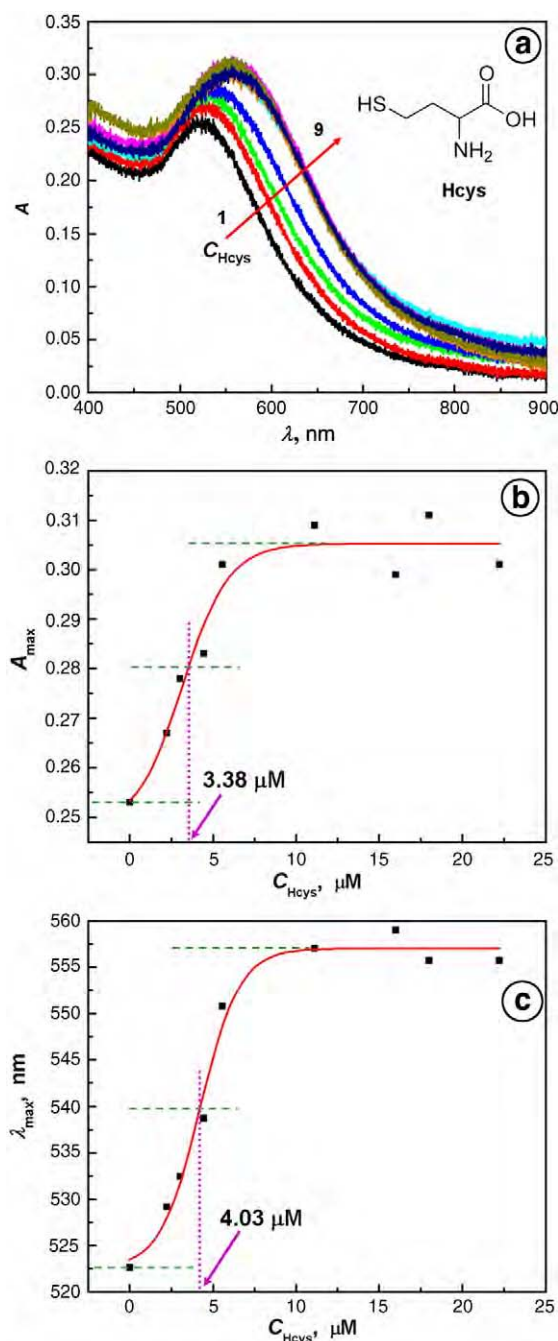
Fig. 2. (a) Absorbance spectra for ZONYL-capped AuNP for different concentrations of homocysteine, $C_{Hcys}$ [μM]: (1) 0, (2) 2.22, (3) 3, (4) 4.44, (5) 5.56, (6) 11.11, (7) 16, (8) 18, (9) 22.22. $C_{AuNP}=6$ nM, $C_{ZONYL}=0.22$ %, pH = 6; (b–c) dependence of (b) $\lambda_{max}$ and (c) $A_{max}$ vs. $C_{Hcys}$.

The bathochromic shift of the surface plasmon peak ($\Delta\lambda_{max}=36$ nm, for 16 μM Hcys) corresponds to the formation of small Hcys-linked AuNP ensembles. The increase of SP absorbance by 21% (from 0.253 to 0.305, Fig. 1b) indicates on the collective oscillations of local surface plasmons in AuNP that form these ensembles. The collective oscillation of local surface plasmons is excited when the distance $d$ between AuNP is: $d<5r$, where $r$ is the AuNP radius. The absorbance maximum increases with $C_{Hcys}$ and reaches the saturation value at $C_{Hcys}>7$ μM, with the half-absorbance change appearing at $C_{Hcys}=3.38$ μM. The value of $\lambda_{max}$ also reaches saturation at $C_{Hcys}>7$ μM (Fig. 1c). Therefore, we can assume that above 7 μM Hcys concentration the ligand exchange process has completed and nanoparticle shells are saturated with Hcys.

Extensive studies of the surface plasmon absorbance for various AuNP systems have been carried out by several groups [37,38,42, 50,51,70,86,92–99]. In particular, it follows from studies of the homocysteine-mediated assembly of AuNP that the interparticle zwitterion interaction of the Hcys-Au system is particularly strong [29] and that the Hcys-mediated assembly of AuNP can be accelerated by an increased temperature and ionic strength of the solution thus reducing the barrier for Hcys attachment to gold nanoparticle surface [29]. Also, the assembly can be reversed by the pH change [29,30].

Similar experiments performed with cysteine indicate that at higher concentrations ($C>15$ μM) the kinetics of ligand exchange for both Hcys and Cys is very fast and the exchange is completed within 1 min of mixing AuNP solution with the thioaminoacids. However, at lower concentrations, the ligand exchange is considerably faster for Hcys than for Cys.

*3.2. Resonance scattering of the thioaminoacid-mediated ZONYL-capped gold nanoparticle assembly process*

Typical light scattering spectrum for a ZONYL FSN surfactant-capped 5 nm diameter Au nanoparticles ($AuNP_{5\ nm}$) in solution is presented in Fig. 3, curve 1, for $AuNP_{5\ nm}$ concentration of 6 nM and a constant excitation wavelength $\lambda_{ex}=550$ nm (1.94 eV). The strong resonant Rayleigh scattering from $AuNP_{5\ nm}$ nanoparticles in solution results from the absorption of photons at 550 nm followed by secondary emission without any energy loss. Thus, the coherent elastic Rayleigh scattering with Gaussian peak shape centered at $\lambda_{em}=\lambda_{ex}=550$ nm is observed. The narrow linewidth of $\Delta\lambda=15$ nm confirms that the effects due to radiation broadening, density fluctuation, fluorescence, and inelastic Raman scattering are negligible. Note that the background intensity is very low (virtually zero), which is leading to the well defined RELS peaks.

The addition of homocysteine to the ZONYL-capped $AuNP_{5\ nm}$ nanoparticles results in strong enhancement of Rayleigh scattering, as indicated in Fig. 3, curves 2–9, obtained for 6 nM $AuNP_{5\ nm}+x$ μM Hcys, where $x=0$ ... 22.2 μM. Upon addition of Hcys, the solution pH was maintained at pH = 6.0. This pH value is within the range of predominantly neutral (zwitterionic) form of homocysteine (pH = 2.22 to 8.87; $pK_{a,1}=2.22$ (COOH), $pK_{a,2}=8.87$ (NH$_2$), $pK_{a,3}=10.86$ (SH)). The strong enhancement of RELS from $AuNP_{5\ nm}$ by Hcys molecules is expected since any size increase of AuNP due to the aggregate formation associated with interparticle interactions with zwitterionic Hcy-Hcys cross-linking should result in stronger scattering. The strong sixth-power dependence of elastic scattering intensity $I_{sc}$ on the
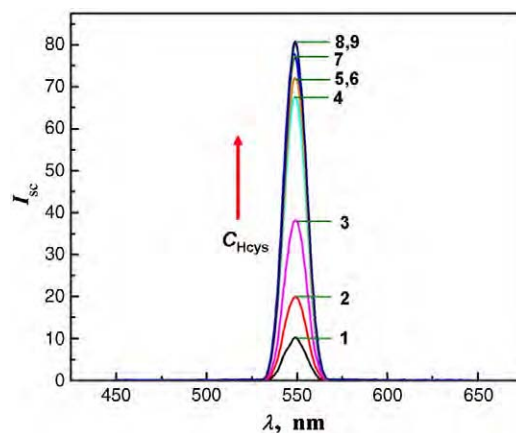


Fig. 3. Resonance elastic light scattering spectra for ZONYL-capped $AuNP_{5\ nm}$ for different concentrations of homocysteine, $C_{Hcys}$ [μM]: (1) 0, (2) 2.22, (3) 3, (4) 4.44, (5) 5.56, (6) 14, (7) 16, (8) 18, (9) 22.22. $C_{AuNP}=6$ nM, $C_{ZONYL}=0.22$ %, pH = 6, $\lambda_{ex}=550$ nm.

nanoparticle diameter $a$ follows from the Rayleigh equation for light scattering from small particles:

$$I_{sc} = I_0 N \frac{(1 + \cos^2 \theta)}{2R^2} \left(\frac{2\pi}{\lambda}\right)^4 \frac{([n_2 - n_1]^2 - 1)}{([n_2 - n_1]^2 + 2)} \left(\frac{a}{2}\right)^6 \qquad (1)$$

where $n_1$ and $n_2$ are the refractive indices for the solution and particles, respectively, $\lambda$ is the wavelength of incident light beam, $\theta$ is the scattering angle, $N$ is the number of particles, and $I_0$ is the constant. For $\lambda = $ const and other experimental conditions ($\theta$, $R$, $I_0$) unchanged, one obtains:

$$\frac{I_{sc,2}}{I_{sc,1}} = \frac{N_2 a_2^6}{N_1 a_1^6} = c_{rel} a_{rel}^6 \qquad (2)$$

where indices 1,2 stand for the particles before and after Hcys addition, respectively, $c_{rel} = N_2/N_1$ is the relative concentration of particles after addition of Hcys, and $a_{rel} = a_2/a_1$ is the relative diameter of particles after addition of Hcys. Therefore, the increase in the particle diameter can be estimated as follows:

$$a_{rel} = \left[\frac{I_{sc,2}}{c_{rel} I_{sc,1}}\right]^{1/6} \qquad (3)$$

Furthermore, the relative concentration $c_{rel}$, which is equal to 1 for a no-aggregation condition and less than 1 for aggregation, can be expressed by:

$$c_{rel} = \frac{N_2}{N_1} = \frac{V_1}{V_2} \qquad (4)$$

where $V_i$ is the effective volume of a single aggregate $i$. Substituting $V_i = (4/3)\pi(a_i/2)^3$, one obtains:

$$c_{rel} = a_{rel}^{-3} \qquad (5)$$

and:

$$\frac{I_{sc,2}}{I_{sc,1}} = a_{rel}^3 \qquad (6)$$

Therefore, the increase of the particle diameter can be estimated as follows:

$$a_{rel} = \sqrt[3]{\frac{I_{sc,2}}{I_{sc,1}}} \qquad (7)$$

From the data of Fig. 3, the scattering intensity increase is: $I_{sc,2}/I_{sc,1} = 80.44/10.26 = 7.84$ and, hence,

$$a_{rel} = 1.99 \qquad (8)$$

This means that most likely small aggregates composed of only few nanoparticles (e.g. 2–6) are formed. Since a small contribution to the change in particle diameter is also due to the ligand exchange, we have to estimate this contribution. The thickness of the ZONYL shell around AuNP is 1.1 nm (vertical, fully extended orientation, ZONYL FSN-100, with formula $CF_3(CF_2)_m(C_2H_4O)_nCH_2OH$ and average $m = 12$, $n = 6$ assumed on the basis of molmass $M = 950$ g/mol) and the height of Hcys molecule adsorbed on Au is on the order of 0.5 nm based on quantum mechanical evaluation for Hcys adsorbed on a solid Au surface. The structure and dimensions of ZONYL and Hcys molecules are shown later on (Figs. 8–11). Hence, the diameter of a single AuNP, with core of 5 nm diameter would decrease from ca. 7.2 nm to 6.0 nm. Obviously, the diameter decrease cannot explain the observed ~8-fold scattering intensity increase. Therefore, we can con-

clude that Hcys-mediated assembly of AuNP's occurs upon addition of Hcys to the ZONYL-capped AuNP solution and the effective diameter of assemblies is: $a = 1.99 \, a_0$ (where $a_0$ is the diameter of Hcys-capped AuNP). This assembly results in a large increase in $I_{sc}$ in accord with the data of Fig. 3. Because there are only very weak interactions between the Hcys molecules and hydrophobic tail of ZONYL, any Hcys-mediated bridging of ZONYL-capped AuNP's, such as that observed upon addition of GSH to citrate-capped AuNP's, cannot take place. Hence, the ligand exchange is the first stage of the interactions between Hcys and ZONYL-capped AuNP and it is followed by Hcys-Hcys interparticle interactions leading to AuNP assembly.

### 3.3. Ligand exchange processes for ZONYL-capped gold nanoparticles

It is interesting to compare the ligand exchange processes for different aminoacid ligands and ZONYL-capped AuNP. As reported earlier [24,52], these processes differ considerably between aminoacids and these differences are due to highly selective ZONYL-replacement abilities of the particular aminoacids. The plots of RELS intensity vs. aminoacid concentration measured at $\lambda_{ex} = 550$ nm for Hcys, methionine, alanine, histidine, and glutathione, are presented in Fig. 4. They show a strong increase of $I_{sc}$ with $C$ for homocysteine and apparent no response for other aminoacids and glutathione. The $I_{sc}$ vs. $C_{Hcys}$ dependence is sigmoidal with an inflection point at low Hcys concentration indicating a high affinity of Hcys for Au surface, higher than that of ZONYL. From a Boltzmann function fitted to the experimental data for Hcys and ZONYL, we obtain:

$$I_{sc} = A_2 + (A_1 - A_2) / (1 + \exp[(C - C_{1/2}) / s]) \qquad (9)$$

where $A_1$, $A_2$ — are the lower and higher $I_{sc}$ plateaus, $C_{1/2}$ is the concentration at the inflection point, and $s$ is the slope parameter. The value of $C_{1/2} = 3$ μM and the characteristic constant $K_{1/2}^*$ describing the "half-reaction" state of the ligand exchange in the ZONYL replacement by Hcys is: $K_{1/2}^* = 3.3 \times 10^5$ M$^{-1}$ (note that the value and units of this phenomenological half-reaction-state equilibrium constant are typically different than those for a thermodynamic equilibrium constant for higher order reactions involving more than single molecules). The high value of $K_{1/2}^*$ confirms a high affinity of Hcys to the gold surface in comparison to that of the ZONYL surfactant.

The longer elution time for Hcys than for Cys observed in C18 column chromatography experiments [24,52] is consistent with higher affinity of Hcys than Cys to hydrophobic chains. In the setting of a ZONYL-capped AuNP, this would translate to a slower transfer of Hcys through a ZONYL shell and a slower kinetics of the ligand
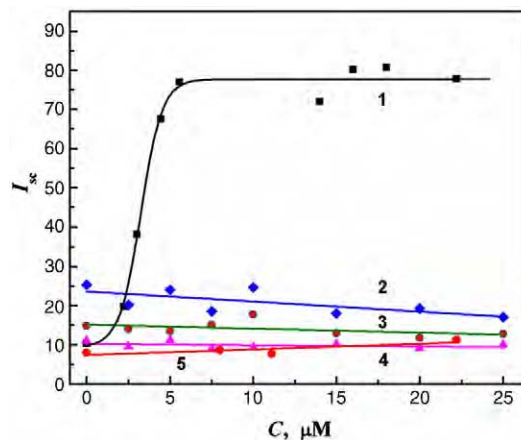


Fig. 4. Dependence of elastic light scattering intensity maximum $I_{sc,max}$ for ZONYL-capped AuNP on concentration of analytes: (1) homocysteine, (2) methionine, (3) alanine, (4) histidine, (5) glutathione, $C_{AuNP} = 6$ nM, $C_{ZONYL} = 0.22\%$, pH = 6, $\lambda_{ex} = 550$ nm.

exchange process. Since the opposite is observed, this means that other factors play a role in the ligand exchange mechanism. The interactions of Hcys and Cys with ZONYL molecules are further discussed later on by employing molecular dynamic simulations of a model ZONYL and biomarker molecules.

### 3.4. Interactions of thioaminoacids with citrate ligands of core-shell gold nanoparticles
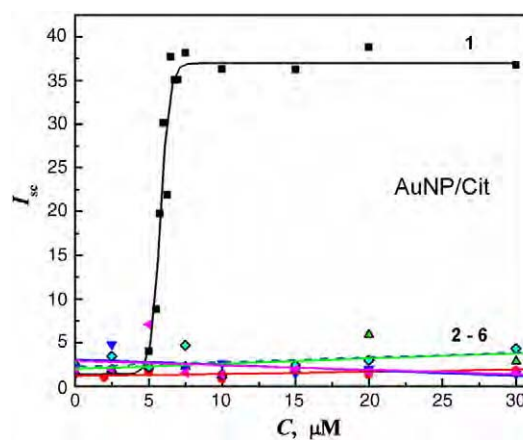
Upon addition of homocysteine to citrate-capped AuNP, an increase in resonance elastic light scattering, similar to the one described for ZONYL-capped AuNP, is also observed (Fig. 5), provided that the solution pH is carefully controlled. The RELS spectra in Fig. 5 were obtained at pH = 5.0 for $\lambda_{ex} = 560$ nm, for increasing concentrations of Hcys from $C_{Hcys} = 0$ to 15 μM. The increase in scattering intensity upon addition of 15 μM Hcys is $I_{sc,2}/I_{sc,1} = 36.2/1.91 = 19.0$ (mean of 5 measurements). The 19-fold increase in scattering intensity clearly indicates on the homocysteine-induced assembly of AuNP. Utilizing again Eq. (7), we obtain for the increase of particle diameter: $a_{rel} = 2.7$.

Similar RELS experiments carried out for other aminoacid ligands and glutathione, presented in Fig. 6, show that the RELS response is highly selective to Hcys, consistent with recent findings [29,43,46] showing that thiol-containing aminoacids adsorb preferentially on a gold surface while glutathione (at neutral pH) is repelled from the citrate shell of nanoparticles. The mechanisms leading to this high selectivity are not well understood, though the importance of this selectivity for analytical determinations of homocysteine in a matrix of aminoacids and glutathione is high.

In order to explore the effects of protonation equilibria for species in solution and in the protective SAM environment of gold nanoparticle shells, we have performed RELS measurements for Hcys and citrate-capped AuNP at three different solution pH: 2.0, 5.0, and 9.0. The plot of scattering intensity $I_{sc}$ vs. $C_{Hcys}$ for these three media is presented in Fig. 7. The three dependencies of $I_{sc}$ vs. $C_{Hcys}$ for different pH values show completely different behaviors. The curve 1 for pH = 2.0 shows a scattering intensity decrease with increasing $C_{Hcys}$ and establishment of a plateau for $C_{Hcys} > 4$ μM. Curve 2 shows a sigmoidal shape with the onset of scattering at $C_{Hcys} = 5$ μM and establishment of a new level of scattering intensity plateau for $C_{Hcys} > 7$ μM. In the case of the third curve, for pH = 9.0, there is virtually no scattering change seen for the entire concentration range of Hcys examined and the level of scattering is very low ($I_{sc} \approx 8$, for 20 μM Hcys). Note that the scattering intensity levels established for pH = 2.0 and pH = 5.0 at higher concentrations of Hcys, are different.
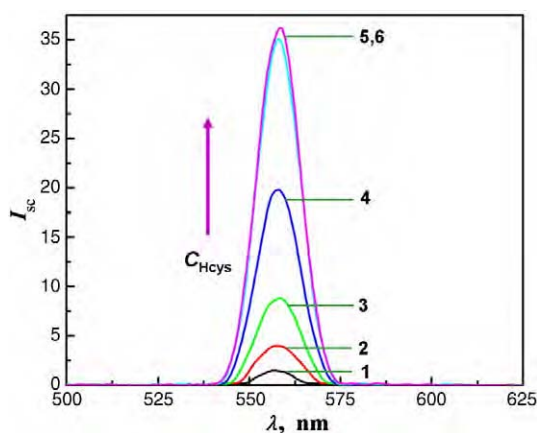


**Fig. 6.** Dependence of elastic light scattering intensity maximum $I_{sc,max}$ for citrate-capped AuNP$_{5\,nm}$ on concentration of analytes: (1) homocysteine, (2) methionine, (3) alanine, (4) histidine, (5) glutathione, (6) cysteine, $C_{AuNP} = 3.8$ nM, pH = 5, $\lambda_{ex} = 560$ nm.

The elucidation of the mechanism of processes leading to the complex behavior of the citrate-capped AuNP − homocysteine system is a key element to understanding the reactivity and assembling properties of functionalized AuNP and their interactions with small biomolecules. The three situations represented by the data of Fig. 7 can be analyzed as follows:

(i) The low elastic scattering intensity observed at pH = 9 (curve 3) for all Hcys concentrations examined is certainly due to the high gold colloid stability which is associated with strong electrostatic interparticle repulsions between deprotonated carboxyl groups that exist in the citrate shell before and in the Hcys-shell after the ligand exchange has taken place.

(ii) The situation changes at pH = 5 (curve 2) where citrates are still predominantly deprotonated (p$K_{a,1} = 3.09$, p$K_{a,2} = 4.75$, p$K_{a,3} = 5.41$) but homocysteine exists as a zwitterion with protonated –NH$_3^+$ group and dissociated COO$^-$ group (p$K_{a,1} = 2.22$ (COOH), p$K_{a,2} = 8.87$ (NH$_2$)). Thus, at low Hcys concentrations ($C_{Hcys} < 5$ μM), scattering is low since it is dominated by interparticle repulsions of negatively-charged citrate shells. As the ligand exchange process progresses, the citrate ions are being replaced by the neutral Hcys molecules. The progression is accelerated at higher Hcys concentrations. The switch from low elastic light scattering intensity to high intensity is observed in the concentration range: 5 μM < $C_{Hcys}$ < 7 μM. At $C_{Hcys} = 7$ μM, the



**Fig. 5.** Resonance elastic light scattering spectra for citrate-capped AuNP$_{5\,nm}$ for different concentrations of homocysteine, $C_{Hcys}$ [μM]: (1) 0, (2) 5, (3) 5.5, (4) 5.75, (5) 6.75, (6) 15, $C_{AuNP} = 3.8$ nM, pH = 5, $\lambda_{ex} = 560$ nm.
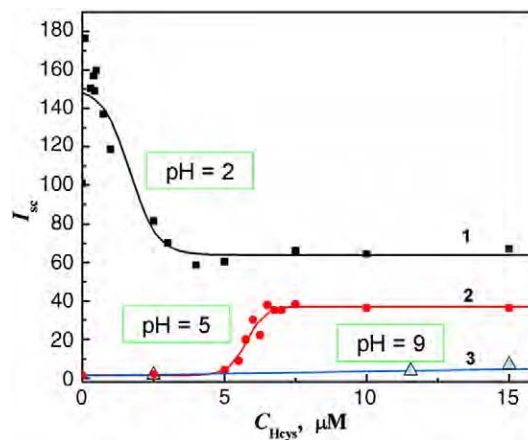


**Fig. 7.** Dependence of elastic light scattering intensity maximum $I_{sc,max}$ on concentration of homocysteine $C_{Hcys}$ for citrate-capped AuNP$_{5\,nm}$ for different solution pH: (1) pH = 5 and (2) pH = 2.

saturation level is attained. This level can be ascribed to small ensembles of Hcys-linked AuNP where the interparticle attractions are attributed to strong Hcys-Hcys zwitterionic interactions.

(iii) In an acidic solution at low pH (curve 1, pH = 2) and in the absence of homocysteine, a strong scattering intensity is observed which is due to the extensive interparticle hydrogen bonding. This occurs because at this pH citrates are predominantly undissociated ($pK_{a,1} = 3.09$, $pK_{a,2} = 4.75$, $pK_{a,3} = 5.41$, for citric acid) rendering the gold colloid unstable. The hydrogen bonding is responsible for the formation of gold nanoparticle networks and since the scattering intensity strongly increases with the aggregate size, a high scattering intensity is observed. Upon the addition of homocysteine, the light scattering intensity unexpectedly decreases to a new level, approximately at 50% of the initial scattering intensity value. This can be rationalized by assuming the dismantling of the initial citrate-linked gold nanoparticle ensembles and replenishing the nanoparticle shells with homocysteine in a ligand exchange process. While the newly formed shells are more strongly bound to the gold cores than citric acid based shells do, the Hcys molecules at pH = 2 are partially positively charged and cannot form as large the nanoparticle aggregates as citrate-capped AuNP do. In fact, one should expect interparticle repulsions of Hcys-capped AuNP at pH = 2 since $pK_{a,1} = 2.22$ (COOH), $pK_{a,2} = 8.87$ ($NH_2$) for homocysteine. There are two plausible explanations of this behavior. On one hand, the reported value of $pK_{a,1}$ for Hcys, which has been determined for the solution phase, is not relevant to Hcys molecules adsorbed on gold. A shift of the value of $pK_{a,1}$ to somewhat lower values, would make the Hcys molecules still zwitterionic at pH = 2. However, to evaluate this possibility, the $pK_a$ values for surface bound homocysteine should be determined. On the other hand, some of the partially dissociated citrate molecules may participate in the neutralization and cross-linking of Hcys-capped AuNP. The level of light scattering intensity indicates that the nanoparticle ensembles formed are larger than those formed at pH = 5 where pure zwitterionic interactions have been found. Therefore, participation of citrate ligands in the gold nanoparticle cross-linking is likely to occur.

In summary, we have observed for the first time the scattering spectra for the de-aggregation of citrate-capped gold nanoparticle ensembles followed by their conversion to citrate-linked Hcys-capped nanoparticle assemblies.

*3.5. Molecular dynamics and quantum mechanical analysis of ligand exchange processes for core-shell gold nanoparticles*

The two main monolayer-protective types of shells for AuNP examined in this work differ considerably in their composition and properties, yet they both provide selectivity toward homocysteine versus cysteine in the nanoparticle assembly process. In order to elucidate the intriguing difference one methylene group makes in the behavior of cysteine ($HS–(CH_2)_2–NH_2–COOH$) and homocysteine ($HS–(CH_2)_3–NH_2–COOH$), we have performed molecular dynamics and quantum mechanical calculations to characterize the kind of intermediate structures that form on approach of Cys and Hcys molecules to a charged citrate-capped gold nanoparticle. Molecular dynamics simulations have also been carried out to evaluate the interactions of Hcys and Cys with a non-ionic fluorosurfactant-capped gold nanoparticle.

A model gold nanoparticle coated with a monolayer of a fluorocarbon-ether surfactant is presented in Fig. 8. The fluorosurfactant used for model calculations has a composition $CF_3(CF_2)_m(C_2H_4O)_nH$ and consists of a hydrophobic fluorocarbon tail and an ethoxylated chain $–(C_2H_4O)_n–$, with assumed chain lengths: $m = 6$ and $n = 4$. The formation of a tight hydrophobic shell is consistent with the ZONYL-AuNP core-shell structure following studies on Au solid
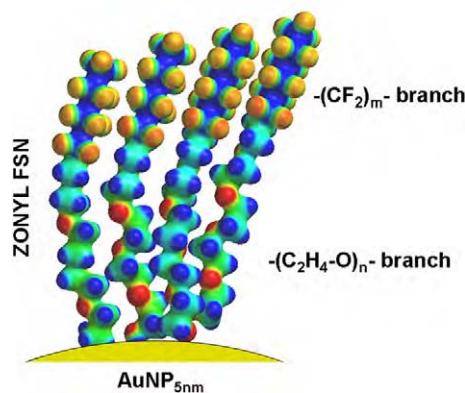


**Fig. 8.** Model ZONYL-capped gold nanoparticle; electron density surfaces for $d = 0.08$ au$^{-3}$, calculated for a fluorosurfactant molecule with formula $CF_3(CF_2)_m(C_2H_4O)_nH$ with $m = 6$, $n = 4$, with electrostatic potential map (color coded from negative — red, to positive — blue).

electrode surfaces [91]. In order to understand the behavior of cysteine and homocysteine in the surroundings of a fluorosurfactant shell, we have performed molecular dynamics simulations of the interactions of a biomarker with different parts of the fluorosurfactant molecule: (a) the top –$CF_3$ group of the molecule, (b) the side of the $–(CF_2)_m–$ tail, and (c) the side of the ethoxy chain. In Fig. 9, shown are cysteine molecules interacting with a fluorosurfactant molecule at these three positions. While there is virtually no effect of cysteine on the conformation of the fluorosurfactant molecule when cysteine interacts at the top or at the side of the hydrophobic tail, there is a change of the conformation observed when cysteine interacts with the ethoxylated part of the fluorosurfactant. A tendency of the ethoxy chain toward surrounding the cysteine molecule is observed in later stages of the simulation. Similar molecular dynamics simulations were performed for homocysteine. Fig. 10 illustrates the interactions of homocysteine with the top of the surfactant molecule, the side of the hydrophobic tail and the side of the ethoxylated chain. Again, there are no conformational changes in the surfactant molecule when homocysteine interacts with the hydrophobic tail. There are some
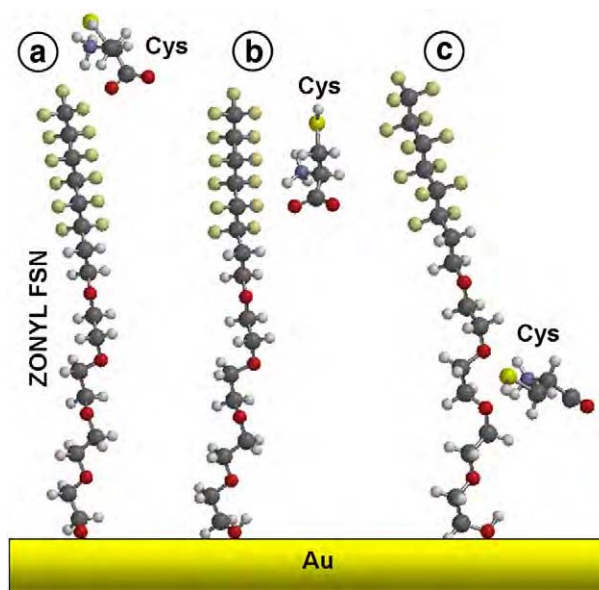


**Fig. 9.** Molecular dynamics simulations of interactions of cysteine with a model fluorosurfactant molecule with formula $CF3(CF2)m(C2H4O)nH$ with $m = 6$, $n = 4$; positions of cysteine: (a) at the top of the surfactant molecule, (b) at the side of the hydrophobic $–(CF2)m–$ chain, and (c) at the side of ethoxy chain.
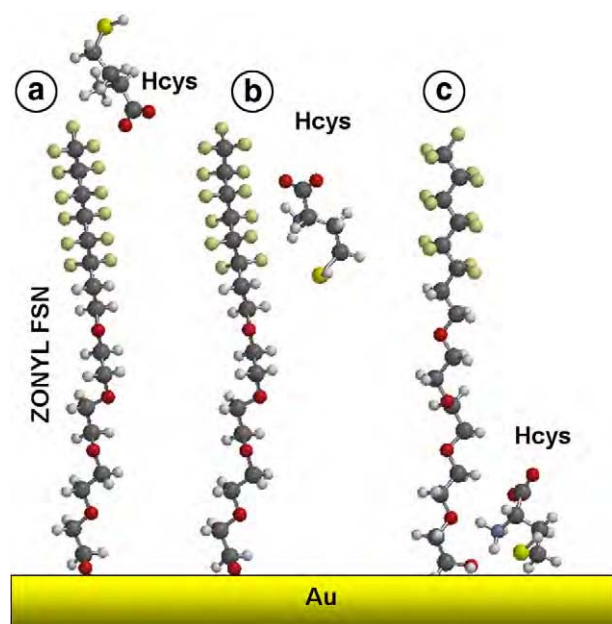
**Fig. 10.** Molecular dynamics simulations of interactions of homocysteine with a model fluorosurfactant molecule with formula $CF_3(CF_2)_m(C_2H_4O)_nH$ with $m = 6$, $n = 4$; positions of homocysteine: (a) at the top of the surfactant molecule, (b) at the side of the hydrophobic $-(CF_2)_m-$ chain, and (c) at the side of ethoxy chain.



**Fig. 11.** Interactions of cysteine and homocysteine with citrate ions in a ligand exchange process: (a, b) surface complex formation through hydrogen bonding calculated for (a) Cit-Cys and (b) Cit-Hcys using molecular dyn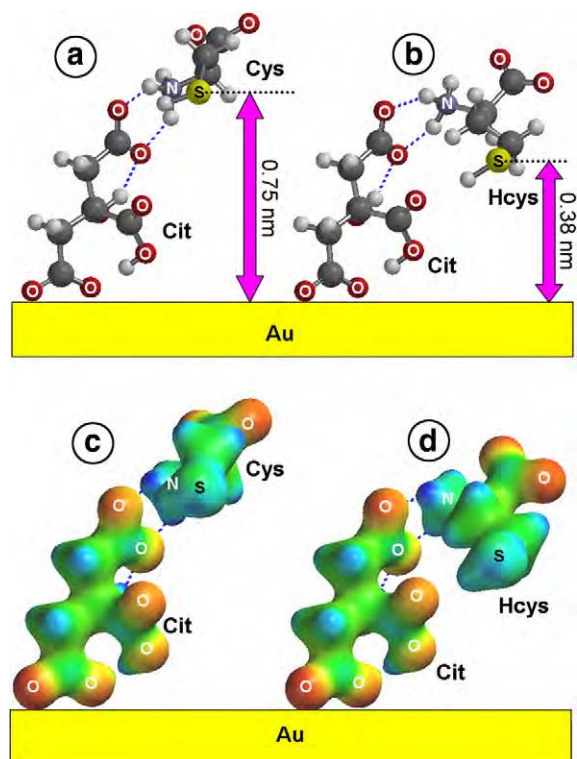amics, and (c, d) electron density surfaces for $d = 0.08$ au$^{-3}$, with electrostatic potential map for (c) Cit-Cys and (d) Cit-Hcys; electrostatic potential: color coded from negative – red to positive – blue.

conformational changes in the surfactant molecule when homocysteine interacts with ethoxyleted chain, but these changes are much smaller than in the case of cysteine. This may be due to higher polarization of cysteine than homocysteine. The ethoxylated chain attempts to surround the smaller cysteine molecule while lowering the system energy. Therefore, it seems that the stronger interaction of cysteine with the fluorosurfactant may slow down considerably the adsorption competition between cysteine and fluorosurfactant at the surface of an Au substrate and hinder the ligand exchange process. It has been suggested earlier that the stronger affinity of homocysteine to fluorocarbon tail facilitates faster transport of homocysteine than cysteine, which is however, contradicted by the results of C18 column chromatography experiments [52] showing clearly faster elution of Cys than Hcys, consistent with stronger interactions of Hcys with a hydrophobic chain [24]. In addition to that, the shorter cysteine forms less strongly bound film of SAM on gold than longer homocysteine so in the adsorption competition, cysteine is a weaker competitor to the fluorosurfactant than homocysteine. In summary, there seem to be both thermodynamic as well as kinetic aspects of the ligand exchange between the thioaminoacids and the fluorosurfactant that lead under carefully selected conditions to a much higher effectiveness of homocysteine, in relation to that of cysteine, in replacing ZONYL from the gold nanoparticle protective shell.

The interactions of cysteine and homocysteine with citrate-capping film have also been considered. At the pH of measurements (pH 5–6), the citrate shell is charged negatively providing a long-term stability for the gold colloid, whereas both cysteine and homocysteine are in the form of zwitterions with protonated $-NH_3^+$ group and dissociated $-COO^-$ group. The main interaction of the electrostatic nature between $-COO^-$ group of the nanoparticle shell and $-NH_3^+$ group of the approaching thioaminoacid is expected with strong repulsions between dissociated carboxylate groups of the citrate and Cys or Hcys molecules. The results of molecular dynamics simulations and quantum mechanical calculations obtained are presented below.

In Fig. 11, the interactions of cysteine and homocysteine with citrate ions in a ligand exchange process are analyzed. It is seen that both Cys and Hcys form intermediate surface complexes on approaching to a citrate-capped gold nanoparticle. Within the framework of electrostatic

attractions between $COO^-$ group of the nanoparticle shell and $NH_3^+$ group of the thioaminoacid, a double hydrogen bond is formed for both the Cit-Cys and Cit-Hcys complexes. Immediately seen is, however, a completely different configuration of the thioaminoacid in the surface complex formed. Whereas a cysteine molecule forms a kind of axial (linear) configuration extending out of the citrate protective SAM, the homocysteine tends to bend out of the axial conformation and toward the citrate side-chain and the electrode surface. The lack of flexibility of the cysteine molecule has already been pointed out when comparing ring-forming abilities of these two molecules [32]. Here, the bending toward the citrates side chain results in the substantial difference in the distance of the thiol group to the gold surface. This distance is 0.75 nm for Cit-Cys surface complex and only 0.38 nm for Cit-Hcys complex. This difference can be translated to classifying the thioaminoacid position as being outside of the shell (in the case of cysteine) or inside the shell (in the case of homocysteine). The large difference in the observed light scattering intensity between Cys and Hcys can be explained by easier and faster penetration of Hcys into the citrate-dominated gold nanoparticle shell followed by citrate ligand replacement. After the ligand exchange has been completed, the zwitterion-type interactions begin to operate leading to the nanoparticle assembly and manifested by the sharp increase in the resonance elastic light scattering, as observed experimentally. On the other hand, in the case of cysteine, the ligand exchange process is strongly hindered by cysteine inability to enter the citrate protective shell due to the axial conformation of the surface complex Cit-Cys.

## 4. Conclusion

The results demonstrate clearly the differences between cysteine and homocysteine in their ability to ligand exchange with non-ionic

fluorosurfactant-capped AuNP, as well as with negatively charged citrate-capped AuNP. These intriguing differences appear as an amplification of a small structural difference in the molecular build-up (one methylene group), which progresses through several stages leading to the final sensitive detection in the gold nanoparticle assembly process. The selective stages include kinetic retardation due to interactions of the thioaminoacids with the fluorosurfactant chain or formation of charge-induced H-bonded complexes, as in the case of citrate-capped AuNP. Conformational differences in these surface complexes on one hand prevent cysteine from entering the citrate shell and on the other hand pull the homocysteine into the citrate film, thus shortening the distance between the thiol part of the biomarker and the Au surface and making it easier to form Au thiolate bond. We have observed for the first time the RELS characteristics for de-aggregation of citrate-capped gold nanoparticle ensembles followed by their conversion to citrate-linked Hcys-capped nanoparticle assemblies. The ligand exchange effects and gold nanoparticle assembly induced by thioaminoacid zwitterionic interparticle interactions are important in understanding physicochemical aspects of small biomolecule interactions with metal nanoparticles as the use of the latter is widely being explored for new nanomedical applications. The observed differences in the behavior of structurally similar cysteine and homocysteine have profound implications in their analytical determinations using rapid and inexpensive measurement techniques important for the oxidative stress screening and prevention of environmental pollution effects on human health.

## Acknowledgements

## References

[1] M. Noble, M. Mayer-Proschel, C. Proschel, Redox regulation of precursor cell function: insights and paradoxes, Antioxid. Redox Signal. 7 (2005) 1456–1467.
[2] D. Armstrong, Book oxidative stress biomarkers and antioxidant protocols, Humana Press, Totowa, NJ, 2002.
[3] M.D. Carlo, R.F. Loeser, Increased oxidative stress with aging reduces chondrocyte survival, Arthritis Rheum. 48 (2003) 3419–3430.
[4] S.J. James, S. Melnyk, S. Jernigan, M.A. Cleves, C.H. Halsted, D.J. Wong, P. Cutler, M. Boris, K. Bock, J.J. Bradstreet, S.B. Baker, D.W. Gaylor, Metabolic endophenotype and related genotypes are associated with oxidative stress in children with autism, Am. J. Med. Genet. 141B (2006) 947–956.
[5] Y. Yamamoto, S. Yamanashi, Ubiquinol/ubiquinone ratio as a marker of oxidative stress, in: D. Armstrong (Ed.), Oxidative Stress Biomarkers and Antioxidant Protocols, Humana Press, Totowa, NJ, 2002.
[6] W. Droge, Free radicals inthe physiologic control of cell function, Physiol. Rev. 82 (2002) 47–95.
[7] R. Carmel, D.W. Jacobsen, Book homocysteine in health and disease, Cambridge University Press, Cambridge, U.K., 2001.
[8] D.W. Jacobsen, Hyperhomocysteinemia and oxidative stress: time for a reality check? Arterioscler. Thromb. Vasc. Biol. 20 (2000) 1182–1184.
[9] H. Refsum, P.M. Ueland, O. Nygard, S.E. Volset, Homocysteine and cardiovascular disease, Annu. Rev. Med. 49 (1989) 31.
[10] X. Zhang, H. Li, H. Jin, Z. Ebin, S. Brodsky, M.S. Goligorsky, Effects of homocysteine on endothelialnitric oxide production, Am. J. Physiol. Renal Physiol. 279 (2000) F671.
[11] C. Boushey, S. Beresford, G. Omenn, A. Motulsky, A quantitative assessment of plasma homocysteine as a risk factor for vascular disease: probable benefits of increasing folic acid intake, JAMA 274 (1995) 1049.
[12] I.M. Graham, L. Daly, H. Refsum, K. Robinson, L. Brattstrom and P.M. Ueland, Plasma homocysteine as a risk factor for vascular disease: the European concerted action project, JAMA 277 (1997) 1775; 5482.
[13] S.R. Lentz, W.G. Haynes, Homocysteine: Is it a clinically important cardiovascular risk factor? Clevel. Clin. J. Med. 71 (2004) 729–734.
[14] G.N. Welch, J. Loscalzo, Homocysteine and atherothrombosis, N. Engl. J. Med. 338 (1998) 1042–1050.
[15] S. Seshadri, A. Beiser, J. Selhub, P.F. Jaques, I.H. Rosenberg, R.B. D'Agostino, P.W.F. Wilson, Plasma homocysteine as a risk factor for dementia and Alzheimer's disease, N. Engl. J. Med. 346 (2002) 476.
[16] S. Varadarajan, J. Kanski, M. Aksenova, C. Lauderback, D.A. Butterfield, Different mechanisms of oxidative stress and neurotoxicity for Alzheimer's Ab(1–42) and Ab(25–35), J. Am. Chem. Soc. 123 (2001) 5625.
[17] J.L. Mills, J.M. Scott, P.N. Kirke, J.M. McPartlin, M.R. Conley, D.G. Weir, A.M. Molloy, Y.J. Lee, Homocysteine and neural tube defects, J. Nutr. 126 (1996) S756.
[18] K.M. Beard, N. Shangari, B. Wu, P.J. O'Brien, Metabolism, not autoxidation, plays a role in α-oxoaldehyde- and reducing sugar-induced erythrocyte GSH depletion: Relevance for diabetes mellitus, Mol. Cell. Biochem. 252 (2003) 331–338.
[19] S. Bernard, A. Enayati, L. Redwood, H. Roger, T. Binstock, Autism: a novel form of mercury poisoning, Med. Hypotheses 56 (2001) 462–471.
[20] T. Clark-Taylor, Is autism a disorder of fatty acid metabolism? Possible dysfunction of mitochondrial β-oxidation by long chain acyl-CoA dehydrogenase, Med. Hypotheses 62 (2003) 970–975.
[21] C.V. Guldener, K. Robinson, Homocysteine and renal disease, Semin. Thromb. Hemost. 26 (2000) 313.
[22] B. Brown, Homocysteine: a risk factor for retinal venous occlusive desease, Am. Acad. Ophthalmol. 109 (2002) 287–290.
[23] M. Stobiecka, J. Deeb, M. Hepel, Molecularly-templated polymer matrix films for biorecognition processes: sensors for evaluating oxidative stress and redox buffering capacity, Electrochem. Soc. Trans. 19 (2009).
[24] W. Wang, O. Rusin, X. Xu, K. Kyu, K. Kim, J.O. Escobedo, S.O. Fakayode, K.A. Fletcher, M. Lowry, C.M. Schowalter, C.M. Lawrence, F.R. Fronczek, I.M. Warner, R.M. Strongin, Detection of homocysteine and cysteine, J. Am. Chem. Soc. 127 (2005) 15949–15958.
[25] J.O. Escobedo, O. Rusin, W. Wang, O. Alptürk, K.K. Kim, X. Xu, R.M. Strongin, Detection of biological thiols, Reviews in Fluorescence, Springer, US, 2006, pp. 139–162.
[26] F. Tanaka, N. Mase, C.F. Barbas III, Determination of cysteine concentration by fluorescence increase: reaction of cysteine with a fluorogenic aldehyde, Chem. Commun. 7 (2004) 1762–1763.
[27] E.J. Pacsial-Ong, R.L. McCarley, W. Wang, R.M. Strongin, Electrochemical detection of glutathione using redox indicators, Anal. Chem. 78 (2006) 7577–7581.
[28] L. Agüí, C. Peña-Farfal, P. Yáñez-Sedeño, J.M. Pingarrón, Electrochemical determination of homocysteine at a gold nanoparticle-modified electrode, Talanta 74 (2007) 412–420.
[29] I.I.S. Lim, W. Ip, E. Crew, P.N. Njoki, D. Mott, C.J. Zhong, Y. Pan, S. Zhou, Homocysteine-mediated reactivity and assembly of gold nanoparticles, Langmuir 23 (2007) 826–833.
[30] A.T. Gates, S.O. Fakayode, M. Lowry, G.M. Ganea, A. Marugeshu, J.W. Robinson, R.M. Strongin, I.M. Warner, Gold nanoparticle sensor for homocysteine thiolactone-induced protein modification, Langmuir 24 (2008) 4107–4113.
[31] P.K. Sudeep, S.T.S. Joseph, K.G. Thomas, Selective detection of cysteine and glutathione using gold nanorods, J. Am. Chem. Soc. 127 (2005) 6516–6517.
[32] H.P. Wu, C.C. Huang, T.L. Cheng, W.L. Tseng, Sodium hydroxide as pretreatment and fluorosurfactant-capped gold nanoparticles as sensor for the highly selective detection of cysteine, Talanta 76 (2008) 347–352.
[33] M. Wasowicz, S. Viswanathan, A. Dvornyk, K. Grzelak, B. Kludkiewicz, H. Radecka, Comparison of electrochemical immunosensors based on gold nanomaterials and immunoblot techniques for detection of histidine-tagged proteins in culture medium, Biosens. Bioelectron. 24 (2008) 284–289.
[34] M. Hepel, J. Dallas, M.D. Noble, Interactions and reactivity of Hg(II) on glutathione modified gold electrode studied by EQCN technique, J. Electroanal. Chem. 622 (2008) 173–183.
[35] M. Hepel, E. Tewksbury, Ion-gating phenomena of self-assembling glutathione films on gold piezoelectrodes, J. Electroanal. Chem. 552 (2003) 291–305.
[36] M. Hepel, E. Tewksbury, Nanogravimetric study of templated copper deposition in ion-channels of self-assembled glutathione films on gold piezoelectrodes, Electrochim. Acta 49 (2004) 3827–3840.
[37] S.I. Lim, C.J. Zhong, Molelucarly mediated processing and assembly of nanoparticles: exploring the interparticle interactions and structures, Acc. Chem. Res. 42 (2009) 798–808.
[38] N.N. Kariuki, J. Luo, L. Han, M.M. Maye, L. Moussa, M. Patterson, U. Lin, M.H. Engelhard, C.J. Zhong, Nanoparticle-structured ligand framework as electrode interfaces, Electroanalysis 16 (2004) 120–126.
[39] I.I.S. Lim, C.J. Zhong, Molecularly-Mediated Assembly of Gold Nanoparticles, Gold Bulletin 40/1 (2007) 59–66.
[40] S. Zhang, X. Kou, Z. Yang, Q. Shi, G.D. Stucky, L. Sun, J. Wang, C. Yan, Nanoneckles assembled from gold rods, spheres, and bipyramids, Chem. Commun. (2007) 1816–1818.
[41] L. Han, J. Luo, N. Kariuki, M.M. Maye, V.W. Jones, C.J. Zhong, Novel interparticle spatial properties of hydrogen-bonding mediated nanoparticle assembly, Chem. Mater. 15 (2003) 29–37.
[42] W. Zheng, M.M. Maye, F.L. Leibowitz, C.J. Zhong, Imparting biomimetic ion-gating recognition properties to electrodes with a hydrogen-bonding structured core-shell nanopartricle network, Anal. Chem. 72 (2000) 2190–2199.
[43] I.I.S. Lim, D. Mott, W. Ip, P.N. Njoki, Y. Pan, S. Zhou, C.J. Zhong, Interparticle interactions of glutathione mediated assembly of gold nanoparticles, Langmuir 24 (2008) 8857–8863.
[44] Z.P. Li, X.R. Duan, C.H. Liu, B.A. Du, Selective determination of cysteine by resonance light scattering technique based on self-assembly of gold nanoparticles, Anal. Biochem. 351 (2006) 18–25.
[45] O. Rusin, N.N.S. Luce, R.A. Agbaria, J.O. Escobedo, S. Jiang, I.M. Warner, F.B. Dawan, K. Lian, R.M. Strongin, Visual detection of cysteine and homocysteine, J. Am. Chem. Soc. 126 (2004) 438–439.
[46] F.X. Zhang, L. Han, L.B. Israel, J.G. Daras, M.M. Maye, N.K. Ly, C.J. Zhong, Colorimetric detection of thiol-containing amino acids using gold nanoparticles, Analyst 127 (2002) 462–465.
[47] C. Lu, Y. Zu, V.W.W. Yam, Nonionic surfactant-capped gold nanoparticles as postcolumn reagents for high-performance liquid chromatography assay of low-molecular-mass biothiols, J. Chromatogr. A 1163 (2007) 328–332.

[48] A. Mocanu, I. Cernica, G. Tomoaia, L.D. Bobos, O. Horovitz, M. Tomoaia-Cotisel, Self-assembly characteristics of gold nanoparticles in the presence of cysteine, Colloids Surf. A 338 (2009) 93–101.

[49] W. Wang, J.O. Escobedo, C.M. Lawrence, R.M. Strongin, Direct detection of homocysteine, J. Am. Chem. Soc. 126 (2004) 3400–3401.

[50] M.J. Hostetler, A.C. Templeton, R.W. Murray, Dynamics of place-exchange reactions on monolayer-protected gold cluster molecules, Langmuir 15 (1999) 3782–3789.

[51] M.J. Hostetler, J.E. Wingate, C.J. Zhong, J.E. Harris, R.W. Vachet, M.R. Clark, J.D. Londono, S.J. Green, J.J. Stokes, G.D. Wignall, J.L. Glish, M.D. Porter, N.D. Evans, R.W. Murray, Alkanethiolate gold cluster molecules with core diameters from 1.5 to 5.2 nm: core and monolayer properties as a function of core size, Langmuir 14 (1998) 17–30.

[52] C. Lu, Y. Zu, V.W.W. Yam, Specific postcolumn detection method for HPLC assay of homocysteine based on aggregation of fluorosurfactant-capped gold nanoparticles, Anal. Chem. 79 (2007) 666–672.

[53] C.C. Huang, W.L. Tseng, Role of fluorosurfactant-modified gold nanoparticles in selective detection of homocysteine thiolactone: remover and sensor, Anal. Chem. 80 (2008) 6345–6350.

[54] C.J. Ackerson, M.T. Sykes, R.D. Kornberg, Liagnd exchange between GSH and thiolated oligonucleotides on AuNP, Proc. Natl. Acad. Sci. U.S.A. 102 (2005) 13383.

[55] B.T. Draine, P.J. Flatau, Discrete-dipole approximation for scattering calculations, J. Opt. Soc. Am. A 11 (1994) 1491–1499.

[56] W.H. Yang, G.C. Schatz, R.R.v. Duyne, Discrete dipole approximation for calculating extinction and Raman intensities for small particles with arbitrary shapes, J. Chem. Phys. 103 (1995) 869–875.

[57] A. Brioude, X.C. Jiang, M.P. Pileni, Optical properties of gold nanorods: DDA simulations supported by experiments, J. Phys. Chem. B 109 (2005) 13138–13142.

[58] K.S. Lee, M.A. El-Sayed, Dependence of the enhanced optical scattering efficiency relative to that of absorption for gold metal nanorods on aspect ratio, size, end-cap shape, and medium refractive index, J. Phys. Chem. B 109 (2005) 20331.

[59] P.K. Jain, K.S. Lee, I.H. El-Sayed, M.A. El-Sayed, Calculated absorption and scattering properties of gold nanoparticles of different size, shape, and composition: applications in biological imaging and biomedicine, J. Phys. Chem. B 110 (2006) 7238.

[60] E.S. Kooij, B. Poelsema, Shape and size effects in the optical properties of metallic nanorods, Phys. Chem. Chem. Phys. 8 (2006) 3349–3357.

[61] K.S. Lee, M.A. El-Sayed, Gold and silver nanoparticles in sensing and imaging: sensitivity of plasmon response to size, shape, and metal composition, J. Phys. Chem. B 110 (2006) 19220.

[62] S.W. Prescott, P. Mulvaney, Gold nanorod extinction spectra, J. Appl. Phys. 99 (2006) 123504.

[63] G. Yin, S.Y. Wang, M. Xu, L.Y. Chen, discrete dipole approximation — size and shape, J. Korean Phys. Soc. 49 (2006) 2108.

[64] A.L. Gonzales, C. Noguez, Influence of morphology on the optical properties of metal nanoparticles, J. Comput. Theor. Nanosci. 4 (2007) 231.

[65] C. Ungureanu, R.G. Rayavarapu, S. Manohar, T.G.v. Leeuwen, Discrete dipole approximation simulations of gold nanorod optical properties: choice of input parameters and comparison with experiment, J. Appl. Phys. 105 (2009) 102032.

[66] P.B. Johnson, R.W. Christy, Optical constants of the noble metals, Phys. Rev. B 6 (1972) 4370.

[67] M.M. Alvarez, J.T. Khoury, T.G. Schaaff, M.N. Shafigullin, I. Vezmar, R.L. Whetten, Optical absorption spectra of nanocrystal gold molecules, J. Phys. Chem. B 101 (1997) 3706–3712.

[68] S. Link, M.A. El-Sayed, Spectral properties and relaxation dynamics of surface plasmon electronic oscillations in gold and silver nanodots and nanorods, J. Phys. Chem. B 103 (1999) 8410–8426.

[69] S. Link, M.B. Mohamed, M.A. El-Sayed, Simulation of the optical absorption spectra of gold nanorods as a function of their aspect ratio and the medium dielectric constant, J. Phys. Chem. B 103 (1999) 3073–3077.

[70] P.V. Kamat, Photophysical, photochemical and photocatalytic aspects of metal nanoparticles, J. Phys. Chem. B 106 (2002) 7729–7744.

[71] M. Mishchenko, L. Travis, A. Lacis, Scattering, absorption, and emission of light by small particles, Cambridge University Press, Cambridge, 2002.

[72] J. Perez-Juste, I. Pastoriza-Santos, L.M. Liz-Marzan, P. Mulvaney, Gold nanorods: Synthesis, characterization and applications, Coord. Chem. Rev. 249 (2005) 1870–1901.

[73] P.G. Etchegoin, E.C.l. Ru, M. Meyer, An analytic model for the optical properties of gold, J. Chem. Phys. 125 (2006) 164705-1–164705-3.

[74] Y. Ping, D. Hanson, I. Koslov, T. Ogitsu, O. Prendergast, E. Schwegler, G. Collins, A. Ng, Dielectric function of warm dense gold, Phys. Plasmas 15 (2008) 056303.

[75] R.F. Pasternack, C. Bustamante, P.J. Collings, A. Giannetto, E.J. Gibbs, Porphyrin assemblies on DNA as studied by a resonance light-scattering technique, J. Am. Chem. Soc. 115 (1993) 5393–5399.

[76] R.F. Pasternack, Resonance light scattering: a new technique for studying chromophore aggregation, Science 269 (1995) 935.

[77] C.Z. Huang, K.A. Li, S.Y. Tong, Determination of nanogram of nucleic acids by their enhancement effect on the resonance light scattering of the cobalt(II)/4-[(5-chloro-2-pyridyl)azo]-1, 3-diaminobenzene complex, Anal. Chem. 69 (1997) 514–520.

[78] C.Z. Huang, K.A. Li, S.Y. Tong, Determination of nucleic acids by a resonance light-scattering technique with a, b, c, d-tetrakis[4-(trimethylammoniumyl)phenyl] porphine, Anal. Chem. 68 (1996) 2259–2263.

[79] Z.X. Guo, H.X. Shen, Sensitive and simple determination of protein by resonance Rayleigh scattering with 4-azochromotropic acid phenylfluorone, Anal. Chim. Acta 408 (2000) 177–182.

[80] Y.T. Wang, F.L. Zhao, K.A. Li, S.Y. Tong, Molecular spectroscopic study of DNA binding with neutral red and application to assay of nucleic acids, Anal. Chim. Acta 396 (1999) 75–81.

[81] C.Z. Huang, Y.F. Li, X.D. Liu, Determination of nucleic acids at nanogram levels with safranine T by a resonance light-scattering technique, Anal. Chim. Acta 375 (1998) 89–97.

[82] Y. Liu, C.Q. Ma, K.A. Li, F.C. Xie, S.Y. Tong, Rayleigh light scattering study on the reaction of nucleic acids and methyl violet, Anal. Biochem. 268 (1999) 187–192.

[83] X. Wu, Y. Wang, M. Wang, S. Sun, J. Yang, Y. Luan, Determination of nucleic acids at nanogram level using resonance light scattering technique with Congo Red, Spectrochim. Acta A 61 (2005) 361–366.

[84] Z. Jia, J. Yang, X. Wu, C. Sun, S. Liu, F. Wang, Z. Zhao, The sensitive determination of nucleic acids using resonance light scattering quenching method, Spectrochim. Acta A 64 (2006) 555–559.

[85] D.E. Aspnes, Effective medium theory, Am. J. Phys. 50 (1982) 704.

[86] K.L. Kelly, E. Coronado, L.L. Zhao, G.C. Schatz, The optical properties of metal nanoparticles: the influence of size, shape, and dielectric environment, J. Phys. Chem. B 107 (2003) 668–677.

[87] J. Nappa, G. Revillod, J.P. Abid, I. Russier-Antoine, C. Jonin, E. Benichou, H.H. Girault, P.F. Brevet, Hyper-Rayleigh scattering of gold nanorods and their relationship with linear assemblies of gold nanospheres, Faraday Discuss. 125 (2004) 145–156.

[88] J. Turkevich, P.C. Stevenson, J. Hiller, synthesis of AuNP, Discuss. Faraday Soc. 11 (1951) 55–75.

[89] W.J. Hehre, L. Radon, P.R. Schleyer, J.A. Pople, Ab-initio molecular orbital theory, Wiley, New York, 1985.

[90] P.W. Atkins, R.S. Friedman, Molecular quantum mechanics, Oxford University Press, Oxford, 2004.

[91] F. Li, Y. Zu, Effect of nonionic fluorosurfactant on the electrogenerated chemiluminescence of the Tris (2, 2′-bipyridine)ruthenium(II)/Tri-n-propylamine system: lower oxidation potential and higher emission intensity, Anal. Chem. 76 (2004) 1768–1772.

[92] R. Elghanian, J.J. Storhoff, R.C. Mucic, R.L. Letsinger, C.A. Mirkin, Selective colorimetric detection of polynucleotides based on the distance-dependent optical properties of gold nanoparticles, Science 277 (1997) 1078–1081.

[93] A.P. Alivisatos, K.P. Johnsson, X. Peng, T.E. Wilson, C.J. Loweth, M.P. Bruchez, P.G. Schultz, attachment of oligonucleotides to thiol-coated AuNP, Nature 382 (1996) 610.

[94] M.M. Maye, I.I.S. Lim, J. Luo, Z. Rab, D. Rabinovich, T. Liu, C.J. Zhong, Mediator-template assembly of nanoparticles, J. Am. Chem. Soc. 127 (2005) 1519–1529.

[95] S.J. Park, T.A. Taton, C.A. Mirkin, Array-based electrical detection of DNA with nanoparticle probes, Science 295 (2002) 1503–1505.

[96] R.A. Reynolds, C.A. Mirkin, R.L. Letsinger, Homogeneous, nanoparticle-based quantitative colorimetric detection of oligonucleotides, J. Am. Chem. Soc. 122 (2000) 3795–3796.

[97] J.J. Storhoff, R. Elghanian, R.C. Mucic, C.A. Mirkin, R.L. Letsinger, One-pot colorimetric differentiation of polynucleotides with single base imperfections using gold nanoparticle probes, J. Am. Chem. Soc. 120 (1998) 1959–1964.

[98] T.A. Taton, G. Lu, C.A. Mirkin, Two-color labeling of oligonucleotide arrays via size-selective scattering of nanoparticle probes, J. Am. Chem. Soc. 123 (2001) 5164–5165.

[99] T.A. Taton, R.C. Mucic, C.A. Mirkin, R.L. Letsinger, The DNA-mediated formation of supramolecular mono- and multilayered nanoparticle structures, J. Am. Chem. Soc. 122 (2000) 6305–6306.

# Resonance elastic light scattering (RELS) spectroscopy of fast non-Langmuirian ligand-exchange in glutathione-induced gold nanoparticle assembly

Magdalena Stobiecka, Kaitlin Coopersmith, Maria Hepel *

Department of Chemistry, State University of New York at Potsdam, Potsdam, NY 13676, USA

## ABSTRACT

The interactions of a biomolecule glutathione (GSH) with citrate-capped gold nanoparticles (AuNP) have been investigated to evaluate the viability of a rapid GSH-capture by gold nanoparticle carriers, as a model system for applications ranging from designing nanoparticle-enhanced functional biosensor interfaces to nanomedicine. The measurements, performed using resonance elastic light scattering (RELS) spectroscopy, have shown a strong dependence of GSH-induced scattering cross-section on gold nanoparticle size. A large increase in RELS intensity after injection of GSH, in a short reaction time ($\tau$ = 60 s), has been observed for small AuNP (5 nm dia.) and ascribed to the fast ligand-exchange followed by AuNP assembly. The unexpected non-Langmuirian concentration dependence of scattering intensity for $AuNP_{5nm}$ indicates on a 2D nucleation and growth mechanism of the ligand-exchange process. The ligand-exchange and small nanoparticle ensemble formation followed by relaxation have been observed in long term (10 h) monitoring of GSH–AuNP interactions by RELS. The results of molecular dynamics and quantum mechanical calculations corroborate the mechanism of the formation of hydrogen-bonded GSH-linkages and interparticle interactions and show that the assembly is driven by multiple H-bonding between GSH-capped AuNP and electrostatic zwitterionic interactions. The RELS spectroscopy has been found as a very sensitive tool for studying interparticle interactions. The application of RELS can be expanded to monitor reactivities and assembly of other monolayer-protected metal clusters, especially in very fast processes which cannot be followed by other techniques.

© 2010 Elsevier Inc. All rights reserved.

## 1. Introduction

The gold nanoparticles (AuNP) have recently gained outstanding interests owing to their size and shape dependent plasmonic optical properties [1–6], ease of functionalization [7–12], and the ability to penetrate the cell membranes. Numerous prospective applications of AuNP relate to the detection of biomolecules [13–16], including DNA strands [17–25], the design of photonic and bioelectronic devices, and the nanomedicine [26–29]. In the latter field, AuNP benefit medical diagnostics, cancer therapy, and contribute to imaging enhancements. The potential application of AuNP in cancer treatment involves targeted drug delivery and photodynamic therapy (PDT). The nanoparticles concentrated in a tumor tissue can deliver chemotherapeutic agents to kill the cancer cells or act as the light scatterers for PDT. In both cases, the specific reactivities of AuNP with biomolecules have to be taken into account. Since the propensity of AuNP to strongly interact with thiol species is one of the most pronounced properties of AuNP, the potential interactions of AuNP with the natural body thiols such

as the glutathione (GSH), cysteine (Cys), and homocysteine (Hcys), are of the utmost importance. Therefore, studies of the interactions of functionalized AuNP with GSH and other biomolecules are important not only to elucidate mechanistic issues and describe new phenomena encountered in these systems but also to further the understanding of effects occurring in real tissue environment and to improve the practical therapeutic outcomes.

Glutathione, which adsorbs readily on gold surfaces [10,11,30–32] is a tripeptide (glutamate–cysteine–glycine) with sulfhydryl group able to form a strong Au–S bond. Different kinds of interparticle interactions between GSH, cysteine and homocysteine have been recently discussed by Maye et al. [33]. Such molecules as homocysteine [34,35], glutathione (GSH) [35–37], and aminoacids [35,38–40] have been found to influence the spectral surface-plasmon (SP) characteristics. Previously, we have investigated the interactions and electrochemical reactivity of Hg(II) on GSH-modified gold piezoelectrodes [10,11,41]. The GSH-SAM permeability to ionic species has been demonstrated for Hg(II) [10,11], Pb(II) [30], Ni(II) [30], and Cu(II) [31] using metal adatom probe, nanogravimetry and chronoamperometry. Gooding and co-workers [42] studied GSH bonded to mercaptopropionic acid as the sensor for Cd(II). The interactions of adsorbed GSH with $Cu^{2+}$ have also been studied [31,32]. It has been shown that GSH-SAM's formed

* Corresponding author. Fax: +1 315 267 3170.
E-mail address: hepelmr@potsdam.edu (M. Hepel).

on Au piezoelectrodes can act as chemically controlled ion gates [30,43–46] and as templates for metal depositions [31].

In living organism's homeostasis, GSH and its oxidized disulfide form (GSSG) constitute the main redox regulation system. It protects cells against organic peroxides and damaging radicals, and is involved in signaling processes associated with cell apoptosis. The diminished active GSH levels in cells and body fluids lead to the reduced antioxidation capacity [47] to protecting against radicals and have been found to increase susceptibility to autism [48,49], diabetes [50], and other diseases [47,49–55]. The low GSH levels have been found to be caused by oxidative stress and exposure to toxic heavy metals (Hg, Cd, Pb). GSH and phytochelatines with general structure ($\gamma$-Glu-Cys)$_n$Gly participate as the capping agents [56,57] in heavy-metal sulfide nanoparticles formed in living organisms in natural detoxification processes [58–61].

The glutathione-mediated gold nanoparticle assembly has been studied by Sudeep et al. [36] and by Zhong and co-workers [37] and strong effects of pH and electrolyte concentration have been found. A model based on two-point zwitterionic interparticle interactions has been proposed [62]. Directional growth of GSH-linked gold nanorod assemblies has been observed by Kou et al. [63] whereas the competitive adsorption of GSH and thiolated oligonucleotides has been investigated by Ackerson et al. [64]. Recently, GSH has been found to participate in the degradation of Pt(II)-based DNA intercalators utilized in chemotherapy.

In this work, we have investigated interactions of glutathione with gold nanoparticles and explored the utility of the resonance elastic light scattering (RELS) spectroscopy to monitor GSH-induced AuNP assembly. This technique has been developed [65–70] as a sensitive technique for the detection of bioorganic complexes. The resonance elastic light scattering from molecules and nanoparticles in solution results from the absorption of photons followed by an immediate coherent re-emission of light in all directions without any energy loss [70]. We have recently applied RELS to study nanoparticle assembly [71] and found it to be very sensitive to supramolecular ensemble formation in the system homocysteine-citrate-fluorosurfactant-AuNP. In this paper, we describe new phenomena associated with the interactions of GSH with AuNP and elucidate the mechanism of the multi-step process leading to the assembly of GSH-capped AuNP networks. For the model system based on high concentration levels of GSH and short time-scale AuNP assembly, an unexpected non-Langmuirian ligand-exchange kinetics has been found. Details of the experiments and implications of this finding are discussed.

## 2. Materials and methods

### 2.1. Chemicals

All chemicals used for investigations were of analytical grade purity. L-glutathione reduced (GSH), minimum 99%, glutathione oxidized form (GSSG), tetrachloroauric(III) acid trihydrate (HAuCl$_4$·3H$_2$O), 99.9+% metals basis, were purchased from Sigma Aldrich Chemical Company (Atlanta, GA, USA) and used as received. Sodium citrate dihydrate was obtained from J.T. Baker Chemical Co. (Phillipsburg, NJ, USA). Sodium borohydride (NaBH$_4$) was obtained from Fisher Scientific Company. Solutions were prepared using Millipore (Billerica, MA, USA) Milli-Q deionized water (conductivity $\sigma$ = 55 nS/cm). They were deoxygenated by bubbling with purified argon.

### 2.2. Apparatus

The imaging analyses of Au nanoparticles were performed using high-resolution transmission electron microscopy (HR-TEM) with

Model JEM-2010 (Jeol, West Chester, PA, USA) instrument (200 kV). The elastic light scattering spectra were recorded using LS55 Spectrometer (Perkin Elmer, Waltham, MA, USA) equipped with 20 kW Xenon light source operating in 8 μs pulsing mode allowing for the use of monochromatic radiation with wavelength from 200 nm to 800 nm with 1 nm resolution and sharp cut-off filters: 290, 350, 390, 430, 515 nm. The dual detector system consisted of a photomultiplier tube (PMT) and an avalanche photodiode. Pulse width at half height was less than 10 μs. The UV–Vis spectra were recorded using Perkin Elmer Lambda 50 Spectrophotometer in the range 220–1100 nm or Ocean Optics (Dunedin, FL, USA) Model R4000 Precision Spectrometer in the range from 340 nm to 900 nm.

### 2.3. Procedures

The Au nanoparticles were synthesized according to the published procedure [72]. Briefly, to obtain 5 nm AuNP, a solution of HAuCl$_4$ (10 mM, 2.56 mL) was mixed with a trisodium citrate solution (10 mM, 9.6 mL), ratio 1:3.75, and poured to distilled water (88 mL). The obtained solution was vigorously stirred and fresh cold NaBH$_4$ solution (5 mM, 8.9 mL) was added dropwise. Larger AuNP (22.5 nm dia.) were obtained by mixing 10 mL of HAuCl$_4$ (10 mM stock solution) with 4 mL of Na$_3$Cit (38.75 mM) and 86 mL of water. The obtained solution was vigorously stirred and fresh cold NaBH$_4$ solution (5 mM, 8.9 mL) was added dropwise. The solution slowly turned light gray and then ruby red. Stirring was maintained for 30 min. The obtained citrate-capped core–shell Au nanoparticles were stored at 4 °C. Their size was first estimated from UV–Vis surface plasmon absorption band shift and determined more precisely by HR-TEM imaging to be: 5.0 ± 0.9 nm ($n$ = 85) and 22.5 ± 2.6 nm ($n$ = 40); these nanoparticles are denoted as AuNP$_{5nm}$ and AuNP$_{22nm}$, respectively. No larger particle population was present. The concentrations of AuNP are given in moles of particles per 1 L of solution (usually, in the nM range). The size and distribution of AuNP were also tested using plasmonic absorbance spectra in UV–Vis. For instance, a clear surface plasmon band with $\lambda_{max}$ = 516 nm for AuNP$_{5nm}$ and a low background beyond that wavelength indicate that no larger particles were present. This was also confirmed by TEM. The pH of AuNP solutions was maintained a citrate buffer (0.46 mM) at pH = 5 for storing and adjusted to 3.24 ± 0.03 before the experiments.

The glutathione stock solutions in water (10 mM) were protected from light and stored at 4 °C. The interactions of GSH with AuNP were monitored by UV–Vis absorption and resonant elastic light scattering (RELS).

Quantum mechanical calculations of electronic structure for Cit and GSH adsorbed on small gold-atom clusters Au$_n$ were performed using modified Hartree–Fock methods [73,74] with 6-311G$^*$ basis set and pseudopotentials, semi-empirical PM3 method, and density functional theory (DFT) with B3LYP functional and 6-311G$^*$ basis set, embedded in Wavefunction Spartan 6 [74]. The electron density and local density of states (LDOS) are expressed in atomic units, au$^{-3}$, where 1 au = 0.529157 Å and 1 au$^{-3}$ = 6.749108 Å$^{-3}$.

## 3. Results and discussion

### 3.1. Effect of GSH on resonance elastic light scattering of AuNP nanoparticles

Typical RELS spectrum for a citrate-capped AuNP$_{5nm}$ solution is presented in Fig. 1a, curve 1, for a constant excitation wavelength $\lambda_{ex}$ = 640 nm (1.94 eV). The scattering intensity peak with a Gaussian peak shape centered at $\lambda_{em} = \lambda_{ex}$ = 640 nm and with a narrow linewidth of $\Delta\lambda$ = 14 nm confirms that the effects due to radiation broadening, density fluctuation, fluorescence, and inelastic Raman
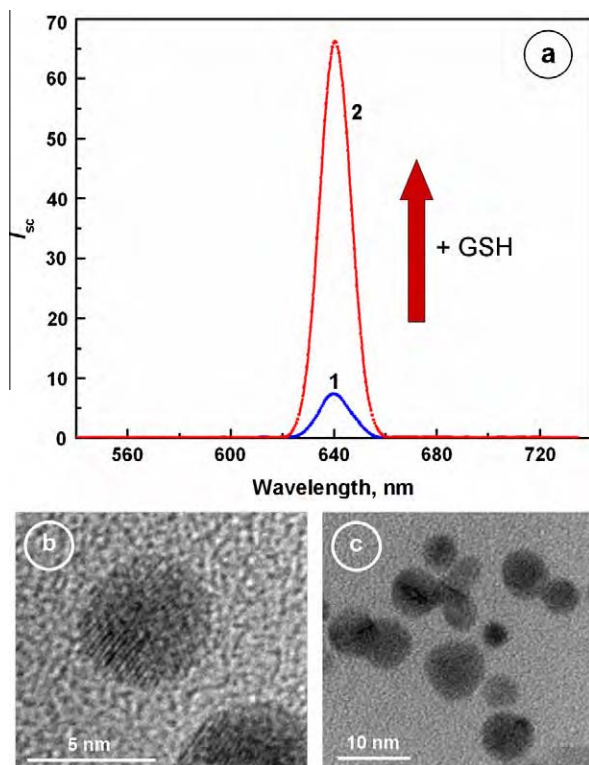
**Fig. 1.** Upper panel: (a) light scattering spectra for 10.1 nM AuNP$_{5nm}$ in the absence (1) and in the presence (2) of 5 mM glutathione, recorded for the incident beam wavelength $\lambda_{ex} = 640$ nm (spectra recorded within 1 min of glutathione injection). Lower panel: (b) high-resolution TEM image of AuNP$_{5nm}$; atomic rows with distance 0.24 nm are seen; (c) HR-TEM image of small GSH-linked AuNP$_{5nm}$ assemblies.

scattering are negligible. The background intensity is very low (virtually zero) providing excellent conditions for a sensitive analysis with well defined RELS peaks.

In the presence of GSH, the light scattering from AuNP$_{5nm}$ nanoparticles is strongly enhanced (Fig. 1a, curve 2). The solution pH was 3.24 ± 0.03 which is within the range of predominantly neutral (zwitterionic) form of GSH (pH = 2.04–3.4; p$K_a$ values for GSH are: p$K_1$ = 2.04 (glutamate –COOH), p$K_2$ = 3.4 (glycine –COOH), p$K_3$ = 8.72 (–SH group), p$K_4$ = 9.49 (–NH$_2$ group)). Note that surface p$K_a$ values may shift for surface-confined GSH similar to other molecules with pH-sensitive pendant groups ([75–81]), hence, these values are used only as guidelines. However, the strong RELS increase in pH range close to 3.2 confirms that zwitterionic form of GSH is in relative predominance in the AuNP shells, otherwise the assembly and strong scattering would not be observed. The enhancement of RELS from AuNP$_{5nm}$ by GSH molecules is attributed to the size increase of AuNP due to the ligand exchange (i.e. replacing short-chain citrate molecules in the nanoparticle shell with longer-chain GSH molecules) and/or interparticle interactions leading to AuNP assembly. The strong sixth-power dependence of elastic scattering intensity $I_{sc}$ on the nanoparticle diameter $a$ follows from the Rayleigh equation for light scattering from small particles:

$$I_{sc} = I_0 N \frac{(1 + \cos^2 \theta)}{2R^2} \left(\frac{2\pi}{\lambda}\right)^4 \left(\frac{\left((n_p - n_s)^2 - 1\right)}{\left((n_p - n_s)^2 + 2\right)}\right) \left(\frac{a}{2}\right)^6 \qquad (1)$$

where $n_p$ and $n_s$ are the refractive indices for the particles and the solution, respectively, $\lambda$ is the wavelength of incident light beam, $\theta$ is the scattering angle, $N$ is the number of particles, and $I_0$ is the constant. Taking into account the decrease in particle concentration

due to assembly and assuming $\lambda =$ const and other experimental conditions ($\theta$, $R$, $I_0$) unchanged, the increase of the effective particle diameter $a_{rel}$ can be estimated using the formula [71]:
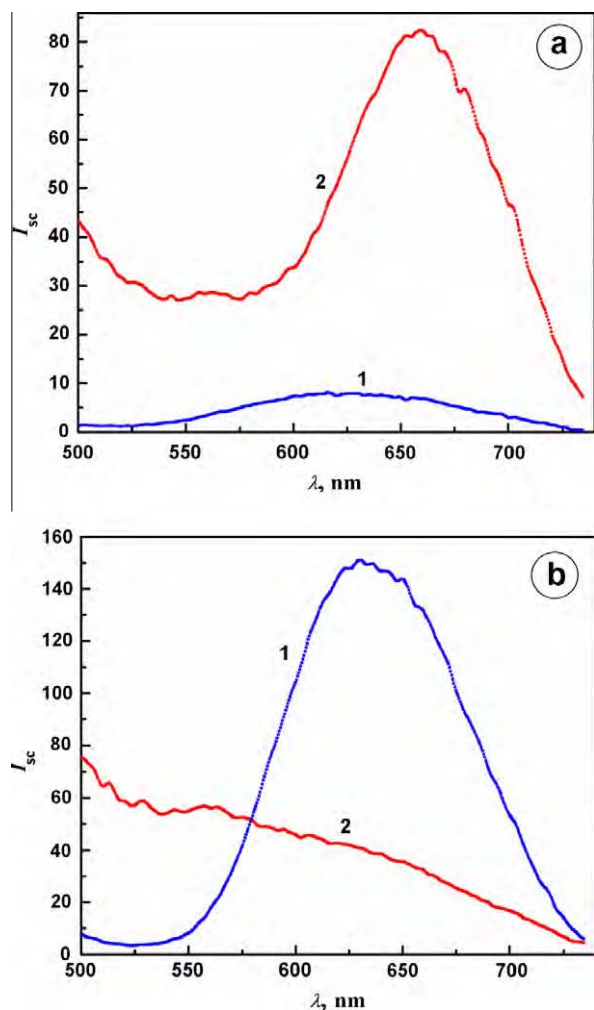
$$a_{rel} = \frac{a_1}{a_0} = \sqrt[3]{\frac{I_{sc,1}}{I_{sc,0}}} \qquad (2)$$

where indices 0 and 1 stand for the particles before and after GSH addition, respectively. From the data of Fig. 1a, the scattering intensity increase is: $I_{sc,1}/I_{sc,0} = 9.09$ and, hence, $a_{rel} = 2.09$. This means that most likely small aggregates composed of only few nanoparticles (e.g. 2–6) are formed. Similar experiments performed with larger Au nanoparticles show a completely opposite effect of GSH addition. In Fig. 2a, the RELS spectrum for a solution of AuNP$_{22nm}$ ($C_{AuNP} = 1.42$ nM) is shown in the absence of GSH (curve 1) and in the presence of 5 mM GSH (curve 2). Now, the addition of GSH to the Au nanoparticles, unexpectedly, results in a strong quenching of the Rayleigh scattering. To elucidate these differences in the behavior of AuNP$_{5nm}$ and AuNP$_{22nm}$, further investigations of full-scan RELS spectroscopy, long-term scattering evolution, and UV–Vis plasmonic spectroscopy have been carried out.

The full-scan RELS spectra for small and large AuNP are presented in Fig. 3. For small AuNP$_{5nm}$ nanoparticles, a dramatic increase of the resonant scattering intensity in the entire photon energy range scanned is observed. The $I_{sc}$ maximum for AuNP$_{5nm}$ alone is at $\lambda_{max} = 625$ nm. The broad RELS peak generated by the interactions of GSH with AuNP$_{5nm}$ is shifted to longer wavelengths and appears at $\lambda_{max} = 655$ nm. Similar RELS spectra for larger nanoparticles (AuNP$_{22nm}$), presented in Fig. 3b, show that the $I_{sc}$ maximum for AuNP$_{22nm}$ alone is larger than that for AuNP$_{5nm}$ alone, consistent with stronger scattering for larger particles. How-
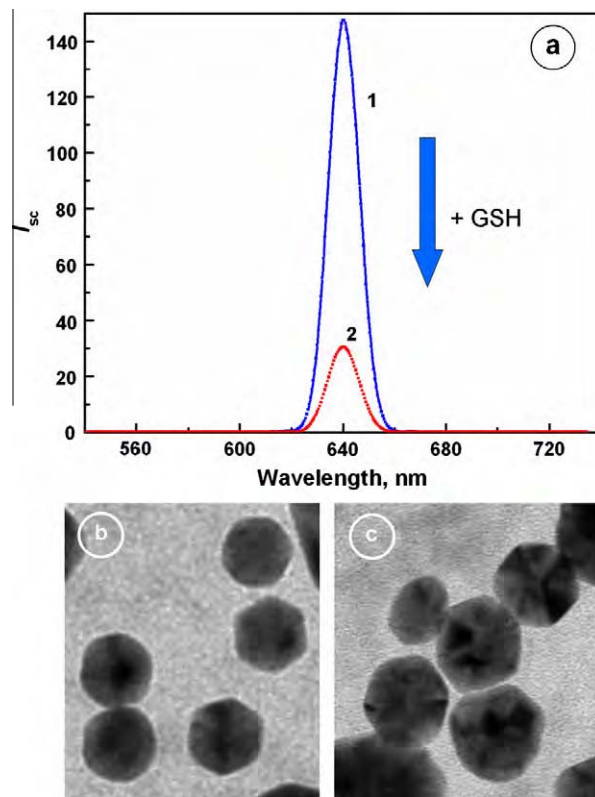


**Fig. 2.** Upper panel: (a) light scattering spectra for 1.42 nM AuNP$_{22nm}$, in the absence (1) and in the presence (2) of 5 mM glutathione (spectra recorded within 1 min of glutathione injection); incident beam wavelength: $\lambda_{ex} = 640$ nm. Lower panel: HR-TEM images of AuNP$_{22nm}$ before (b) and after (c) addition of 5 mM GSH.
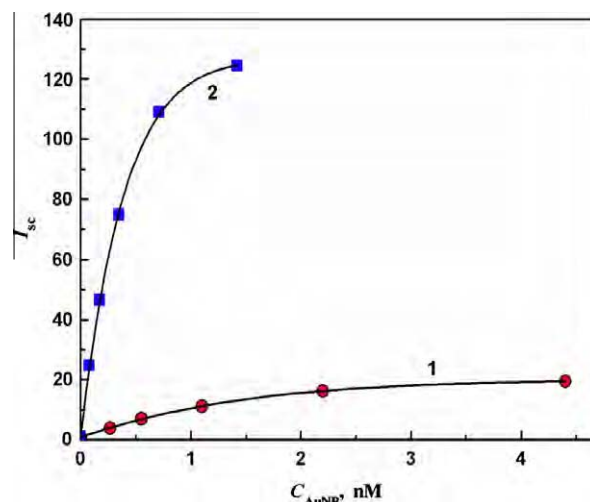
Fig. 4. Resonance elastic light scattering intensity $I_{sc}$ on concentration of gold nanoparticles $C_{AuNP}$ for: (1) $AuNP_{5nm}$ and (2) $AuNP_{22nm}$; incident beam wavelength: $\lambda_{ex} = 640$ nm.



Fig. 3. RELS spectra $I_{sc}$ vs. $\lambda$ for: (a) small nanoparticles ($AuNP_{5nm}$) and (b) larger nanoparticles ($AuNP_{22nm}$) in the absence of GSH (1) and in the presence of 5 mM GSH (2), recorded within 1 min of GSH injection.



Fig. 5. (a) Elastic light scattering spectra for 10.1 nM $AuNP_{5nm}$ for different concentrations of GSH, recorded within 1 min of GSH injection, $C_{GSH}$ [mM]: (1) 0, (2) 2.67, (3) 3.0, (4) 3.17, (5) 3.33, (6) 5; (b) experimental dependence of $I_{sc}$ vs. $C_{GSH}$ (curve 1, points) fitted with Boltzmann threshold function (line) and (2–5): calculated curves for a hypothetical pseudo-first-order Langmuirian kinetics showing the absence of threshold characteristics in Langmuirian model, $k$ [$M^{-1}s^{-1}$]: (2) 40, (3) 17, (4) 4, (5) 0.8; $\tau = 60$ s; incident beam wavelength: $\lambda_{ex} = 640$ nm.
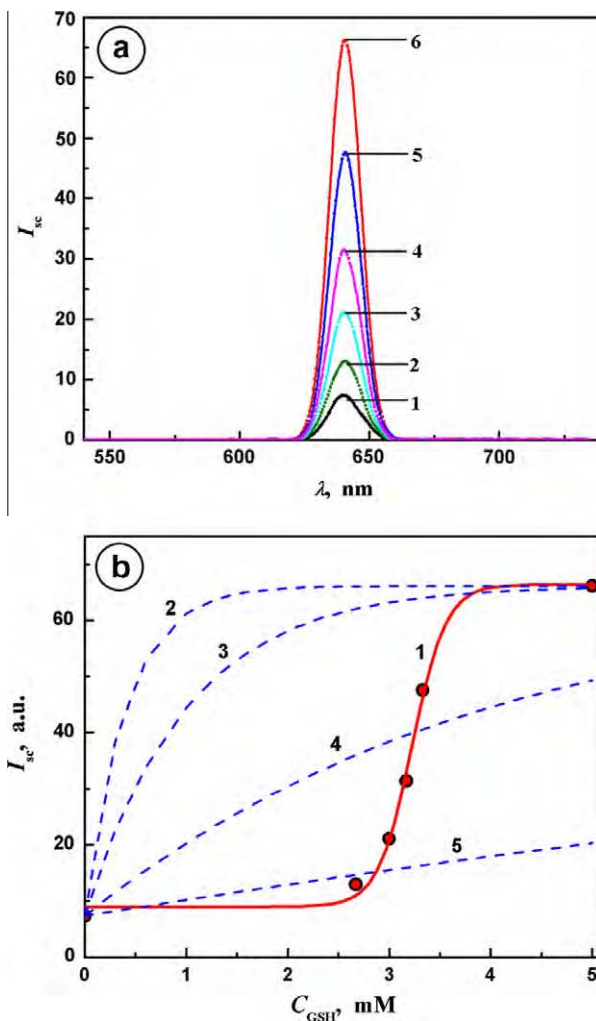
ever, in the presence of GSH an increase in scattering is only observed in the shorter wavelength region, $\lambda < 580$ nm, whereas a decrease in scattering intensity is apparent in the wavelength range above $\lambda = 580$ nm. The origin of the broad scattering peaks with $\lambda_{max} > \lambda_{SP,max}$ nm is ascribed to the increasing reflectivity of free electrons in Au at wavelengths longer than the Frohlich wavelength: $\lambda > \lambda_{Froh} = \lambda_{SP,max}$ where the electrical conductance of nanoparticles becomes a true metallic conductance [82]. At shorter wavelengths, the free conduction electrons in Au are unable to follow fast changing electromagnetic field imposed by the incident light beam.

The scattering intensity increases with nanoparticle concentration as illustrated in Fig. 4 where the dependencies of $I_{sc}$ on $C_{AuNP}$ for $AuNP_{5nm}$ and $AuNP_{22nm}$ are presented. A higher slope $\partial I_{sc}/\partial C_{AuNP}$ is encountered for $AuNP_{22nm}$ than for $AuNP_{5nm}$ consistent with the enhanced scattering by larger particles.

The relationship between the RELS intensity and GSH concentration for small Au nanoparticles, $AuNP_{5nm}$, measured after $\tau = 60$ s of reaction time does not conform to the Langmuirian pseudo-first-order kinetics. This is illustrated in RELS spectra presented in Fig. 5. The dependence of $I_{sc,max}$ on $C_{GSH}$ is sigmoidal, as shown in Fig. 5b, curve 1, indicating on a kinetic threshold. This dependence indicates on the 2D nucleation and growth mechanism of the ligand-exchange process rather than uniform place-exchange mechanism, for which

a pseudo-first-order Langmuirian kinetics describes well the ligand exchange and AuNP assembly in other systems [83–85]. To delineate the difference in the shape of the Langmuirian kinetic characteristics and the one observed experimentally, a family of kinetic curves was calculated for the rate constant values $k$ = 40, 17, 4, and 0.8 M$^{-1}$s$^1$ (curves 2–5) using the kinetic equation [86] derived for random place-exchange assembly with pseudo-first-order Langmuirian kinetics:

$$I_{sc} = \varepsilon(1 - \exp\{-kC_{GSH}\tau\}) + I_{sc,ini} \qquad (3)$$

where $\varepsilon = I_{sc,fin} - I_{sc,ini}$, $k$ is the rate constant, $\tau$ is the reaction time, and $I_{sc,ini}$, $I_{sc,fin}$ are the RELS intensities at $\tau = 0$ and $\tau = \infty$, respectively. These curves show clearly the absence of any threshold in contrast to the experimental curves.

## 3.2. Evolution of surface plasmon absorbance of AuNP on interactions with GSH molecules

To corroborate the conclusion from previous section that gold nanoparticle assembly is responsible for the large scattering increase of AuNP$_{5nm}$ particles upon injection of GSH, we have performed measurements of the surface plasmon band shift under the same conditions as those for Fig. 1. A bathochromic SP band shift and a band broadening are indicative of the SP coupling occurring during the AuNP assembly process [36,37] and can thus be utilized to confirm the assembly. This type of UV–Vis spectroscopic evidence has been supported by the dynamic light scattering (DLS) measurements [33], small-angle X-ray scattering (SAXS) [33,87], and theoretical calculations of spectral shifts [1–5].

The color changes associated with ligand-exchange GSH-induced AuNP assembly are illustrated in Fig. 6. The concentration dependence of the SP absorbance band maximum $\lambda_{max} = f(C_{GSH})$ and $A_{max} = f(C_{GSH})$ recorded within 1 min of the reaction time do not represent a uniform ligand exchange, with GSH replacing the existing citrate SAM, but rather a 2D nucleation and growth process. It is seen that the threshold GSH concentration range is from 1.5 to 2.5 mM (Fig. 6b). The value of $\lambda_{max}$ increases from $\lambda_{max,ini}$ = 522 nm to the final value $\lambda_{max,fin}$ = 576 nm at the plateau established for $C_{GSH} \geqslant$ 2.6 mM. At the same time, $A_{max}$ goes through a maximum and decreases at higher GSH concentrations. In the first stage, for $C_{GSH}$ < 2.28 mM, absorbance maximum increases with $C_{GSH}$ on account of the increasing diameter of GSH-capped AuNP ensembles, while in the second stage, for $C_{GSH}$ > 2.28 mM, absorbance maximum decreases with further increase of $C_{GSH}$ due to the bathochromic shift of the SP band to longer wavelength and natural $1/\lambda$ absorbance decrease. Note that the concentrations required to drive ligand exchange in 60 s of reaction time are much higher than those observed for small thiol molecules such as cysteine or homocysteine which are typically in the low micromolar range. Extensive studies of SP absorbance for various AuNP systems have been carried out by the Zhong group [33–35,88]. In particular, from studies of the GSH-mediated assembly of AuNP [37,62] it follows that the presence of NaCl (10 mM) stimulates GSH-mediated assembly of AuNP$_{11nm}$ while the addition of NaOH (1.6–3.3 mM) reverses it. In our experiments, the pH was maintained at pH = 3.24 ± 0.03 by citrate buffer which is within the range of zwitterionic predominance of GSH species.

The SP band broadening concomitant with bathochromic band shift is clearly observed in Fig. 6. The calculations of the SP band structure for gold and silver nanoparticles have been performed by various groups [1–6] enabling to assess the effects of the size and shape variability of nanoparticles, nanorods, and nanoplates, on plasmonic absorbance. The broadening of the SP band for AuNP has been described by El-Sayed et al. [2,3]. The SP band broadening and bathochromic band shift observed in our experiments corroborate the assembly process.
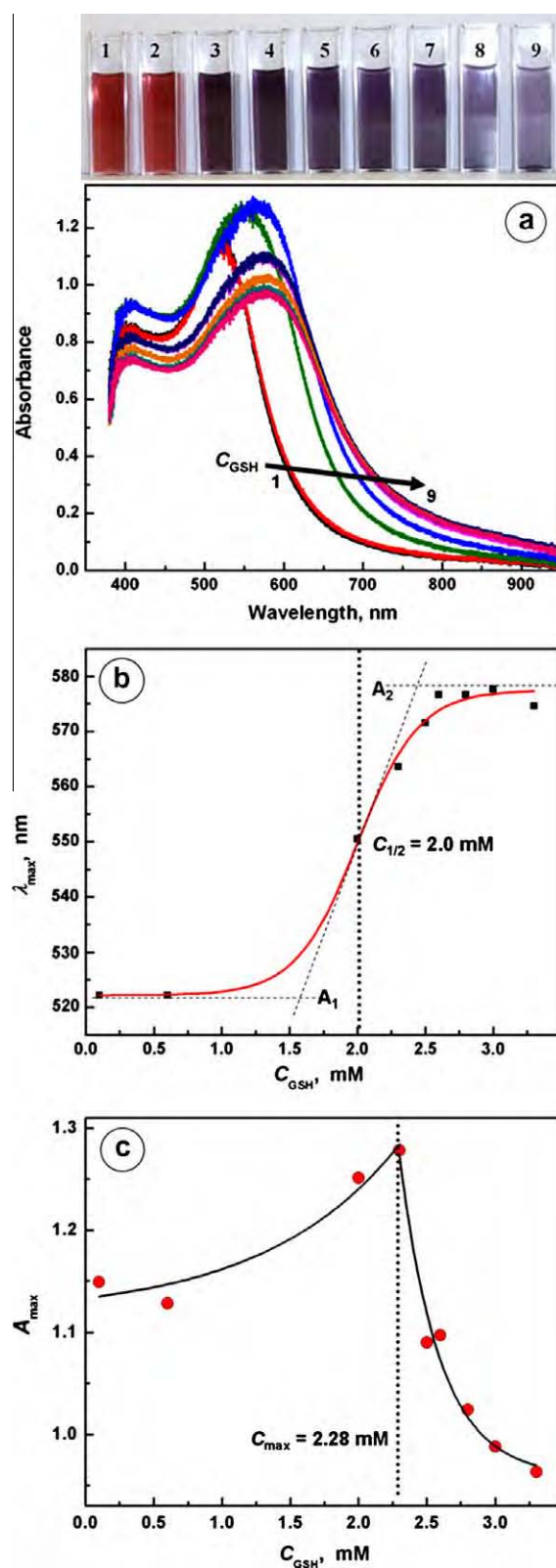


**Fig. 6.** Effect of glutathione concentration on absorbance of 10.1 nM AuNP$_{5nm}$ nanoparticle solution: (a) absorbance spectra for $C_{GSH}$ [mM]: (1) 0.1, (2) 0.67, (3) 2.0, (4) 2.33, (5) 2.5, (6) 2.67, (7) 2.83, (8) 3.0, (9) 3.33; above: color change in response to GSH injections (1–9); (b) dependence of the surface plasmon band wavelength $\lambda_{max}$ on $C_{GSH}$; (c) dependence of SP absorbance maximum $A_{max}$ on $C_{GSH}$.

Similar experiments performed with oxidized glutathione GSSG (not shown) indicate that the transition concentration $C_{1/2,GSSG}$ for

half-way shift of peak wavelength $\lambda_p$ is lower than that for the reduced GSH. For AuNP$_{5nm}$, $C_{1/2,GSSG}$ = 0.83 mM for GSSG for 1 min reaction time in comparison to $C_{1/2,GSH}$ = 2.0 mM for GSH, as determined from fitting of the Boltzmann function:

$$\lambda_p = \lambda_{p,\max} + \frac{(\lambda_{p,\min} - \lambda_{p,\max})}{\left(1 + \exp\left\{\frac{C - C_{1/2}}{s}\right\}\right)} \qquad (4)$$

where $\lambda_{p,\min}$, $\lambda_{p,\max}$ – are the minimum and maximum values of the peak wavelength $\lambda_p$, $C_{1/2}$ is the concentration at the inflection point, and $s$ is the slope parameter. The lower value of $C_{1/2}$ for GSSG than for GSH can be ascribed to the higher 2D nucleation rate for the disulfide where each GSSG molecule contributes 2 GS$^-$ moieties to the forming 2D nucleus.

### 3.3. Long-term monitoring of GSH-mediated AuNP assembly by resonance light scattering

The temporal evolution of RELS signal at $\lambda_{ex}$ = 640 nm, for a 2.5 nM AuNP$_{5nm}$, after addition of GSH (5 mM final concentration), is presented in Fig. 7, for the time span of 10 h. Immediately after GSH injection, a jump of scattering occurs (stage I). This initial reactivity, completed within 1 min of GSH injection, represents a straight vertical line in Fig. 7. As discussed in the next section, the ligand-exchange and GSH-mediated AuNP assembly into small ensembles are responsible for this large change in the scattering cross-section. The initial jump of scattering is followed by a slow exponential decrease of scattering (stages II and III) which is attributed to the film ordering and relaxation after the completion of the ligand-exchange and formation of small assemblies. This process lasts approximately 4.5 h. The duration of the first part of the decay (stage II) is approximately 1.5 h and results in a 12% decrease in RELS intensity. This period is then followed by ca. 3 h of very slow scattering changes (stage III of apparent colloid stability). After that a slow decay of scattering is observed (stage IV) which is due to $C_{AuNP}$ depletion arising from the sedimentation of assemblies. Control experiments indicate on a decrease of absorbance and thus confirm the solution depletion due to sedimentation. This is also corroborated by the observation of precipitated networked AuNP material after 24 h. Larger particles (e.g. AuNP$_{22nm}$) are more likely to show screening of incident light for other AuNP$_{22nm}$ bound in ensembles. Also, the sedimentation begins immediately after the addition of GSH. These might be the main reasons why the decrease of RELS was observed in Fig. 2. To the increased speed of sedimentation may also contribute nanoparticle crystallinity which is higher for AuNP$_{22nm}$ than for AuNP$_{5nm}$ which are spherical. The AuNP$_{22nm}$ nanocrystals have large flat surfaces and the attachment of two particles becomes then much stronger since the interparticle interactions are stronger. This in turn induces the formation of larger aggregates for which both the screening is more efficient and precipitation is faster.

### 3.4. Mechanistic aspects of the interactions of GSH with AuNP

On the basis of measurements described in previous sections, we have evaluated the pathways of GSH interactions and reactivity with core–shell gold nanoparticles. Before presenting the mechanism, it is necessary to assess changes in the thickness of AuNP protecting monolayers. The thickness of a citrate shell around a AuNP is from 0.38 nm (flat orientation) to 0.70 nm (vertical, fully extended orientation) and the height of a GSH molecule adsorbed on a Au is on the order of 1.18 nm based on EQCN measurements and quantum chemical evaluation [30] for GSH adsorbed on solid QC/Au piezoelectrodes. The structure and dimensions of Cit and GSH molecules are shown in Fig. 8. During the ligand exchange (AuNP@Cit + GSH = AuNP@GSH + Cit), the diameter of a single
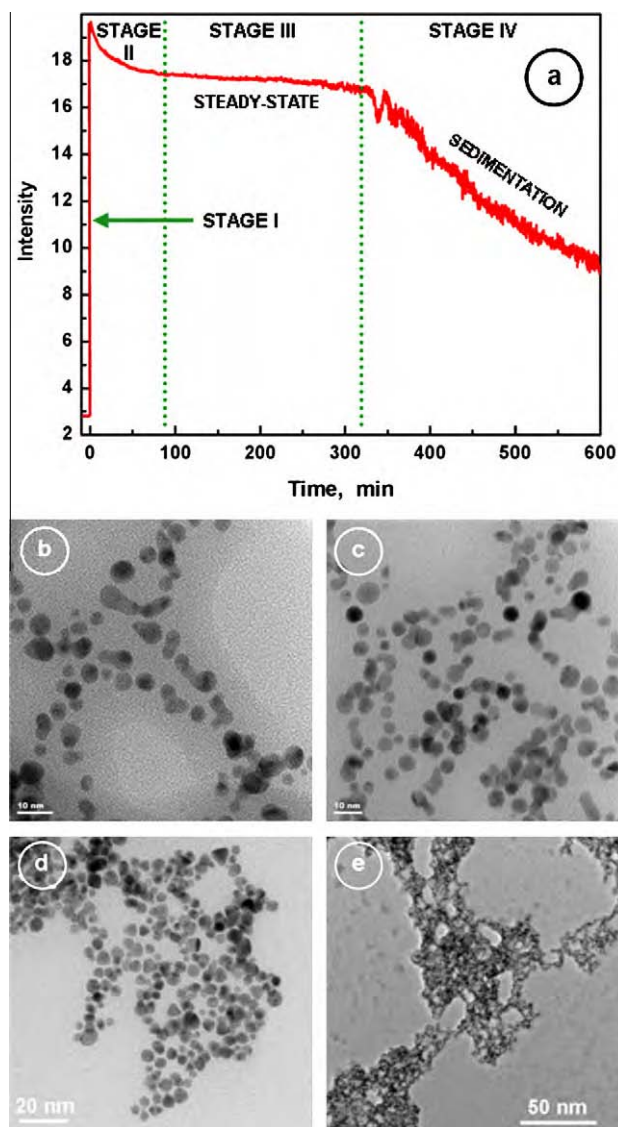


**Fig. 7.** Upper panel: (a) temporal evolution of RELS intensity at $\lambda$ = 640 nm for a 2.5 nM AuNP$_{5nm}$ nanoparticle solution after injection of 5 mM GSH. Lower panel: HR-TEM images obtained during a GSH-induced AuNP assembly; increasing density of AuNP networks from (b) to (e).

AuNP, with core of 5 nm dia., would increase from ca. 6.4 nm to 7.4 nm, or by 15.6%. This is rather a small change of the diameter and so it cannot account for the observed 9-fold scattering intensity increase observed upon injection of GSH to AuNP$_{5nm}$ solution. The change in the refractive index on ligand replacement is small due to the similarity of organic shells and is thus neglected. Therefore, upon addition of GSH to a solution of citrate-capped AuNP, a GSH-mediated assembly of AuNP@GSH must take place.

According to our estimates based on RELS measurements, the diameter of the assemblies is approximately doubled (the effective diameter: $a_1$ = 2.1 $a_0$, where $a_0$ is the diameter of the original citrate-capped AuNP). The GSH-capped AuNP assemblies are depicted in Fig. 8.

During the film relaxation period (stage II), the newly formed GSH SAM is being compacted and the film ordering processes take place. It is also rational to assume that any intermediate structures composed of linker molecules present in the interparticle space are disassembled and removed in favor of more stable direct particle-to-particle bonding through the zwitterionic and H-bond forces.
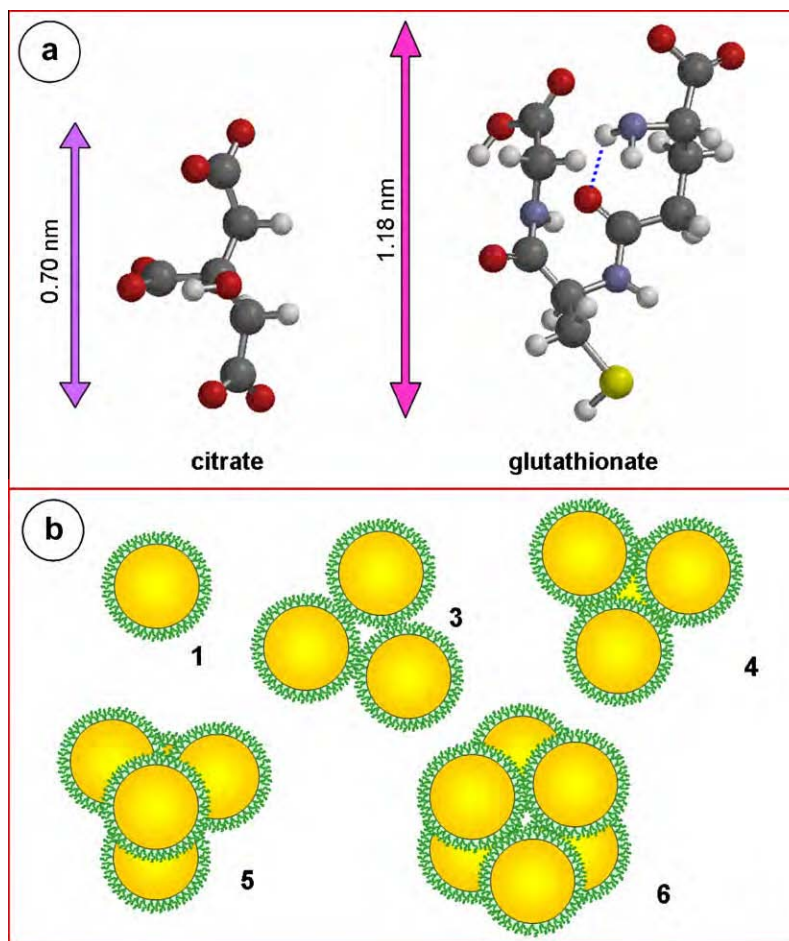
**Fig. 8.** (a) Comparison of heights of AuNP capping molecules: citrate and glutathionate (atoms: yellow – sulfur, red – oxygen, blue – nitrogen, gray – carbon, light gray – hydrogen); (b) small assemblies of $n$ GSH-linked AuNP with diameter $2a_0 < a < 3a_0$ ($n = 3$ to 6, marked at the assemblies), where $a_0$ is the diameter of single AuNP ($n = 1$). (For interpretation of the references to color in this figure legend, the reader is referred to the web version of this article.)
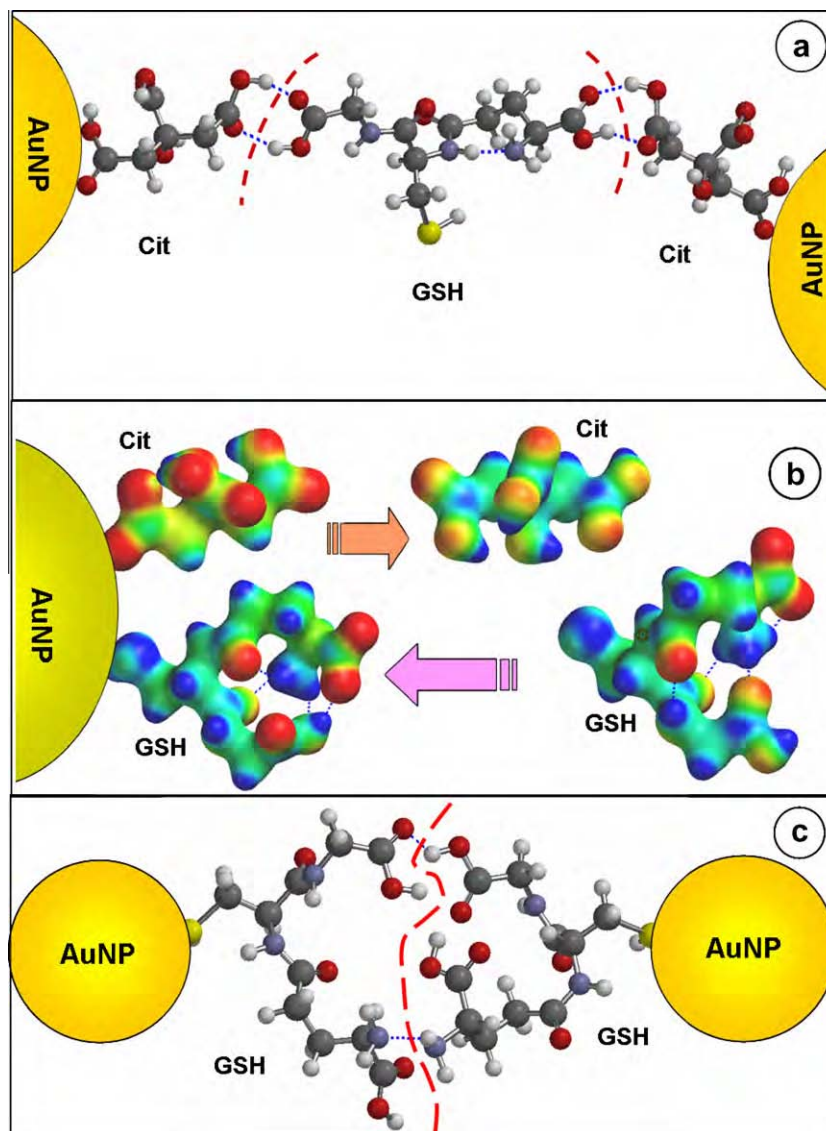
## 3.5. Interparticle hydrogen bonding and electrostatic interactions

In order to verify the feasibility of the mechanism presented above, molecular dynamics simulations and quantum mechanical calculations of structural interdependencies of interacting molecular capping agents and cross-linkers were conducted.

The initiating interactions of GSH molecules with citrate-capped AuNP is likely to break hydrogen bonds between citrate molecules in the citrate SAM on AuNP making the citrate ligands more vulnerable to be pulled out the SAM. One example of such bonding between GSH linker and citrate-capped AuNP is presented in Fig. 9a. The ligand-exchange that follows leads to the complete replacement of weakly bound citrate SAM with more strongly bound GSH-SAM on account of the strong Au–S bonding. While in the stage I of GSH interactions with AuNP the ligand-exchange is completed, provided that sufficiently high concentration of GSH is used ($C_{GSH} > 2.5$ mM), it is likely that interparticle linker structures are formed which facilitate the fast assembly of AuNP, as indicated by the large jump in the scattering intensity. It is rational to assume that these structures (e.g. AuNP@GSH – GSH(aq) – AuNP@GSH) release the linker molecules during the relaxation stage II in favor of directly bonded particle-to-particle ensembles with strong zwitterionic and hydrogen bonding. An example of such interparticle bonding is presented in Fig. 9c. This process represents compacting of ensembles and is therefore reflected in the decrease of scattering. The experimental decrease of ca. 12% of scattering is consistent with this model. Due to the flexibility and

intrinsic multiple-functionality of GSH ligands, a wealth of interparticle interactions becomes possible. Hence, the interparticle interactions of GSH-capped AuNP have been further analyzed by considering the formation of multiple hydrogen bonds as depicted in Fig. 10. It is seen that there are several possibilities for the formation of hydrogen bonds, from a single H-bond up to a triple H-bond. In Fig. 10a, a single H-bond COOH′–COOH″ formed between COOH groups from two GSH molecules is presented. In Fig. 10b, another single H-bond COOH–NH₂ is shown which forms between COOH group from one GSH molecule and NH₂ group from another GSH molecule. Then, in Fig. 10c–e, double H-bonds are presented. They can be formed as follows: (c) two H-bonds on the same couple COOH′–COOH″ where one carboxyl is from one GSH molecule and one from the second GSH molecule; (d) COOH′–COOH″ and COOH′–COOH‴, where the same COOH′ from one GSH molecule forms two H-bonds with two different carboxyl groups COOH″ and COOH‴ from the second GSH molecule; (e) one H-bond COOH′–NH₂ and one COOH″–COOH where two different carboxyl groups (COOH′ and COOH″) in one GSH molecule are involved. A triple H-bond is shown in Fig. 10f: two H-bonds in one carboxylate couple COOH′–COOH″ plus one H-bond COOH‴–NH₂. This means that there is a lot of configurational flexibility in GSH molecules to achieve one- to triple-H-bonding and thus the ensembles of GSH-capped AuNP are considerably strengthened by the selection of H-bonding opportunities.

The formation of hydrogen bonds is augmenting strong zwitterionic interactions due to the polarized groups COO⁻–NH₃⁺ operat-

**Fig. 9.** Mechanism of interactions of GSH with gold nanoparticles: (a) formation of interparticle linkages, (b) ligand exchange, (c) interparticle hydrogen bonding; gold nanoparticles drawn not-to-scale; in (b): electron density surfaces for a model citric acid and glutathione for electron density $d = 0.1$ au$^{-3}$, color coded electrostatic potential: from blue – positive, to red – negative potential. Internal hydrogen bonds are also seen in citric acid and glutathione in (b). (For interpretation of the references to color in this figure legend, the reader is referred to the web version of this article.)

ing in the pH range from 2.04 to 3.4. At pH < 2.04 and pH > 3.4, electrostatic repulsions become the dominant force in the interparticle interactions between GSH-capped gold nanoparticles.

The results presented above corroborate the mechanism of interactions of glutathione molecules with citrate-capped gold nanoparticles, the formation of GSH linkages, and the interparticle interactions of AuNP.

## 4. Conclusions

We have demonstrated that RELS spectroscopy can provide a wealth of information about the interactions of small biomolecules, such as glutathione, with gold nanoparticles and can be applied to monitor the ligand-exchange processes followed by AuNP assembly. The RELS spectroscopic measurements, in conjunction with plasmonic UV–Vis absorbance and HR-TEM imaging, have revealed that the interactions of glutathione with gold nanoparticles are complex and proceed through several stages: (i) ligand-exchange and interparticle cross-linking resulting in AuNP assembly, (ii) relaxation of AuNP ensembles with GSH-SAM ordering and disassembly of interparticle linker structures evidenced by the decrease in light scattering, (iii) period of a metastable colloidal solution (steady-state), (iv) further aggregation with sedimentation. Strong dependence of scattering cross-section on GSH concentration has been found for small AuNP (5 nm dia.) with 9-fold increase of RELS intensity $I_{sc}$ (for $C_{AuNP,5nm} \approx 10$ nM and $C_{GSH} > 2.5$ mM). The calculated effective diameter of assemblies is $2.1a_0$ indicating on the formation of small ensembles (2–6 original nanoparticles). For larger AuNP (22.5 nm dia.), an opposite effect has been observed where the addition of GSH caused a sharp decrease in $I_{sc}$, ascribed to more extensive assembly and sedimentation of aggregates. Indeed, the time-resolved assembly and sedimentation stages in GSH-linked AuNP network formation have been observed in long-term monitoring of GSH–AuNP interactions by RELS for smaller, more stable, AuNP$_{5nm}$ nanoparticle systems. The ligand exchange (citrate for GSH) has been found to deviate from the first-order Langmuirian kinetics observed for some longer chain thiols [83,84] and the obtained characteristics $I_{sc} = f(C_{GSH})$ appear to be a sigmoidal threshold
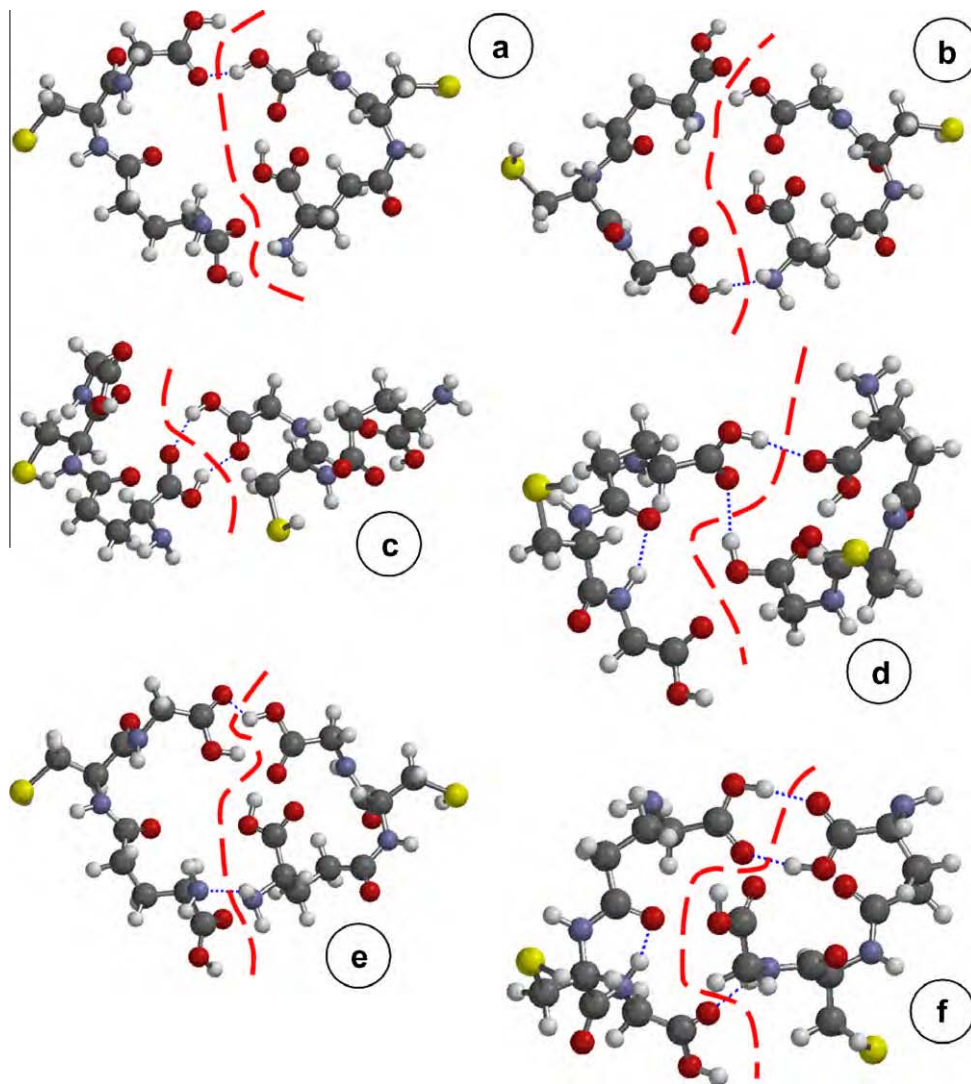
**Fig. 10.** Hydrogen bonding between two glutathione molecules from shells of two interacting AuNP; H-bonds marked with a dotted line; atoms: yellow – sulfur, red – oxygen, blue – nitrogen, gray – carbon, light gray – hydrogen); GSH molecules are separated with a red dashed line. (For interpretation of the references to color in this figure legend, the reader is referred to the web version of this article.)

function resembling that obtained recently for homocysteine ligand [71]. Such a ligand-exchange process is likely to encompass a 2D nucleation and growth process rather than a random place-exchange. The observed SP band broadening and bathochromic shift are consistent with the ligand-exchange and GSH-induced AuNP assembly. These control experiments support the conclusions drawn from the results of RELS measurements. Molecular dynamics and quantum mechanical calculations corroborate the interparticle interactions with zwitterionic and multiple H-bonding leading to GSH-induced AuNP assembly observed experimentally. We have found the RELS spectroscopy to be very useful in elucidating mechanistic aspects of interparticle interactions. The application of RELS can be expanded to monitor reactivities and assembly of other monolayer-protected metal clusters, especially for very fast processes which cannot be followed by other techniques.

## References

[1] K.L. Kelly, E. Coronado, L.L. Zhao, G.C. Schatz, J. Phys. Chem. B 107 (2003) 668–677.
[2] S. Link, M.A. El-Sayed, J. Phys. Chem. B 103 (1999) 8410–8426.
[3] S. Link, M.B. Mohamed, M.A. El-Sayed, J. Phys. Chem. B 103 (1999) 3073–3077.
[4] S. Franzen, J.C.W. Folmer, W.R. Glomm, R. O'Neal, J. Phys. Chem. B 106 (2002) 6533–6540.
[5] C. Ungureanu, R.G. Rayavarapu, S. Manohar, T.G.V. Leeuwen, J. Appl. Phys. 105 (2009) 102032.
[6] A.L. Gonzales, C. Noguez, J. Comput. Theor. Nanosci. 4 (2007) 231.
[7] M. Sugawara, A. Hirano, P. Buhlmann, Y. Umezawa, Bull. Chem. Soc. Jpn. 75 (2002) 187.
[8] J.J. Gooding, I. Pugliano, D.B. Hibbert, P. Erokhin, Electrochem. Commun. 2 (2000) 217.
[9] W.U. Wang, C. Chen, K.H. Lin, Y. Fang, Proc. Natl. Acad. Sci. U. S. A. 102 (2005) 3208–3212.
[10] M. Hepel, J. Dallas, M.D. Noble, Sensors Transducers J. 88 (2008) 47.
[11] M. Hepel, J. Dallas, M.D. Noble, J. Electroanal. Chem. 622 (2008) 173–183.
[12] I. Szymanska, M. Stobiecka, C. Orlewska, T. Rohand, D. Janssen, W. Dehaen, H. Radecka, Langmuir 24 (2008) 11239–11245.
[13] J. Halamek, M. Hepel, P. Skladal, Biosens. Bioelectron. 16 (2001) 253.
[14] J. Pribyl, M. Hepel, J. Halamek, P. Skladal, Sens. Actuators B 91 (2003) 333.
[15] J. Pribyl, M. Hepel, P. Skladal, Sens. Actuators B 113 (2006) 900.
[16] M. Stobiecka, J.M. Cieśla, B. Janowska, B. Tudek, H. Radecka, Sensors 7 (2007) 1462–1479.
[17] A.P. Alivisatos, K.P. Johnsson, X. Peng, T.E. Wilson, C.J. Loweth, M.P. Bruchez, P.G. Schultz, Nature 382 (1996) 610.
[18] S.J. Park, T.A. Taton, C.A. Mirkin, Science 295 (2002) 1503–1505.

[19] J.J. Storhoff, R. Elghanian, R.C. Mucic, C.A. Mirkin, R.L. Letsinger, J. Am. Chem. Soc. 120 (1998) 1959–1964.
[20] T.A. Taton, G. Lu, C.A. Mirkin, J. Am. Chem. Soc. 123 (2001) 5164–5165.
[21] T.A. Taton, R.C. Mucic, C.A. Mirkin, R.L. Letsinger, J. Am. Chem. Soc. 122 (2000) 6305–6306.
[22] R.A. Reyolds, C.A. Mirkin, R.L. Letsinger, J. Am. Chem. Soc. 122 (2000) 3795–3796.
[23] I.I.S. Lim, U. Chandrachud, L. Wang, S. Gal, C.J. Zhong, Anal. Chem. 80 (2008) 6038–6044.
[24] R. Elghanian, J.J. Storhoff, R.C. Mucic, R.L. Letsinger, C.A. Mirkin, Science 277 (1997) 1078–1081.
[25] B. Dubertet, M. Calame, A.J. Libchaber, Nat. Biotechnol. 19 (2001) 365–370.
[26] E. Matijevic, Medical Applications of Colloids, Springer Sci., New York, 2008.
[27] L. Tong, Y. Zhao, T.B. Huff, M.N. Hansen, A. Wei, J.X. Cheng, Adv. Mater. (Weinheim, Germany) 19 (2007) 3136.
[28] T.B. Huff, L. Tong, Y. Zhao, M.N. Hansen, J.X. Cheng, A. Wei, Nanomedicine 2 (2007) 125.
[29] C.H. Chou, D. Chen, C.R.C. Wang, J. Phys. Chem. B 109 (2005) 11135.
[30] M. Hepel, E. Tewksbury, J. Electroanal. Chem. 552 (2003) 291–305.
[31] M. Hepel, E. Tewksbury, Electrochim. Acta 49 (2004) 3827–3840.
[32] C. Fang, X. Zhou, Electroanalysis 15 (2002) 1632–1638.
[33] M.M. Maye, I.I.S. Lim, J. Luo, Z. Rab, D. Rabinovich, T. Liu, C.J. Zhong, J. Am. Chem. Soc. 127 (2005) 1519–1529.
[34] I.I.S. Lim, W. Ip, E. Crew, P.N. Njoki, D. Mott, C.J. Zhong, Langmuir 23 (2007) 826–833.
[35] F.X. Zhang, L. Han, L.B. Israel, J.G. Daras, M.M. Maye, N.K. Ly, C.J. Zhong, Analyst 127 (2002) 462–465.
[36] P.K. Sudeep, S.T.S. Joseph, K.G. Thomas, J. Am. Chem. Soc. 127 (2005) 6516–6517.
[37] I.M.S. Lim, D. Mott, W. Ip, P.N. Njoki, Y. Pan, S. Zhou, C.J. Zhong, Langmuir 24 (2008) 8857–8863.
[38] Z.P. Li, X.R. Duan, C.H. Liu, B.A. Du, Anal. Biochem. 351 (2006) 18.
[39] S. Mandal, A. Gole, N. Lala, R. Gonnade, V. Ganvir, M. Sastry, Langmuir 17 (2001) 6262.
[40] P.R. Selvakannan, S. Mandal, S. Phadtare, R. Pasricha, M. Sastry, Langmuir 19 (2003) 3545.
[41] M. Hepel, J. Dallas, Sensors 8 (2008) 7224–7240.
[42] E. Chow, D.B. Hibbert, J.J. Gooding, Analyst 130 (2005) 831.
[43] K. Takehara, M. Aihara, Y. Miura, F. Tanaka, Bioelectrochem. Bioenerg. 39 (1996) 135.
[44] K. Takehara, M. Aihara, N. Ueda, Electroanalysis 6 (1994) 1083.
[45] K. Takehara, Y. Ide, M. Aihara, Bioelectrochem. Bioenerg. 29 (1991) 113.
[46] K. Takehara, Y. Ide, M. Aihara, E. Obuchi, Bioelectrochem. Bioenerg. 29 (1992) 103.
[47] M. Noble, M. Mayer-Proschel, C. Proschel, Antioxid. Redox Signaling 7 (2005) 1456–1467.
[48] S. Bernard, A. Enayati, L. Redwood, H. Roger, T. Binstock, Med. Hypotheses 56 (2001) 462–471.
[49] T. Clark-Taylor, Med. Hypotheses 62 (6) (2003) 970–975.
[50] K.M. Beard, N. Shangari, B. Wu, P.J. O'Brien, Mol. Cell. Biochem. 252 (2003) 331.
[51] G. Polidoro, C.D. Ilio, A. Arduini, G.L. Rovere, G. Federici, Int. J. Biochem. 16 (1984) 505–509.
[52] G. Almazzan, H.N. Liu, A. Knorchid, S. Sundararajan, A.K. Martinez-Bermudez, S. Chemtob, Free Radical Biol. Med. 29 (2000) 858–869.
[53] M. Repetto, C. Reides, M.L.G. Carretero, M. Costa, G. Griemberg, S. Llesuy, Clin. Chim. Acta 255 (1996) 107–117.

[54] S. Upadhya, S. Upadhya, S.K. Mohan, K. Vanajakshamma, M. Kunder, S. Mathias, Indian J. Clin. Biochem. 19 (2004) 80–83.
[55] T.W. Clarkson, Environ. Health Perspect. 100 (1992) 31–38.
[56] C.T. Dameron, R.N. Reese, R.K. Mehra, P.J. Kortan, M.L. Carrol, M.L. Steigerwald, L.E. Brus, D.R. Winge, Nature 338 (1989) 596.
[57] J. Barbas, V. Santhanagopalan, M. Blaszczynski, W.R. Ellis, D.R. Winge, J. Inorg. Biochem. 48 (1992) 95.
[58] O.K. Vatamaniuk, S. Mari, Y. Lu, P.A. Rea, J. Biol. Chem. 275 (2000) 31451–31459.
[59] O.K. Vatamaniuk, E.A. Bucher, J.T. Ward, P.A. Rea, J. Biol. Chem. 276 (2001) 20817.
[60] R.K. Mehra, D.R. Winge, J. Cell. Biochem. 45 (1991) 30.
[61] M. Inouhe, Braz. J. Plant Physiol. 17 (2005) 65–78.
[62] S. Zhang, X. Kou, Z. Yang, Q. Shi, G.D. Stucky, L. Sun, J. Wang, C. Yan, Chem. Commun. (2007) 1816.
[63] X. Kou, S. Zhang, Z. Yang, C.K. Tsung, G.D. Stucky, L. Sun, J. Wang, C. Yan, J. Am. Chem. Soc. 129 (2007) 6402.
[64] C.J. Ackerson, M.T. Sykes, R.D. Kornberg, Natl. Acad. Sci. U. S. A. 102 (2005) 13383.
[65] R.F. Pasternack, C. Bustamante, P.J. Collings, A. Giannetto, E.J. Gibbs, J. Am. Chem. Soc. 115 (1993) 5393–5399.
[66] R.F. Pasternack, Science 269 (5226) (1995) 935.
[67] Y.T. Wang, F.L. Zhao, K.A. Li, S.Y. Tong, Anal. Chim. Acta 396 (1999) 75–81.
[68] Z.X. Guo, H.X. Shen, Anal. Chim. Acta 408 (2000) 177–182.
[69] X. Wu, U.Y. Wang, M. Wang, S. Sun, J. Yang, Y. Luan, Spectrochim. Acta A 61 (2005) 361–366.
[70] Z. Jia, J. Yang, X. Wu, C. Sun, S. Liu, F. Wang, Z. Zhao, Spectrochim. Acta A 64 (2006) 555–559.
[71] M. Stobiecka, J. Deeb, M. Hepel, Biophys. Chem. 146 (2010) 98–107.
[72] J. Turkevich, P.C. Stevenson, J. Hiller, Discuss. Faraday Soc. 11 (1951) 55–75.
[73] P.W. Atkins, R.S. Friedman, Molecular Quantum Mechanics, Oxford University Press, Oxford, 2004.
[74] W.J. Hehre, L. Radon, P.R. Schleyer, J.A. Pople, Ab-initio Molecular Orbital Theory, Wiley, New York, 1985.
[75] A.C. Templeton, W.P. Wuelfing, R.W. Murray, Acc. Chem. Res. 33 (2000) 27–36.
[76] C.J. Zhong, M.D. Porter, J. Am. Chem. Soc. 116 (1994) 11616.
[77] J.F. Smalley, K. Chalfant, S.W. Feldberg, T.M. Nahir, E.F. Bowden, J. Phys. Chem. B 103 (10) (1999) 1676–1685.
[78] J. Luo, N. Kariuki, L. Han, M.M. Maye, L.W. Moussa, S.R. Kowaleski, F. Louis Kirk, M. Hepel, C.J. Zhong, J. Phys. Chem. B 106 (36) (2002) 9313–9321.
[79] M.A. Porter, J.R. Hall, J.C. Locke, J.H. Jensen, P.A. Molina, Proteins: Struct., Funct., Bioinf. 63 (3) (2006) 621–635.
[80] A.T. Masheter, P. Abiman, G.G. Wildgoose, E. Wong, L. Xiao, N.V. Rees, R. Taylor, G.A. Attard, R. Baron, A. Crossley, J.H. Jonesd, R.G. Compton, J. Mater. Chem. 17 (2007) 2616–2626.
[81] R.K. Shervedani, Electroanalysis 20 (5) (2008) 550–557.
[82] S. Franzen, J.C.W. Folmer, W.R. Glomm, R. O'Neal, J. Phys. Chem. A 106 (2002) 6533–6540.
[83] R. Georgiadis, K.P. Peterlinz, A.W. Peterson, J. Am. Chem. Soc. 122 (2000) 3166–3173.
[84] A. Kassam, G. Bremner, B. Clark, G. Ulibarri, R.B. Lennox, J. Am. Chem. Soc. 128 (2006) 3476–3477.
[85] I.I.S. Lim, M.M. Maye, J. Luo, C.J. Zhong, J. Phys. Chem. B 109 (2005) 2578–2583.
[86] M. Stobiecka, M. Hepel, Sens. Actuators, submitted for publication.
[87] A.E. Saunders, M.B. Sigman, B.A. Korgel, J. Phys. Chem. B 108 (2004) 193–199.
[88] I.I.S. Lim, F. Goroleski, D. Mott, N. Kariuki, W. Ip, J. Luo, C.J. Zhong, J. Phys. Chem. B 110 (2006) 6673–6682.

# Multimodal Coupling of Optical Transitions and Plasmonic Oscillations in Rhodamine B Modified Gold Nanoparticles

Magdalena[a] Stobiecka and Maria Hepel[a]*

The optical properties of a photoluminescent dye Rhodamine B (RhB) interacting with gold nanoparticles (AuNP) have been investigated using plasmonic absorbance, fluorescence, and resonance elastic light scattering (RELS) spectroscopy. We have found that these interactions result in a multimodal coupling that influence optical transitions in RhB. In absorbance measurements, we have observed for the first time the coupling resulting in strong screening of RhB $\pi$-$\pi$* transitions, likely caused by a contact adsorption of RhB on a conductive surface of AuNP. The nanoparticles quench also very efficiently the RhB fluorescence. We have determined that the static quenching mechanism with a non-Förster fluorescence resonance energy transfer (FRET) from RhB molecules to AuNP is involved. The Stern-Volmer dependence $F_0/F = f(Q)$ shows an upward deviation from linearity, attributed to the ultra-high quenching efficiency of AuNP leading to the new extended Stern-Volmer model. A sharp RELS peak of RhB alone ($\lambda_{max} = 566$ nm) has been observed for the first time and attributed to the resonance fluorescence and enhanced scattering. This peak is completely quenched in the presence of $AuNP_{22nm}$. Our quantum mechanical calculations confirm that the distance between AuNP surface and conjugated $\pi$-electron system in RhB is well within the range of plasmonic fields extending from AuNP. The optical transition coupling to plasmonic oscillations and the efficient energy transfer due to the interactions of fluorescent dyes with nanoparticles are important for biophysical studies of life processes and applications in nanomedicine.

## 1. Introduction

Although known as pigments for centuries, the gold nanoparticles have only recently become of a widespread interest with the emergence of nanotechnology owing to their unique optical and electronic properties [1-8] and exciting applications in new fields such as nanomedicine [9] (for imaging, sensing, and therapy), in biosensors, and in energy conversion devices [10-14]. The gold nanoparticles have also been found to act as very efficient quenchers for fluorescent dyes [15-21]. It is believed that the quenching process is due to the fluorescence resonance energy transfer (FRET) [22-25] from the dye molecules to gold nanoparticles (AuNP). This property of AuNP has found applications in fluorescence microscopy in studies of biochemical processes. For instance, photoluminescent (PL) dyes quenched by AuNP can be attached to AuNP through a ssDNA chain enabling very sensitive single-mismatch detection of a target DNA [17]. We have recently investigated a number of fluorescent dyes interacting with AuNP and we report here on the interactions of rhodamine B dye with AuNP.

Rhodamine B (RhB) is a fluorescent dye belonging to the group of xanthene dyes. Owing to the structural rigidity and chemical stability, it shows a high fluorescence quantum yield $\varphi_F = 0.31$ [26]. In acidic solutions, RhB is a monocation due to the positive charge on the nitrogen. The deprotonation of the carboxylic group at the benzene ring attached to xanthene moiety (pK$_a$ = 3.2 [27]) makes rhodamine B a zwitterion in

neutral solutions. According to Magde et al. [26], the emission maximum for RhB$^+$ cation is $\lambda_{em} = 568$ nm and shifts to a longer wavelength $\lambda_{em} = 583$ nm for RhB zwitterion while the quantum efficiency increases from $\varphi_F = 0.24$ for RhB$^+$ cation to $\varphi_F = 0.31$ for RhB zwitterion. The fluorescence lifetime for RhB$^+$ in water is $\tau_F = 1.52$ ns and increases in lower dielectric constant solvents (e.g. in octanol, $\tau_F = 3.18$). RhB is used extensively in ELISA assays, flow cytometry, and fluorescence microscopy [28]. In order to attach RhB as the label to a protein inside a cell, the isothiocyanate group (-N=C=S) is introduced to the carboxyphenyl ring in RhB and this derivative is then reactive toward amine groups on the protein. Due to high lipophilicity, RhB has been employed as the fluorescent probe for imaging organelles [29].

The Förster-type fluorescence quenching due to FRET between RhB and biocompounds is often utilized in analytical determinations. The optical tracking, based on FRET, of organically modified silica nanoparticles as DNA carriers has been proposed by Prasad et al. [30]. This method can provide a new, non-viral, nanomedicinal approach for gene delivery. The methods of covalent attachment of FRET systems to bioactive molecules have been widely investigated, including the incorporation of novel FRET systems to synthetic DNA [31]. The benzotriazole-derivatized RhB has recently been proposed as a strongly adhering dye for surface-enhanced resonance Raman scattering analysis [32]. Interestingly, silver nanoparticles do not appear to quench the fluorescence of RhB [33], although the opposite is true for R6G. Less prone to environmental variation is Rh 101, which is also used as a

fluorescence polarization standard [34], but its absorbance and emission spectra are red-shifted and offer smaller spectral overlap with AuNP than RhB does. In general, a RET in a bimolecular dye-quencher system, involves a single dipole-dipole interaction formulating the Förster RET. In the case of a dye-nanoparticle system, the dipole-dipole interaction is replaced with a dipole-multipole interaction [35, 36] characteristic for the nanomaterial surface energy transfer (NSET) with an extended $(1/R^4)$ distance dependence.

For studies of particle and molecule interactions presented in this work, we have applied fluorescence spectroscopy and resonance elastic light scattering (RELS) spectroscopy. The RELS technique is inherently sensitive to the interparticle distance and the dielectric function of the medium surrounding the metal nanoparticles. The elastic light scattering is a fast two-step process in which light is momentarily absorbed by a particle and then the absorbed energy, without any loss, is coherently re-emitted in all directions. RELS occurs when polarizable particles are subjected to the oscillating electric field of a beam of light which induces oscillating dipoles in the particles and these dipoles radiate light to the surroundings. The RELS spectroscopy has become a very sensitive and convenient technique in analytical determinations of interacting proteins, DNA, and complexes [37-40]. The light-scattering properties of AuNP applied as labels have been utilized in biomedical imaging, in optical coherence tomography [41, 42], dark-field microscopy [43, 44], and multi-photon microscopy [45, 46]. The absorption of light by AuNP, followed by scattering and nonradiative de-excitation processes, leads to the temperature increase which is applied in cancer therapy [47-49] to kill cancerous cells and as a sensitivity enhancement in photoacoustic spectroscopy [50, 51]. Theoretical description of optical properties of AuNP is based on the Mie theory [52]. Extensive studies have been performed to predict scattering from AuNP with different shapes and sizes using analytical solutions or discrete dipole approximation simulations [53-63].

In this work, we have investigated the effects of rhodamine B interactions with gold nanoparticles on optical properties of the system. We have found that these interactions result in multimodal coupling of optical transitions and surface plasmon oscillations. These phenomena, described in detail, are important for biomedical applications of fluorescent dyes and metal nanoparticles.

## 2. Experimental

*Chemicals.* All chemicals used for investigations were of analytical grade purity. Fluorescent dye Rhodamine B and tetrachloroauric(III) acid trihydrate (HAuCl$_4$·3H$_2$O), 99.9+ % metals basis, were purchased from Sigma Aldrich Chemical Company (Atlanta, GA, U.S.A.) and used as received. Sodium citrate, dihydrate (C$_3$H$_2$(OH)(COONa)$_3$·2H$_2$O) was obtained from J.T. Baker Chemical Co. (Phillipsburg, NJ, U.S.A.). Sodium borohydride (NaBH$_4$) was obtained from Fisher Scientific Company (Pittsburgh, PA, U.S.A.). Solutions were prepared using Millipore (Billerica, MA, U.S.A.) Milli-Q deionized water (conductivity $\sigma = 55$ nS/cm).

*Apparatus.* A high-resolution transmission electron microscope (HR-TEM), Model JEM-2010 (Jeol, West Chester, PA, U.S.A.), with 200 kV accelerating voltage, was used for imaging of Au nanoparticles. The elastic light scattering spectra were recorded using LS55 Spectrometer (Perkin Elmer, Waltham, MA, U.S.A.) equipped with 20 kW Xenon light source operating in 8 µs pulsing mode. Pulse width at half height was less than 10 µs. Separate monochromators for the incident and detector beams enabled using monochromatic radiation with wavelengths from 200 to 800 nm with 1 nm resolution. The system was equipped with sharp cut-off filters: 290, 350, 390, 430, 515 nm. The dual detector system consisted of a photo multiplier tube (PMT) and an avalanche photo diode. The RELS spectra were obtained at $90^0$ angle from the incident (excitation) light beam. The excitation beam monochromator was either scanned simultaneously with the detector beam monochromator ($\Delta\lambda = 0$) or set at a constant excitation wavelength. The UV-Vis spectra were recorded using Perkin Elmer Model Lambda 50 Spectrophotometer in the range 400 to 900 nm or Model R4000 Precision Spectrometer (Ocean Optics, Dunedin, FL, U.S.A.) in the range 340 to 900 nm.

*Procedures.* The Au nanoparticles were synthesized by the method reported by Turkevich et al. [64]. Briefly, to obtain 5 nm AuNP, a solution of HAuCl$_4$ (10 mM, 2.56 mL) was mixed with a trisodium citrate solution (10 mM, 9.6 mL), ratio 1: 3.75, and poured to distilled water (88 mL). The obtained solution was vigorously stirred and fresh cold NaBH$_4$ solution (5 mM, 8.9 mL) was added dropwise. The solution slowly turned light grey and then ruby red. Stirring was maintained for 30 min. Syntheses were also performed using the citrate reduction of gold under reflux. The final products containing core-shell citrate-capped gold nanoparticles were transparent ruby red. The mean size of AuNP determined by TEM was 5.0±0.9 nm ($n = 85$) and 22.5±0.9 nm ($n = 60$) for a borohydride and citrate reduction, respectively; these nanoparticles are denoted as AuNP$_{5nm}$ and AuNP$_{22nm}$, respectively. The solutions were prepared fresh just before the experiments, with citrate buffer, pH = 5, $C_{Cit} = 0.46$ mM (final concentration). The concentrations of AuNP's are given in moles of particles per 1 L of solution (usually, in the nM range). The concentrations of AuNP solutions were determined from exact amounts of reagents used in synthesis and the size of AuNP particles determined by TEM image analysis. All concentrations specified for mixed solutions are final concentrations. The RhB stock solution in water (20 µM) was screened from light.

Molecular dynamics (MD) and quantum mechanical (QM) calculations of electronic structure for rhodamine B molecule and its interactions with citrate capped gold nanoparticles were performed using density functional theory (DFT) with B3LYP functional [65, 66] with 6-31G* basis set, semi-empirical PM3 method, and strongly correlated advanced Moller-Plesset method, embedded in Wavefunction Spartan 6 [66]. The electron density and local density of states are expressed in atomic units, au$^{-3}$ (1 au = 0.529157 Å and 1 au$^{-3}$ = 6.749108 Å$^{-3}$).

## 3. Results and discussion

### 3.1. Local surface plasmon spectroscopy of AuNP in the presence of rhodamine B

Typical UV-Vis spectrum of the surface plasmon (SP) band of citrate-capped $AuNP_{22nm}$ is presented in Figure 1, curve 1. The position of the SP absorbance maximum ($A_1$) is at the wavelength $\lambda_{max} = 530$ nm in the absence of RhB. After addition of RhB (10 μM, final concentration), a second maximum $A_2$ appears on the spectrum at $\lambda_{max} = 556$ nm (curve 2). This spectral change differs from those associated with simple nanoparticle assembly observed in other systems, e.g. mercaptopropionic acid- or glutathione-induced assembly.
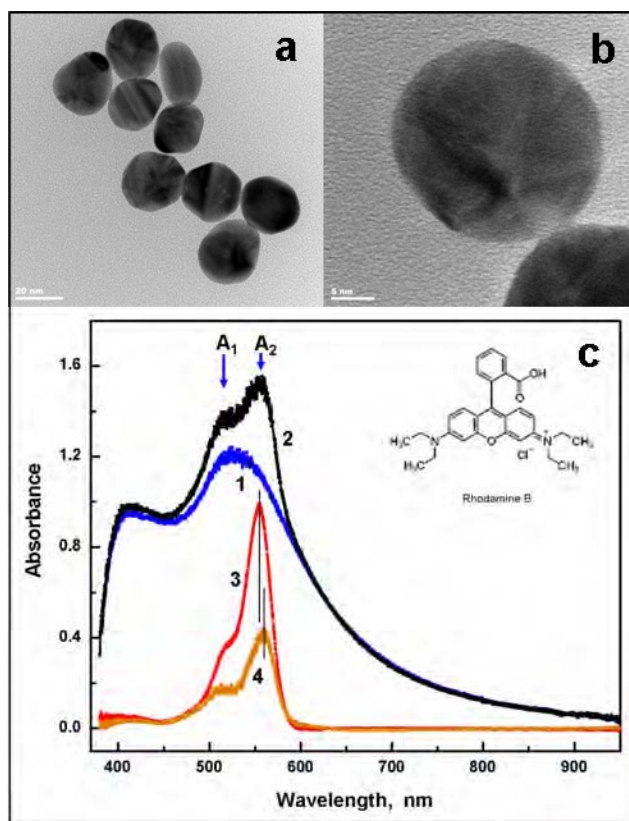


**Figure 1.** (a,b) TEM images of gold nanoparticles at a resolution (bar length) of: (a) 20 nm and (b) 5 nm; (c) UV-Vis spectra for: (1) surface plasmon absorbance band of 0.88 nM $AuNP_{22nm}$, (2) 0.88 nM $AuNP_{22nm}$ + 10 μM RhB; (3) 10 μM RhB without gold nanoparticles; (4) difference spectrum (2)-(1) reflecting the absorbance increase in the presence of 10 μM RhB.

By comparing the absorbance spectrum of RhB (curve 3) showing the RhB π-π* transitions at $\lambda_{max} = 555$ nm, with the spectrum for AuNP + RhB, it becomes evident that both spectra are superimposed. To check if there is a straightforward additivity of these spectral features, we have subtracted spectrum 1 from spectrum 2 and obtained difference spectrum 4. This spectrum can be directly compared with spectrum 3 which was recorded for 10 μM RhB in the absence of AuNP. It is clear that the spectra for AuNP and for RhB are not additive and a considerable absorbance loss of 58.6% is apparent. This loss is most likely due to the AuNP screening associated with high electrical conductivity of gold which renders optical transitions of RhB ineffective and results in diminished absorbance of light energy by the dye molecules. For this to happen, the RhB molecules would need to be tightly adsorbed around AuNP. Such an interaction is not unlikely due to the positive charge on N-atom in RhB molecule and a negatively charged citrate shell of AuNP. We have confirmed the adsorption of RhB on a solid Au electrode surface using electrochemical quartz crystal nanobalance. The surface coverage $\Gamma$ and monolayer mass $\Delta m$ of RhB were found to be: $\Gamma = 0.16$ nmol/cm$^2$, $\Delta m = 77$ ng/cm$^2$, close to the theoretical values for a horizontal orientation of RhB: $\Gamma_{th} = 0.149$ nmol/cm$^2$, $\Delta m_{th} = 71.4$ ng/cm$^2$).
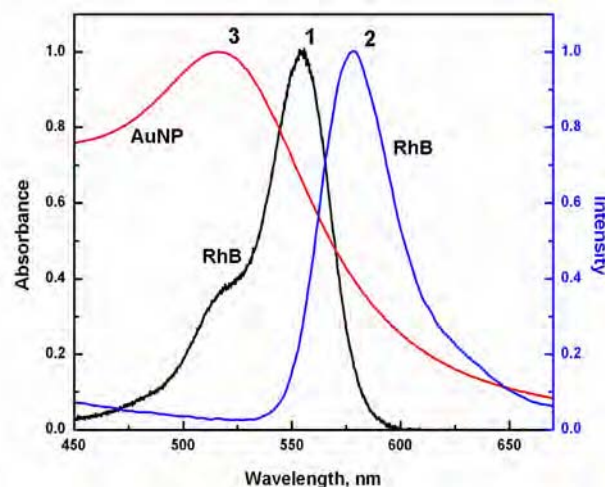


**Figure 2**. Normalized fluorescence spectra for rhodamine B solutions: (1) absorbance spectrum and (2) emission spectrum for excitation at $\lambda_{ex} = 340$ nm and (3) normalized absorbance spectrum of gold nanoparticles $AuNP_{22nm}$, showing considerable overlap of RhB emission and AuNP absorbance.

A small screening effect for rhodamine B isothiocyanate adsorbed on mercaptooctanoate-stabilized $AuNP_{10nm}$ has been observed by Franzen et al. [67]. About 40% decrease of rhodamine 6G absorbance upon addition of 2.5 nm AuNP gold nanoparticles was observed by Kamat et al. [18]. Moreover, by comparing, in Fig.1, spectrum 3 ($\lambda_{max} = 555$ nm) and difference spectrum 4 ($\lambda_{max} = 560$ nm), a bathochromic shift of RhB absorption band is encountered which is likely due to the change in the solvation shell of RhB associated with adsorption on a nanoparticle. Such changes are expected and indeed reported [68]. Since the close interactions of RhB with AuNP may result in photoluminescence quenching of RhB, more detailed investigations of such an effect have been performed and they are described in the next sections.

### 3.2. Photoluminescence of RhB and the quenching effect of AuNP

The normalized RhB absorbance and photoluminescence emission spectra are presented in Figure 2. The luminescence maximum is observed at $\lambda_{em,max} = 578$ nm ($\lambda_{ex} = 450$ nm).

The norm alized S P abs orbance spectrum of a s olution of AuNP i s al so i ncluded in Figure 2 to de monstrate the la rge overlap of AuNP ab sorbance wit h RhB em ission characteristics. S uch an overlap is a pre requisite of an efficient energy trans fer (F RET), provi ded that the dis tance between the interacting dipole molecule and surface multipole is sufficiently small.

The effect of AuNP on RhB photoluminescence signal ha s been evaluated in F igure 3 for 50 nM RhB solution in experiments without AuNP a nd with ad dition o f 0.8 8 n M $AuNP_{22nm}$. It i s s een that the fluorescence peak of RhB at $\lambda_{PL,max}$ = 578 nm observed in curve 1, is completely quenched upon t he addi tion of AuNP (curve 3). (Note that t he enhancement of RhB fluorescence by AuNP, recently reported by Zhu et al. [69], has been ob served at 3- orders o f magnitude higher concentrations of RhB (66.9 µM)).
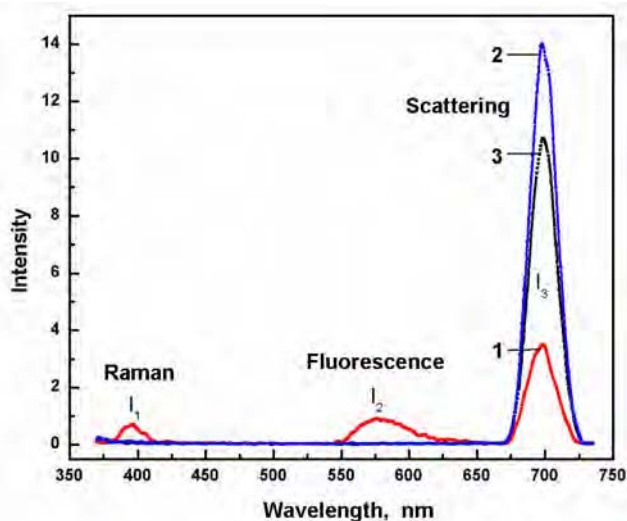


**Figure 3.** Fluorescence spectra for: (1) 50 nM RhB solution, (2) 0.88 nM $AuNP_{22nm}$, and ( 3) 50 nM RhB + 0. 88 nM $AuNP_{22nm}$. Excitation: $\lambda_{ex}$ = 348 nm. Peaks: $I_1$ – Ram an water vibration, $I_2$ – RhB f luorescence, $I_3$ – secondary Rayleigh scattering.

The s econdary Ra yleigh s cattering obs erved in F igure 3 a t $\lambda_{RELS}$ = 698 nm increases in intensity due the strong scattering propensity of AuNP. The so lution of AuNP with t he same concentration shows no PL signal near $\lambda_{PL}$ = 578 nm but stil l larger scattering at $\lambda_{RELS}$ = 698 nm (curve 2). This means that RhB molecules reduce the s cattering intensity of AuNP. The reduction in scattering inte nsity is likely to be due to t he change in the dielectric fun ction of the medium (shell ) surrounding the nanoparticle.

By increasing the concentration of RhB, while maintaining the concentration of AuNP con stant, the PL signal of RhB can be recovered but with co nsiderably lower qua ntum y ield and lower fl uorescence signal sensitivity: $\partial I_{PL}/\partial C_{RhB}$. Thi s is illustrated in Figure 4, for RhB concentration range from 0.01 µM to 10 µM. The fluore scence m aximum is reds hifted in comparison to that in the absence of gold nanoparticles. From the plot of $I_{PL}$ vs . $C_{RhB}$ i n Figure 4 c, i t is seen th at the fluorescence intensity is nearly linear up to $C_{RhB}$ = 5 µM and then shows negative deviations from linea rity, likel y due to chemical effects (concentration quenching, H-aggregate
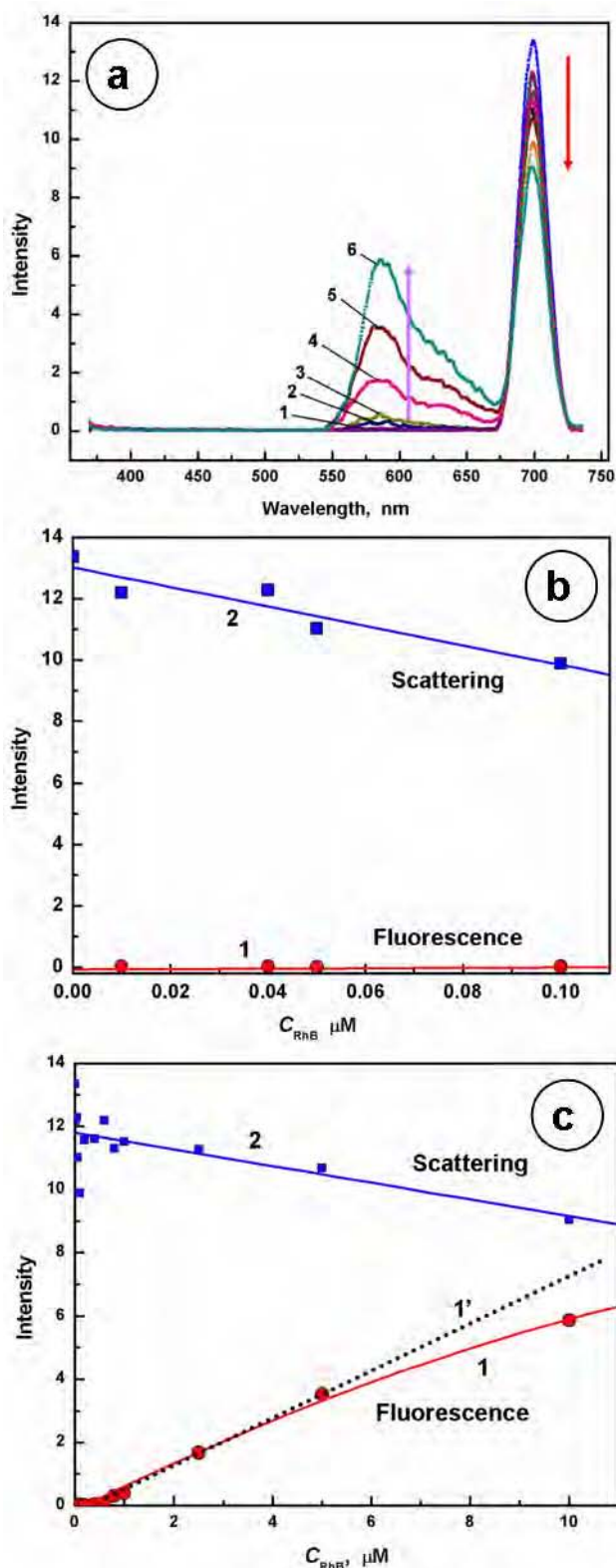


**Figure 4.** Fluor escence spectra (a) for solutions of 0. 88 nM $AuNP_{22nm}$ + RhB [ µM]: (1 ) 0 .6, (2 ) 0 .8, (3 ) 1 .0, (4 ) 2 .5, (5 ) 5 .0, (6 ) 1 0.0. (b ,c) Dependence of f luorescence intensity ( 1) and secondar y scatter ing intensity (2) on concentration of RhB. Excitation: $\lambda_{ex}$ = 348 nm.

formation, etc.). At the same time, the intensity of the secondary light scattering decreases slowly with increasing $C_{RhB}$ (Fig. 4c, curve 2).

In Figure 5, presented are two dependencies of $I_{PL}$ on $C_{RhB}$ for RhB solutions in the absence and in the presence of AuNP quenchers, curves 1 and 2, respectively. The deviation from linearity seen for curve 1 is due to the relatively high concentration of the dye ($C_{RhB} > 1$ µM). The difference in the initial slope of curves 1 and 2 indicates on a very high quenching efficiency of AuNP. The quantum efficiency of fluorescence for RhB alone is high (according to Magde et al. [26] $\varphi_0 = 0.31$, Demas and Crosby [70] reported $\varphi_0 = 0.71$ at room temperature; Huth et al. [71] obtained $\varphi_0 = 0.45$-$0.50$ at 293 K;

Karstens and Kobe [72] after careful evaluation of temperature dependence of RhB and rhodamine 101 suggested that $\varphi_0 \leq 0.5$; according to Lindsay et al. [73], $\varphi_0 = 0.70$ for RhB in ethanol, close to 0.68 found by Snare et al. [74] in 94% ethanol). Assuming the value of $\varphi_0 = 0.31$ after the recent determination for unperturbed RhB in water, we can calculate the quantum efficiency of RhB fluorescence in the presence of 0.88 nM AuNP$_{22nm}$ as follows:

$$\varphi_q = (F_q/F_0) \, k\varphi_0 \qquad (1)$$

where $F_0$ and $F_q$ are the fluorescence intensities for RhB in the absence and in the presence of 0.88 nM AuNP$_{22nm}$, respectively, and $k$ is the correction function for chemical quenching due to the high concentration of the dye used for comparison of the quenched and unquenched fluorescence. The value of $\varphi_q$ thus obtained is: $\varphi_q = 0.01$. This small value of fluorescence quantum efficiency confirms the high quenching effectiveness of AuNP.

### 3.3. Resonance elastic light scattering from AuNP/RhB nanoparticles

The RELS intensity vs. wavelength spectra $I_{sc}$ - $\lambda$ for AuNP, RhB, and AuNP/RhB solutions are presented in Figure 6. For a 0.88 nM AuNP solution, a large and broad RELS peak is encountered in the wavelength range from $\lambda_1 = 550$ nm to $\lambda_1 = 750$ nm, with the scattering maximum located at $\lambda_{max} = 653$ nm. This scattering peak is characteristic of AuNP$_{22nm}$. In quasi-static approximation [75], the scattering efficiency $Q_{sc}$ is given by:

$$Q_{sc} = \frac{128\pi^4 a^4 \varepsilon_m^2}{3\lambda^4} \left| \frac{\varepsilon - \varepsilon_m}{\varepsilon + 2\varepsilon_m} \right|^2 \qquad (2)$$

where $\varepsilon$ is the complex dielectric function ($\varepsilon = \varepsilon_1 + i\varepsilon_2$) of the metal core of Au nanoparticles [76-78], $\varepsilon_m$ is the dielectric constant of the medium, and $a$ is the nanoparticle radius.

The origin of the broad scattering peak at $\lambda_{max} = 653$ nm is ascribed to the increasing reflectivity of Au at wavelengths longer than the Frohlich wavelength:

$$\lambda > \lambda_{Froh} \qquad (3)$$

where the dielectric function $\varepsilon$ for gold becomes more negative than $-2\varepsilon_m$ [67]; here $\lambda_{Froh} = \lambda_{SP,max}$.
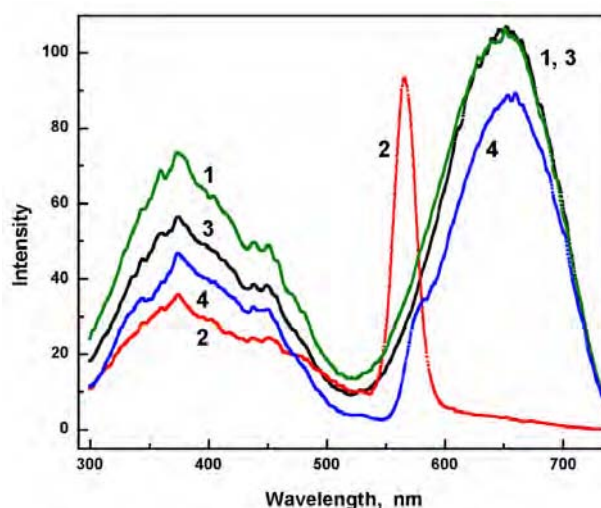
On the other hand, the RhB alone in a 500 nM solution, shows a narrow RELS peak at $\lambda_{max} = 566$ nm. Beyond this peak, there is virtually no scattering at longer wavelengths ($\lambda > 600$ nm). After the addition of AuNP to RhB solution, the RELS spectrum changes dramatically and the strong RhB scattering at $\lambda_{max} = 566$ nm is completely quenched by AuNP. At the same time, there is no effect of RhB seen on the broad AuNP peak at $\lambda_{max} = 653$ nm. By increasing the concentration of RhB 20-fold (to 10 µM), a small decrease of the AuNP RELS intensity at $\lambda_{max} = 653$ nm is observed (curve 4) which is due to screening effects described in previous sections. A small barely distinguishable shoulder on the main RELS peak at $\lambda = 577$ nm is also observed which is reminiscent of the sharp RELS peak of the pure RhB solution at $\lambda_{max} = 566$ nm, observed in curve 2.

The concentration dependence of the sharp RhB RELS peak at $\lambda_{max} = 566$ nm, has been examined in the range from 25 nM to 500 nM RhB. The obtained RELS spectra are presented in Figure 7. The concentration dependence of scattering intensity maximum $I_{sc,max} = f(C_{RhB})$, shown in the inset, indicates that this dependence is linear with a slope of $\partial I_{sc,max}/\partial C_{RhB} = 0.186 \times 10^9$ M$^{-1}$. The position of the RELS maximum, $\lambda_{max} = 566$ nm, is in the midst between the absorbance maximum ($\lambda_{max} = 555$ nm) and the fluorescence emission maximum ($\lambda_{max} = 578$ nm) emphasizing equal importance of absorbance and emission as the steps of a scattering process. Taking into account these circumstances, it is plausible to conclude that the origin of the RELS peak at
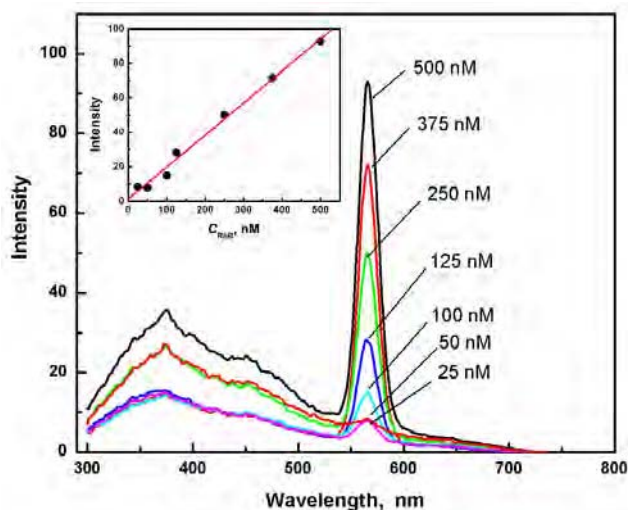


**Figure 7.** RELS spectra of $I_{sc}$ vs. $\lambda$ for RhB solutions with concentrations [nM]: (1) 25, (2) 50, (3) 100, (4) 125, (5) 250, (6) 375, (7) 500. Inset: Dependence of $I_{sc,max}$ on RhB concentration.

$\lambda_{max} = 566$ nm is associated with the combined resonance scattering and resonance fluorescence and should be composed of signals differing in phase: a fast coherent signal (scattering) and a slower incoherent signal (fluorescence). The narrow half-peak width ($w = 25$ nm) corroborates the conclusion that a resonance is involved.

### 3.4. Resonance energy transfer from RhB to AuNP

The static absorbance and scattering screening effects discovered for the RhB-modified AuNP suggest a tight adsorption of RhB on AuNP and a resonance energy transfer (RET) from the dye molecule to the local surface plasmon in AuNP. In the energy transfer processes, usually described in terms of a bimolecular quenching:

$$D^* + A \rightarrow D + A^* \qquad (4)$$

the excitation energy is transferred from an excited donor $D^*$ molecule to a ground-state acceptor A resulting in quenching of $D^*$ and sensitization of A [22-24]. This adds a new decay channel to the existing decay route of $D^*$ [21], as expressed by the overall decay rate constant $k$:

$$k = \tau_D^{-1} + k_Q[A] \qquad (5)$$

where $\tau_D$ is the emission lifetime and $k_Q$ is the bimolecular quenching rate constant. Although, the mechanism of RET is different for NSET, the collisional dynamics for sufficiently low concentration of dye and AuNP remains the same. In order to check if quenching is due to RET in solution (i.e. the dynamic collisional quenching without adsorption of the dye on AuNP), the critical quencher concentration $Q_0$ has been determined for 500 nM RhB from the experimental data of Fig. 8a using the dependence:

$$\eta = 1 - \frac{F_{DA}}{F_D} = \sqrt{\eta}\gamma \exp(\gamma^2) erfc(\gamma) \qquad (6)$$

representing the solution to the collision frequency problem, where erfc($\gamma$) is the complementary error function:

$$erfc(\gamma) = 1 - erf(\gamma) = \frac{2}{\sqrt{\pi}} \int_\gamma^\infty \exp(-t^2) dt \qquad (7)$$

$F_D$ and $F_{DA}$ are the fluorescence intensities in the absence and in the presence of an acceptor, respectively, and:

$$\gamma = Q/Q_0 \qquad (8)$$

For $Q = Q_0$, $\gamma = 1$ and the critical quenching efficiency $\eta^*_{(\gamma=1)}$ can be readily found from the right-hand-side of eq. (6):

$$\eta^*_{(\gamma=1)} = 0.76. \qquad (9)$$

Now, from the experimental data showing $\eta = 1 - F_{DA}/F_D = 0.76$, we obtain: $Q = Q_0 = 0.3 \times 10^{-9}$ M. The critical distance $R_0$ is then calculated according to the equation:

$$R_0 = \sqrt[3]{\frac{3000}{2\pi^{3/2}NQ_0}} \qquad (10)$$

where $N$ is the Avogadro number and $R_0$ is in cm. The value of $R_0$ obtained is too large ($R_0 = 1.14$ µm) for any RET to occur in solution and thus energy transfer must proceed in direct contact between the dye and AuNP, i.e. in an adsorption film of RhB on AuNP surface. The control experiments performed using quartz crystal nanogravimetry [36] have confirmed contact adsorption of RhB on a Au surface. The adsorption of RhB has been recently reported [79] also for other surfaces. A strong quenching of RhB fluorescence by AuNP has been found in experiments described in Fig. 3 and 5. Since the dynamic collisional quenching is not likely to occur, as indicated above, the tests for static quenching have been performed. If the FRET mechanism is based on static quenching, a linear Stern-Volmer plot should be obtained:

$$\frac{F_0}{F} = 1 + K_{SV}Q \qquad (11)$$

where $K_{SV}$ is the quenching constant. Therefore, a series of experiments with varying concentration of AuNP quencher have been performed. The results obtained are plotted in

Figure 8b as t he dependence: $F_0/F = f(Q)$ where $F_0$ is the fluorescence in the abs ence of AuNP and $F$ – is the fluorescence i n the pres ence of AuNP quencher at a
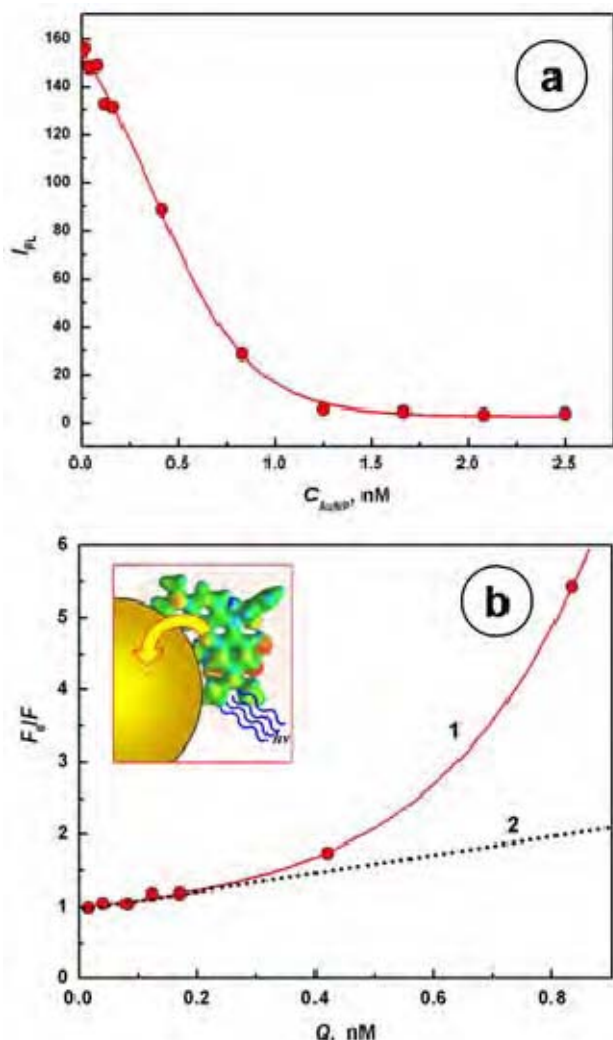


concentration $Q$.

**Figure 8.** Quenching of RhB fluorescence emission by AuNP$_{5nm}$ (a) and FRET dependence of $F_0/F$ vs. $C_{AuNP}$ for solutions of 500 nM RhB + $x$ nM AuNP$_{5nm}$ (b).

It is seen that the plot $F_0/F = f(Q)$ is not linear and shows an upward de viation fr om linea rity. While such a deviatio n could be o bserved fo r a combined dy namic and static quenching, it is not likely the case here since we have already excluded t he possibility of dy namic collisional quenc hing. We have ob served the hy per-linear Stern -Volmer pl ots al so for other dye-AuNP systems, e.g. for coumarin 4, coumarin 7, fluorescein, and Nile bl ue, so the case of rhodamine B i s not an exception. The deviation from linearity of $F_0/F$ vs. $Q$ plots is most likely associated with the high quenching efficiency of AuNP leading to the extended Stern-Volmer relation[36] .

$$\frac{F_0}{F} = 1 + \frac{KQ_{tot}}{\left(1 + \dfrac{KF}{\varepsilon}\right)} \qquad (12)$$

where $\varepsilon$ is the dye fluores cence intens ity factor ($\varepsilon = F/C_{RhB}$), $Q_{tot}$ is the t otal concent ration of active site s on t he nanoparticle q uenchers, and $K$ is the bindi ng equilibri um constant. The strong di stance dependence of RET which in Förster theory is proportional to $1/R^6$, extends to longer ranges in NS ET due t he weake r, $1/R^4$, depen dence of RET [35]. The analysis of e nergy trans fer di stances i s presented in the next section. It has to be empha sized that the simultaneou s RELS measurements do not i ndicate on any assembl y of AuNP (t he RELS inten sity does not incr ease upon ad dition of Rh B to AuNP), hence there i s no c omplication of the que nching relationship coming from the AuNP network formation.

### 3.5. Modeling rhodamine B interactions with gold nanoparticles

In order to g ain further in sights into the nature of the interactions of RhB m olecules with AuNP, MD simulations and QM calculations for model RhB-citrate of the AuNP shell have been performed.
In Figure 9, the side- and top-views of an ens emble created in direct interactions of RhB molecule with a citric acid molecule are pres ented. The electron dens ity s urfaces ($\rho = 0.05$) were calc ulated u sing se mi-empirical PM3 method a nd DFT at the B3LYP-functional level. The electron den sity surface is m apped with an ele ctrostatic pote ntial (blue-to-red colored areas correspond to high-to-low potential values).
The two molecules fo rm a hy drogen bond bet ween one of th e oxygens of t he carboxy l grou ps of cit ric acid and carboxyphenyl group of Rh B. At the sa me time, another carboxylate group of citric acid interacts with the $N^+$ center of the py ronine group o f RhB. A scissor s-like structu re is formed, a s shown in Fig. 9a, with considerable flexibility in scissoring movement due t o the relative ly large angle adjustability of the h ydrogen bond. The planar rigid str ucture of the xanthene grou p i s p reserved but the interaction of carboxyphenyl grou p wit h x anthene moiety is di minished because of the hy drogen bonding with AuNP shell. Thi s should result in the increased rate of nonradiative decay. This mechanism has been confirmed in fluorescence measurements in other systems, e.g. i n protic solvents with vary ing polarity.
In F igure 10, t he electros tatic interactions between the RhB cation and de protonated citrate anion are pres ented. In contrast to t he arrange ment of Figure 9, the prefe rred arrangement i s no w the extended con figuration, wit h rhodamine N $^+$ center bein g attracted by two car boxylate groups of the c itrate anion. T he planar rigi d structure of the xanthene gr oup is pre served and so th e fluoresce nce properties of the dye molecule should be preserved.
As the di stance between RhB and citrate m olecules is fixe d after MD si mulations and c orresponds to an equilibrated complex, the li kely dis tances for t he energy transfer can be evaluated as follows . T he distance from delocalized $\pi$-electron s ystem to the gol d surface can be es timated from the following ato mic distances: (i) for RhB adsorbed horizontally on to p of a cit rate-capped Au NP, $d_{min} = 0 .32$ nm b etween surface Au-at oms and clos est C atom of the xanthene group, (ii) for RhB adsorbed vertically on a citrate-capped AuNP,
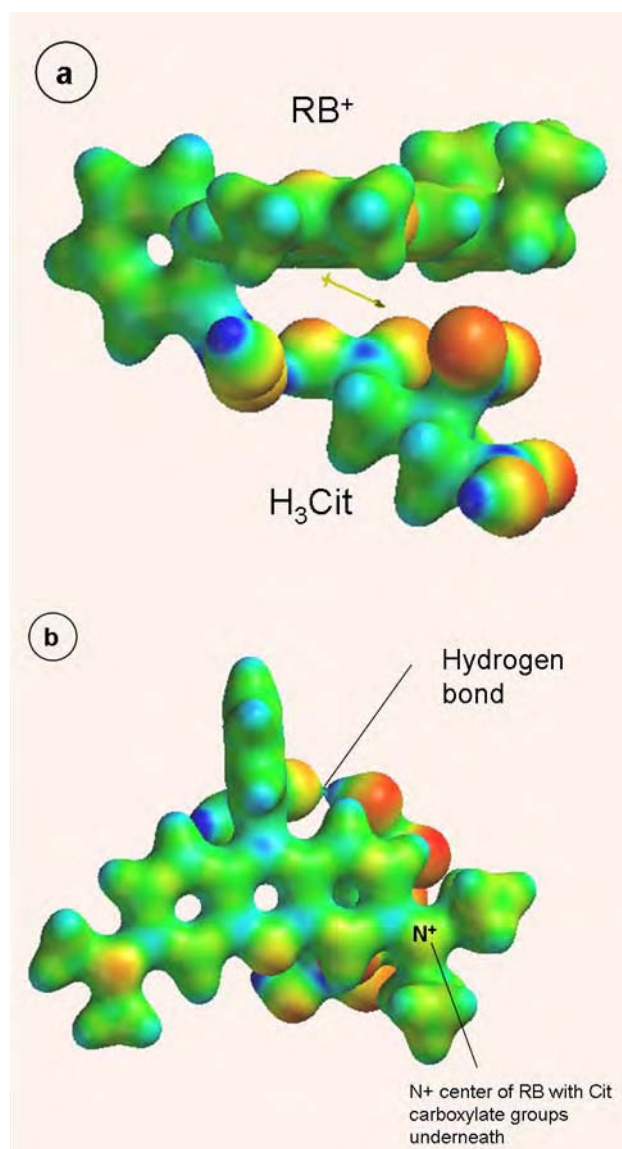
**Figure 9.** Electronic structure of rhodamine B interacting with citrate molecule of a model citrate-capped core-shell Au nanoparticle: (a) side view, (b) top view; hydrogen bond indicated with an arrow. Electron density surface ($\rho = 0.05$) mapped with electrostatic potential (red-to-blue coloring corresponds to the lower-to-higher potential).

$d_{\min} = 0.46$ nm, and (iii) for RhB adsorbed horizontally on Au, $d_{\min} = 0.24$ nm between surface Au-atoms and the $N^+$-center of RhB can be estimated. Therefore, the close distances of the delocalized $\pi$-electron system to the electron cloud of a surface plasmon on AuNP surface can readily facilitate the NSET. These distances can be favorably compared to the maximum distance of the interparticle surface plasmon coupling which is effective for interparticle distances up to $d \approx 5r = 56$ nm, where $r = 11.25$ nm is the nanoparticle radius. The plasmonic field extends then to at least 28 nm from each particle. Therefore, this long range coupling and weak $1/R^4$ distance dependence of RET in NSET provide conditions for strong enhancement of the gold nanoparticle quenching of fluorescent dyes.



.
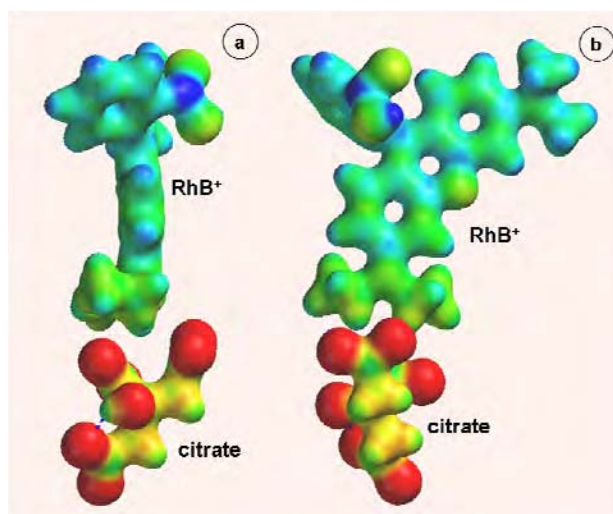
**Figure 10.** Electron density surfaces and molecular arrangement of rhodamine B cation attracted electrostatically to a citrate anion of a model citrate-capped core-shell Au nanoparticles: (a) side view, (b) front view; no hydrogen bonds are formed in this configuration. Electron density surfaces ($\rho = 0.05$) are mapped with electrostatic potential (red-to-blue coloring corresponds to the lower-to-higher potential).

In summary, the model calculations corroborate experimental conclusion that RhB molecules interact strongly with the citrate-capped core-shell AuNP. In these interactions, both the electrostatic and hydrogen bonding are involved.

## 4. Conclusions

We have investigated the effects of rhodamine B interactions with gold nanoparticles on optical properties of the system and we have found a multimodal coupling of optical transitions with electronic SP oscillations. Firstly, these interactions result in lowering of RhB $\pi$-$\pi^*$ transition efficiency attributed to the screening effect of conduction electrons of AuNP. This indicates that RhB is adsorbed on the surface of citrate-capped AuNP's. Secondly, the fluorescence emission of RhB appears to be quenched by a static non-Förster energy transfer mechanism (NSET). Thirdly, a non-linear Stern-Volmer relation, $F_0/F = f(Q)$, has been found. This non-linearity can ascribed to the ultra-high quenching efficiency of AuNP leading to the extended Stern-Volmer relation. Fourthly, a sharp RELS band of RhB alone ($\lambda_{\max} = 566$ nm) has been discovered and attributed to the combined resonance scattering and resonance fluorescence, and this band is completely quenched in the presence of AuNP. Finally, the strong RELS band at $\lambda_{\max} = 653$ nm, observed for AuNP$_{22nm}$, with a high peak-to-valley scattering intensity ratio, $I_P : I_V = 7.7$, is screened to some extent by the interacting RhB molecules at higher RhB concentrations. The results of MD simulations and QM calculations performed indicate that both hydrogen bonding and electrostatic interactions are involved in an ensemble formed by RhB with citrate-capped AuNP. Whereas the covalent binding of a dye through a well-defined spacer provides an excellent definition

of the distance for studying energy transfer, the contact adsorption can also serve as an option for establishing the distance for resonance energy transfer. In the case of RhB, the contact adsorption on a citrate-coated Au surface was confirmed by EQCN. Our QM calculations have shown that the distance for a dipole-multipole energy transfer in RhB-AuNP system is well within the range of plasmonic fields extending from the nanoparticles. The plasmonic field range ($d \approx 28$ nm) is estimated to be several times larger than the distance between the $\pi$-conjugated electron system of RhB and the AuNP surface ($d = 0.32$ nm). Therefore, a very efficient quenching of RhB fluorescence by AuNP is possible.

## Notes and references

*a* Department of Chemistry, State University of New York at Potsdam, Potsdam, NY 13676, USA. Fax: 1 315 267 3170; Tel: 1 315 267 2267; E-mail: hepelmr@potsdam.edu
*Corresponding Author*
† See DOI: 10.1039/b000000x/

1. M. M. Alvarez, J. T. Khoury, T. G. Schaaff, M. N. Shafigullin, I. Vezmar and R. L. Whetten, *J. Phys. Chem. B*, 1997, **101**, 3706-3712.
2. P. G. Etchegoin, E. C. l. Ru and M. Meyer, *J. Phys. Chem.*, 2006, **125**, 164705-164701.
3. P. B. Johnson and R. W. Christy, *Phys. Rev. B*, 1972, **6**, 4370.
4. P. V. Kamat, *J. Phys. Chem. B*, 2002, **106**, 7729-2244.
5. S. Link and M. A. El-Sayed, *J. Phys. Chem. B*, 1999, **103**, 8410-8426.
6. S. Link, M. B. Mohamed and M. A. El-Sayed, *J. Phys. Chem. B*, 1999, **103**, 3073-3077.
7. Y. Ping, D. Hanson, I. Koslov, T. Ogitsu, O. Prendergast, E. Schwegler, G. Collins and A. Ng, *Phys. Plasmas*, 2008, **15**, 056303.
8. J. Perez-Juste, I. Pastoriza-Santos, L. M. L iz-Marzan and P. Mulvaney, *Coord. Chem. Rev.*, 2005, **249**, 1870.
9. E. Matijevic, *Medical Applications of Colloids*, Springer Sci., New York, 2008.
10. L. Han, J. Luo, N. Kariuki, M. M. May e, V. W. Jones and C. J. Zhong, *Chem. Mater.*, 2003, **15**, 29.
11. N. N. Kariuki, J. Luo, M. M. Maye, S. A. Hassan, T. Menard, H. R. Naslund and C. J. Zhong, *Langmuir*, 2004, **20**.
12. M. M. Maye, N. N. Kariuki, J. Luo, L. Han, P. Njoki, L. Wang, Y. Lin, H. R. Naslund and C. J. Zhong, *Gold Bull.*, 2004, **37**, 217.
13. J. Luo, M. M. Maye, N. N. Kariuki, L. Wang, P. Njoki, Y. Lin, M. Schadt, H. R. Naslund and C. J. Zhong, *Catal. Today*, 2005, **99**, 291.
14. J. Luo, M. M. Maye, V. Petkov, N. N. Kariuki, L. Wang, P. Njoki, D. Mott, Y. Lin and C. J. Zhong, *Cham. Mater.*, 2005, **17**, 3086.
15. A. C. Templeton, D. E. Cliffel and R. W. Murray, *J. Am. Chem. Soc.*, 1999, **121**, 7081.
16. O. V. Makarova, A. E. Ostafin, H. Miyoshi, J. R. Norris and D. Meisel, *J. Phys. Cheem. B*, 1999, **103**, 9080.
17. B. Dubertet, M. Calame and A. J. Libchaber, *Nature Biotechnology*, 2001, **19**, 365-370.
18. N. Chandrskharan, P. V. Kamat, J. Hu and G. Jones, *J. Phys. Chem. B*, 2000, **104**, 11103.
19. C. C. Huang and H. T. Chang, *Anal. Chem.*, 2006, **78**, 8332-8338.
20. I. I. S. Lim, F. Goroleski, D. Mott, N. Kariuki, W. Ip, J. Luo and C. J. Zhong, *J. Phys. Chem. B*, 2006, **110**, 6673-6682.
21. J. R. Lakowicz, *Principles of Fluorescence Spectroscopy*, Springer, New York, 2006.
22. T. Forster, *Z. Naturforsch.*, 1949, **49**, 321.
23. T. Forster, *Z. Elektrochem. Angew. Phys. Chem.*, 1949, **53**, 93.
24. T. Forster, *Discuss. Faraday Soc.*, 1959, **27**, 7.
25. T. Forster, in *Modern Quantum Chemistry*, ed. O. Sinanoglu, Academic Press, New York, 1968, vol. 3, p. 93.
26. D. Magde, G. E. Rojas and P. Seybold, *Photochem. Photobiol.*, 1999, **70**, 737-744.
27. R. W. Ramette and E. B. Sandell, *J. Am. Chem. Soc.*, 1956, **78**, 4872-4878.
28. G. W. Gordon, G. Berry, X. H. Liang, B. Levine and B. Herman, *Biophysical J.*, 1998, **74**, 2702-2713.
29. F. V. v. Steyern, J. Q. Jesefsson and S. Tagerud, *J. Histochem. Cytochem.*, 1996, **64**, 267-274.
30. I. Roy, T. Y. Ohulchanskyy, D. J. Bharali, H. E. Pudavar, R. A. Mistretta, N. Kaur and P. N. Prasad, *PNAS*, 2004, **102**, 279-284.
31. L. Clima and W. Bannwarth, *Helv. Chim. Acta*, 2008, **91**, 165-175.
32. E. F. McCabe, D. Graham, D. McKeown and W. E. Smith, *J. Raman Spectroscopy*, 2004, **36**, 45-49.
33. M. C. Marchi, S. A. Bilmes and G. M. Bilmes, *J. Colloid Interface Sci.*, 1999, **218**, 112-117.
34. T. J. V. Prazeres, A. Fedorov, S. P. Barbosa, J. M. G. Martinho and M. N. Berberan-Santos, *J. Phys. Chem. A*, 2008, **112**, 5034-5039.
35. C. S. Yun, A. Javier, T. Jennings, M. Fisher, S. Hira, S. Peterson, B. Hopkins, N. O. Reich and G. F. Strouse, *J. Am. Chem. Soc.*, 2005, **127**, 3115-3119.
36. M. Stobiecka and M. Hepel, 2010, (submitted).
37. R. F. Pasternack and P. J. Collings, *Science*, 1995, **269**, 935-939.
38. M. Stobiecka, J. Deeb and M. Hepel, *Biophys. Chem.*, 2010, **146**, 98-107.
39. M. Stobiecka, K. Coopersmith and M. Hepel, *J. Colloid Interface Sci*, 2010, **350**, *168-177*.
40. M. Stobiecka and M. Hepel, *Sensors Actuators B*, 2010, **149**, 373-380.
41. A. L. Oldenburg, M. N. Hansen, D. A. Zweifel, A. Wei and S. A. Bopart, *Opt. Espress*, 2006, **14**, 6724.
42. T. S. Troutman, J. K. Barton and M. Romanowski, *Opt. Lett.*, 2007, **32**, 1438.
43. P. K. Jain, I. H. El-Sayed and M. A. El-Sayed, *Nano Today*, 2007, **2**, 18.
44. H. Ding, K. T. Yong, I. Roy, H. E. Pudavar, W. C. Law, E. J. Bergey and P. N. Prasad, *J. Phys. Chem. C*, 2007, **111**, 12552.
45. H. Wang, B. Huff, D. A. Zweifel, W. He, P. S. Low, A. Wei and J. Z. Cheng, *Proc. Natl. Acad. Sci. U.S.A.*, 2005, **102**, 15752.
46. N. J. Durr, T. Larson, D. K. Smith, B. A. Korgel, K. Sokolov and A. Ben-Yakar, *Nano Lett.*, 2007, **7**, 941.
47. C. H. Chou, D. Chen and C. R. C. Wang, *J. Phys. Chem. B*, 2005, **109**, 11135.
48. T. B. Huff, L. Tong, Y. Zhao, M. N. Hansen, J. X. Cheng and A. Wei, *Nanomedicine*, 2007, **2**, 125.
49. L. Tong, Y. Zhao, T. B. Huff, M. N. Hansen, A. Wei and J. X. Cheng, *Adv. Mater. (Weinheim, Germany)*, 2007, **19**, 3136.
50. K. Kim, S. W. Huang, S. Ashkenazi, M. O'Donnell, A. Agarwal, N. A. Kotov, M. F. Denny and M. J. Kaplan, *Appl. Phys. Lett.*, 2007, **90**, 223901.
51. M. Eghtedari, A. A. Oraevsky, J. A. Copland, N. A. Kotov, A. Conjusteau and M. Motamedi, *Nano lett.*, 2007, **7**, 1914.
52. M. Mischchenko, L. Travis and A. Lacis, *Scattering, Absorption, and Emission of Light by Small Particles*, Cambridge University Press, Cambridge, 2002.
53. W. H. Yang, G. C. Schatz and R. R. v. Duyne, *J. Chem. Phys.*, 1995, **103**, 869.
54. B. T. Draine and P. J. Flatau, *J. Opt. Soc. Am. A*, 1994, **11**, 1491.
55. K. S. Lee and M. A. El-Sayed, *J. Phys. Chem. B*, 2005, **109**, 20331.
56. K. S. Lee and M. A. El-Sayed, *J. Phys. Chem. B*, 2006, **110**, 19220.
57. C. Ungureanu, R. G. Rayavarapu, S. Manohar and T. G. v. Leeuwen, *J. Appl. Phys.*, 2009, **105**, 102032.
58. P. K. Jain, K. S. Lee, I. H. El-Sayed and M. A. El-Sayed, *J. Phys. Chem. B*, 2006, **110**, 7238.
59. A. Brioude, X. C. Jiang and M. P. Pileni, *J. Phys. Chem. B*, 2005, **109**, 13138-13142.
60. G. Yin, S. Y. Wang, M. Xu and L. Y. Chen, *J. Korean Phys. Soc.*, 2006, **49**, 2108.

61. A. L. Gonzales and C. Noguez, *J. Comput. Theor. Nanosci.*, 2007, **4**, 231.
62. S. W. Prescott and P. Mulvaney, *J. Appl. Phys.*, 2006, **99**, 123504.
63. E. S. Kooij and B. Poelsema, *Phys. Chem. Chem. Phys.*, 2006, **8**, 3349.
64. J. Turkevich, P. C. Stevenson and J. Hiller, *Discuss. Faraday Soc.*, 1951, **11**, 55-75.
65. P. W. Atkins and R. S. Friedman, *Oxford University Press, Oxford*, 2004.
66. W. J. Hehre, L. Radon, P. R. Schleyer and J. A. Pople, *Wiley, New York*, 1985.
67. S. Franzen, J. C. W. Folmer, W. R. Glomm and R.O'Neal, *J. Phys. Chem. A*, 2002, **106**, 6533-6540.
68. H. G. Craighead and A. M. Glass, *Opt. Lett.*, 1981, **6**, 248-250.
69. J. Zhu, K. Zhu and L. Q. Huang, *Phys. Lett. A*, 2008, **372**, 3283-3288.
70. J. N. Demas and G. A. Crosby, *J. Phys. Chem.*, 1971, **75**, 991-1024.
71. B. G. Huth, G. I. Farmer and M. R. Kagan, *J. Appl. Phys.*, 1969, **40**, 5145.
72. T. Karstens and K. Kobs, *J. Phys. Chem.*, 1980, **84**, 1871-1872.
73. H. Du, R. A. Fuh, J. Li, A. Corkan and J. S. Lindsay, *Photochem. Photobiol.*, 1998, **68**, 141-142.
74. M. J. Snare, F. E. Treloar, K. P. Ghiggino and P. J. Thistlethwaite, *J. Photochem.*, 1982, **18**, 335-346.
75. K. L. Kelly, E. Coronado, L. L. Zhao and G. C. Schatz, *J. Phys. Chem. B*, 2003, **107**, 668-677.
76. P. B. Johnson and R. W. Christy, *Phys. Rev. B*, 1972, **6**, 4370.
77. E. D. Palik, *Handbook of Optical Constants of Solids*, Academic, New York, 1985.
78. J. Weaver, C. Krafka, D. Lynch and E. Koch, *Physics Data: Optical Properties of Metals Part 2: Noble Metals, Alumnum, Scandium, Yttrium, the Lanthanides and the Actinides*, Fach-Infomations Zentrum, Karlsruhe, 1981.
79. J. Zhuang, W. Dai, Q. Tian, Z. Li, L. Xie, J. Wang and P. Liu, *Lanfmuir*, 2010, **26**, 9686-9694.